

ESTEC

Deliverables D12: FinalReport (FR)

*SnowLab-NG*

20. Mar. 2023

**ESA CONTRACT NO. 4000130865/20/NL/FF/AN  
with  
WSL-BIRMENS DORF**

**SnowLab-NG**

**Deliverable D12:**

**D12: “final report (FR) of SnowLab-NG Project”**

**WSL-BIRMENS DORF REFERENCE NUMBER: WSL-Birmensdorf\_ESTEC/SnowLab-NG**

Created: 4. August 2022

**Authors:**

Mike Schwank, WSL-Birmensdorf  
Reza Naderpour, WSL-Birmensdorf  
Derek Houtz, WSL-Birmensdorf  
Henning Löwe, WSL-Davos (SLF)  
Roberto Colombo (UNIMIB)  
Roberto Garzonio (UNIMIB)  
Biagio di Mauro (UNIMIB)



 **GAMMA REMOTE SENSING**



## **TABLE OF CONTENTS**

1. Introduction .....	3
2. L-Band Radiometry of Seasonal Snow Cover .....	4
2.1. Results from first Campaign in Davos-Laret during Winter 2019/2020 .....	4
2.2. Results from second Campaign in Sodankylä during Winter 2020/2021 .....	8
3. Wideband scatterometry of seasonal snow cover.....	11
3.1. Results from first Campaign in Davos-Laret during Winter 2019/2020 .....	11
3.2. Results from second Campaign in Sodankylä during Winter 2020/2021 .....	19
4. Thermal Inertia Analysis .....	22
4.1. Data and Method .....	22
4.2. Snow Phases Detection.....	23
4.3. Relation between APs and Snow Density.....	25
4.4. APs and Passive L-band Snow Variables Comparison .....	25
4.5. Conclusions .....	26
5. References .....	28
Appendix A - D2: Preliminary Data Acquisition Report for Davos-Laret during Winter 2019/2020 campaign & D2a: Final DAR for Entire Season of Davos-Laret Campaign (update of D2)	
Appendix B - D8: “Preliminary Data Acquisition Report Sodankylä (2nd season)” & D8a: “Final Data Acquisition Report Sodankylä (2nd season)”	

## 1. INTRODUCTION

This document presents Deliverable D12 which is the “Final Report” (FR) of the SnowLab-NG project. As was agreed with the Technical Officer (TO), the FR includes D4 and D10 defined as the “Preliminary results documentations” associated with the first- and the second campaign performed in Davos-Laret and Sodankylä during the Winters 2019/2020 and 2020/2021, respectively. Mature results (published in [1] and [2]) achieved from passive- and active measurements from the first campaign are presented in Sections 2.1. and 3.1. , respectively. Preliminary results achieved from passive- and active measurements from the second campaign are presented in Sections 2.2. and 3.2. , respectively. Section 4. presents the summary results related to use of thermal inertia from InfraRed (IR) measurements for estimating snow parameters.

The first publication [1] originating from the SnowLab-NG project is entitled “Wideband Backscattering From Alpine Snow Cover: A Full-Season Study”. It was published in IEEE TGRS in 2022, and it describes WBSCAT measurements, including the WBSCAT calibration approach to achieve backscatter coefficients, and scientific results from the first campaign performed at the Davos-Laret Remote Sensing Field Laboratory [3] in the Swiss Alps during winter 2019/2020. More specifically, the results provide experimentally investigated relationships between copol backscattering at a wide range of frequencies (L- to Ka-bands) and snow-ground StateParameters (SPs) in different evolution phases during the full winter cycle.

The second paper [2] originating from the SnowLab-NG project is entitled “L-Band Radiometry of Alpine Seasonal Snow Cover: 4 Years at the “Davos-Laret Remote Sensing Field Laboratory” was accepted for publication in IEEE JSTARS in 2022. It reports on passive L-band measurements performed during four consecutive winter campaigns (2016 – 2020) at the Davos-Laret Remote Sensing Field Laboratory [3] to gain insight into the L-band microwave emission of ground covered with seasonal snow. The last of the four winter campaigns was performed within SnowLab-NG.

There exist numerous key differences between SnowLab-NG’s site for the first (Davos-Laret, Switzerland) and the second (Sodankylä, Finland) measurements campaign. These differences include climate, underlying ground’s freeze/thaw state, snow cover properties, and length of the snow cover period in each winter, exposure to radiation given vastly different lengths of days etc. Thus, performing the second campaign over the Arctic circle at FMI-ARC gives the chance to study which type of information about snow and its subnivean layer can be extracted from a similar set of measurements and whether and to what extent the findings in an alpine site are applicable to the high latitude arctic region and vice versa.

## 2. L-BAND RADIOMETRY OF SEASONAL SNOW COVER

### 2.1. Results from first Campaign in Davos-Laret during Winter 2019/2020

The here reported results are derived from the L-band brightness temperature measurements performed at the Davos-Laret Remote Sensing Field Laboratory [3], henceforth called “Davos-Laret RS site” or “site”. Situated at the Laret valley ( $46^{\circ}50'43''$  N,  $9^{\circ}52'19''$  E) at an altitude of 1420 m a.s.l., this site was established in autumn 2016 for long-term close-range active- and passive microwave remote sensing of alpine snow. The site extends over  $\sim 50 \text{ m} \times 50 \text{ m}$ ; it is relatively flat with small undulations of less than a meter height surrounding all but the north-eastern side. **Figure 1** shows an aerial image of the site highlighting its position with respect to the neighboring Lake-Schwarz, residential area, and the forested regions. The location of the microwave RadioMeter (RM) tower and multiple sets of FootPrint (FP) areas over the site during the SnowLab-NG’s first Winter Campaign 2019/2020 are depicted in **Figure 1**. The more detailed schematics of the site during the SnowLab-NG’s first campaign in winter 2019/2020 is illustrated with **Figure 2**.



**Figure 1:**

Overview photo of the Davos-Laret Remote Sensing (RS) site with indicated RadioMeter (RM) and WBSCAT tower and FootPrints (FP) observed during the Winter Campaign 2019/2020. The detailed layout of the campaign is shown in Figure 2.

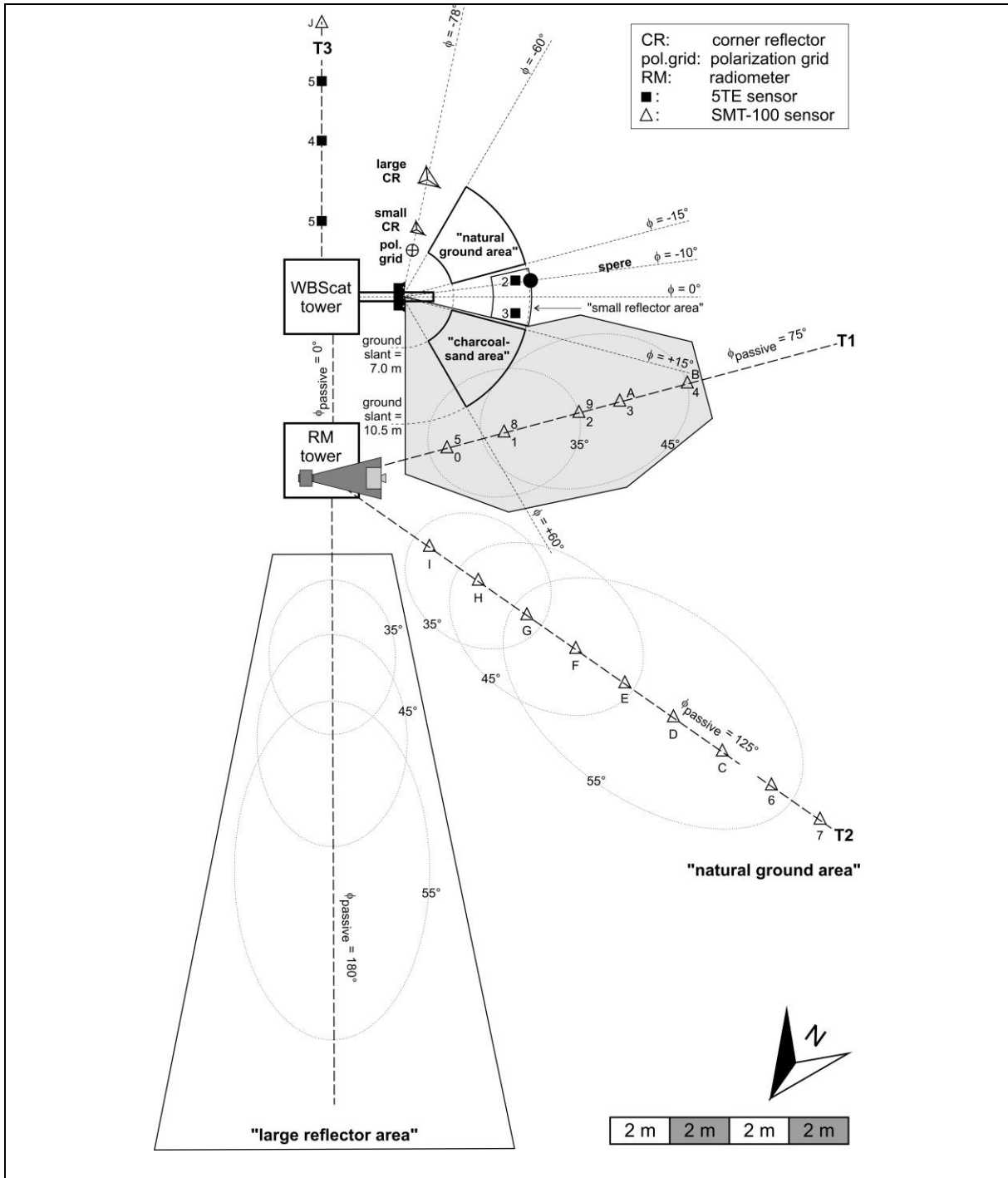


**Figure 2:** Schematics of the Davos-Laret field site implemented during the winter 2019/2020 campaign

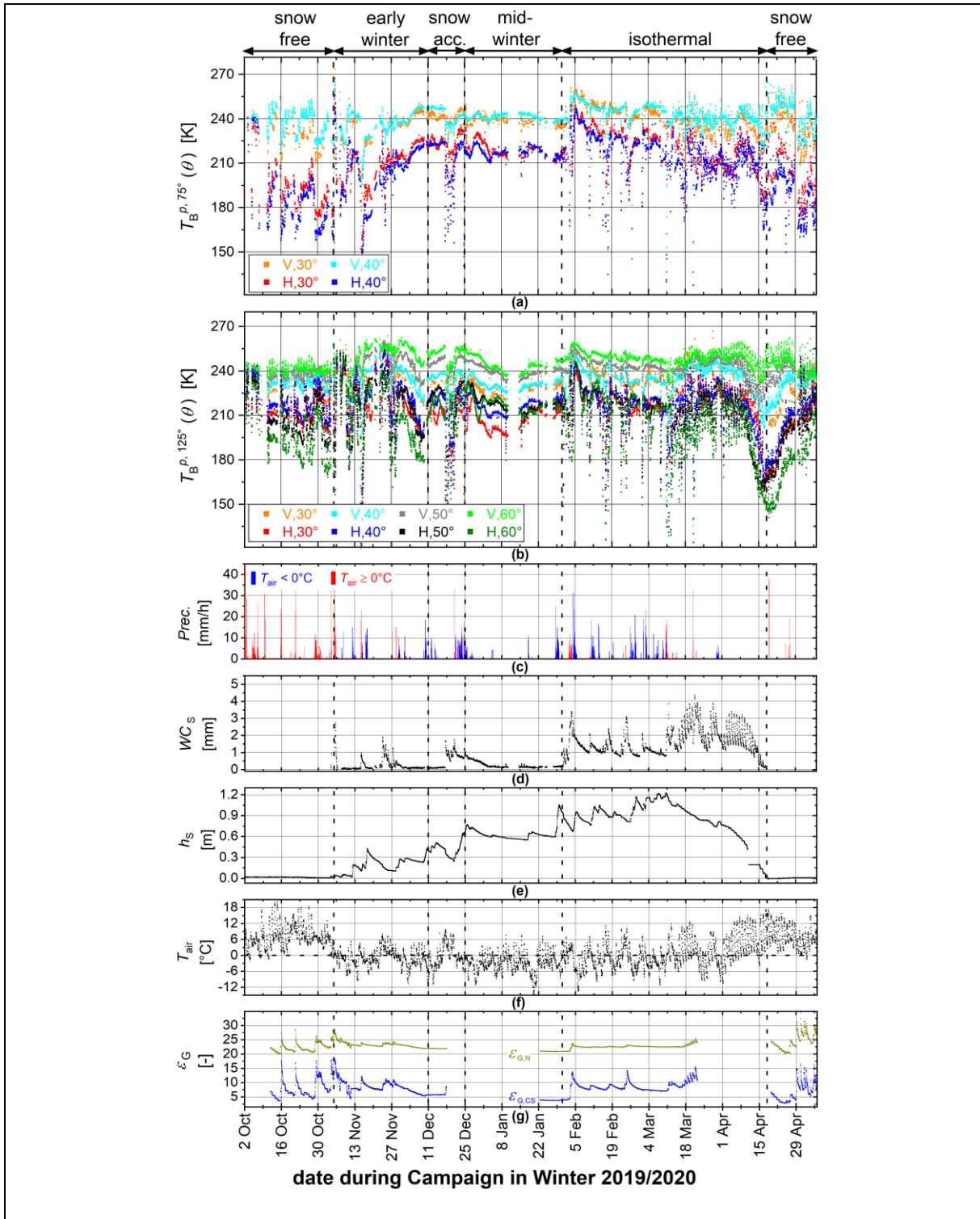


**Figure 3:** Measurements conducted during Winter campaign 2019/2020. (a) Brightness temperatures  $T_B^{p,75^\circ}(\theta)$  over “charcoal-sand areas” at  $\phi = 75^\circ$ ; (b) Brightness temperatures  $T_B^{p,125^\circ}(\theta)$  over “natural areas” at  $\phi = 125^\circ$ ; (c) precipitation (Prec.) differentiated according to  $T_{air} \geq 0^\circ\text{C}$  (red) and  $T_{air} < 0^\circ\text{C}$  (blue); (d) Snow liquid Water-Column  $WC_S$  retrieved from brightness temperature  $T_B^{p,75^\circ}(\theta)$  of the “Reflector area”; (e) Snow height  $h_S$ ; (f) air temperature  $T_{air}$ ; (g) mean Ground permittivities  $\epsilon_G = \epsilon_{G,N}$  (yellow) and  $\epsilon_G = \epsilon_{G,CS}$  (blue) measured along Transects T2 and T1, respectively, shown in **Figure 2**.

**Figure 3** provides an overview of the measurements conducted during winter 2019/2020 campaign. **Figure 3(a,b)** show the time-series of  $T_B^{p,\phi}(\theta)$  measured over “charcoal-sand area” at azimuth angle  $\phi = 75^\circ$  and over the “natural area” at  $\phi = 125^\circ$ , respectively. In **Figure 3 (a)** only the  $T_B^{p,75^\circ}(\theta)$  at  $\theta = \{30^\circ, 40^\circ\}$  are shown because as illustrated in **Figure 2**, the “charcoal-sand area” was designed to fully cover L-band radiometer’s -9 dB FPs associated with  $30^\circ \leq \theta \leq 45^\circ$ .

It is evident from **Figure 3**, especially during “snow-free” and “mid-winter” phases, polarization differences in brightness temperatures are more pronounced for  $T_B^{p,75^\circ}(\theta)$  over the “charcoal-sand area” than for  $T_B^{p,125^\circ}(\theta)$  measured over the “natural area”. This is best visible during the “snow-free” phase at the beginning of the campaign where for a given nadir angle  $\theta$  differences  $T_B^{V,75^\circ}(\theta) - T_B^{H,75^\circ}(\theta)$  over the “charcoal-sand area” is  $\sim 40$  K (**Figure 3 (a)**) while corresponding differences  $T_B^{V,125^\circ}(\theta) - T_B^{H,125^\circ}(\theta)$  over the “natural area” is  $\sim 30$  K (**Figure 3 (b)**). This is a direct effect of impedance matching and lower surface roughness provided by the “charcoal-sand area” compared to the “natural area”.

As seen in **Figure 3(f)**, air temperature was virtually constantly above  $T_{\text{air}} = 0^\circ\text{C}$  which prevented the ground from freezing. Correspondingly, mean Ground permittivities of “natural area” (measured with sensors along T2 and T3 in **Figure 2**) are  $\epsilon_{G,N}$  (**Figure 3(g)**) and therefore prove the unfrozen state of ground. In contrast, mean permittivities  $\epsilon_{G,CS}$  within the “Charcoal-Sand area” (CS) are considerably lower, sometimes  $\epsilon_{G,CS} < 5$ . However, this does not mean that the “charcoal-sand area” froze at any time; instead, the generally low  $\epsilon_{G,CS}$  are due to the low water-holding capacity of the surface layer of this area.

Both permittivity records,  $\epsilon_{G,N}$  and  $\epsilon_{G,CS}$ , fluctuate in response to precipitations such as on 16, 21, and 29 October 2019 during the “snow-free” period before snow onset. During the “early winter” phase, in-situ  $\epsilon_{G,N}$  and  $\epsilon_{G,CS}$  respond to liquid water brought by major precipitations at  $T_{\text{air}} \geq 0^\circ\text{C}$  (for example on 15 November 2019) and increased  $WC_S$  (for example on 23 to 25 November 2019). **Figure 3(g)** shows that from approximately 30 November 2019 ground permittivities of the “natural area” and the “charcoal-sand area” ceased their fluctuations and by the middle of the “snow accumulation” phase they had settled to  $\epsilon_{G,N} \approx 21.8$  and  $\epsilon_{G,CS} \approx 5.8$ , respectively. Despite the gap in the ground permittivities, the next available records on 23 January 2020 in “mid-winter” phase confirm that in presence of thermally insulating snow, subnivean permittivity was stable. The time-series of  $WC_S$  in **Figure 3(d)** shows that the “mid-winter” phase is immediately followed by “isothermal” phase with  $WC_S$  rapidly increasing to high values making the snowpack opaque even for L-band observations.

According to **Figure 3(e)**, the “isothermal” phase ended with a quick melt enforced with consistent  $T_{\text{air}} > 0^\circ\text{C}$  such that between 10 to 18 April 2020, Snow height dropped from  $h_S \approx 0.45$  m to zero. The signature of this quickly disappearing snow cover is visible in  $T_B^{p,75^\circ}(\theta)$  over the “charcoal-sand area” (**Figure 3(a)**) and in  $T_B^{p,125^\circ}(\theta)$  over “natural area” (**Figure 3(b)**).

For example,  $T_B^{H,75^\circ}(40^\circ)$  and  $T_B^{H,125^\circ}(60^\circ)$  drop by  $\sim 50$  K and  $\sim 64$  K, respectively, in the aforementioned period.

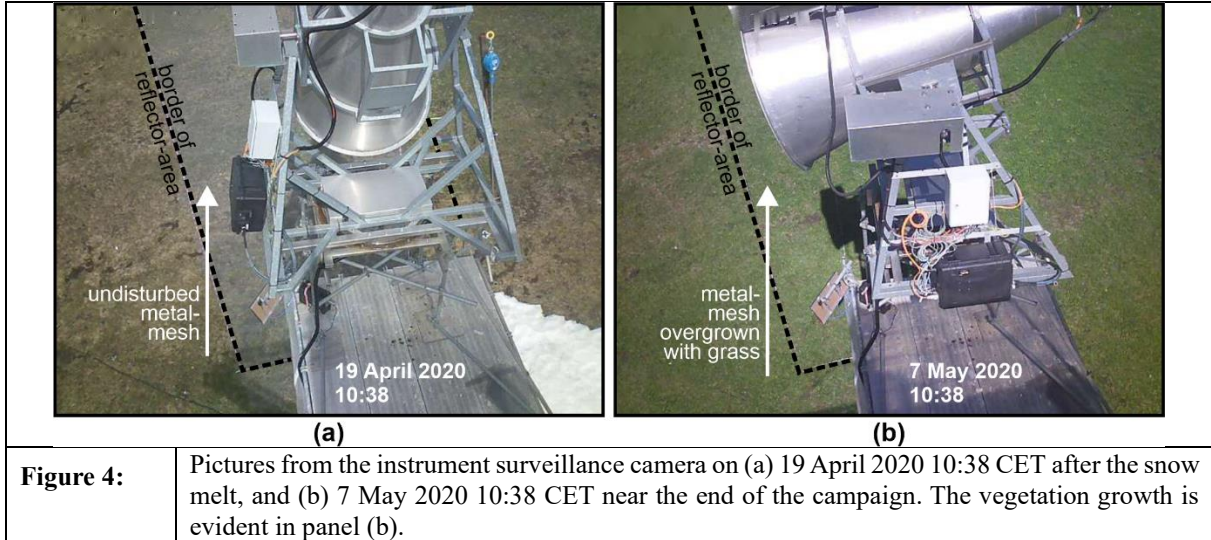


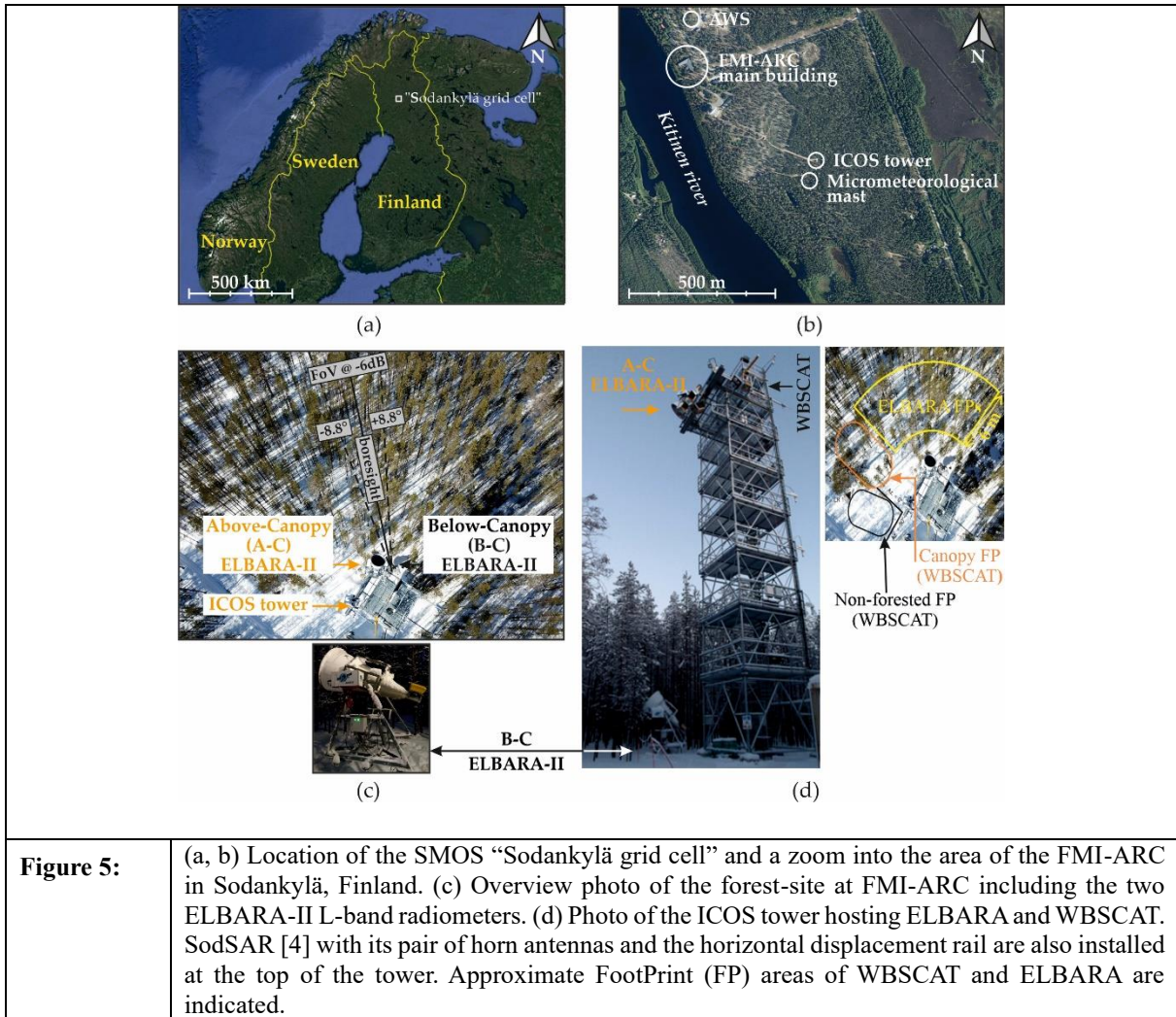
**Figure 4:** Pictures from the instrument surveillance camera on (a) 19 April 2020 10:38 CET after the snow melt, and (b) 7 May 2020 10:38 CET near the end of the campaign. The vegetation growth is evident in panel (b).

It is noteworthy that after complete snow melt,  $T_B^{p,125^\circ}(\theta)$  (**Figure 3(b)**) especially at  $p = H$ , starts increasing. Given the increased  $T_{air} \gg 0^\circ\text{C}$  and snow-free conditions, the vegetation started growing on natural soil. Photographic proof of this vegetation growth is provided in **Figure 4**.

Both photos were automatically taken at 10:38 CET after the end of the “isothermal” phase (19 April 2020) and at the end of the campaign (7 May 2020). Since the “snow-free” phase after snow clearance lasted for  $\sim 20$  days, the effect of growing vegetation on  $T_B^{p,125^\circ}(\theta)$  is noticeable. **Figure 4(b)** shows that by the end of the campaign even the “reflector area” at  $\phi = 180^\circ$  (see **Figure 2(b)**) is covered with green grass which grew through the metal-mesh grid. Vegetation did not grow over the artificially created “charcoal-sand area”; therefore,  $T_B^{p,75^\circ}(\theta)$  does not exhibit an increasing trend towards the end of the campaign.

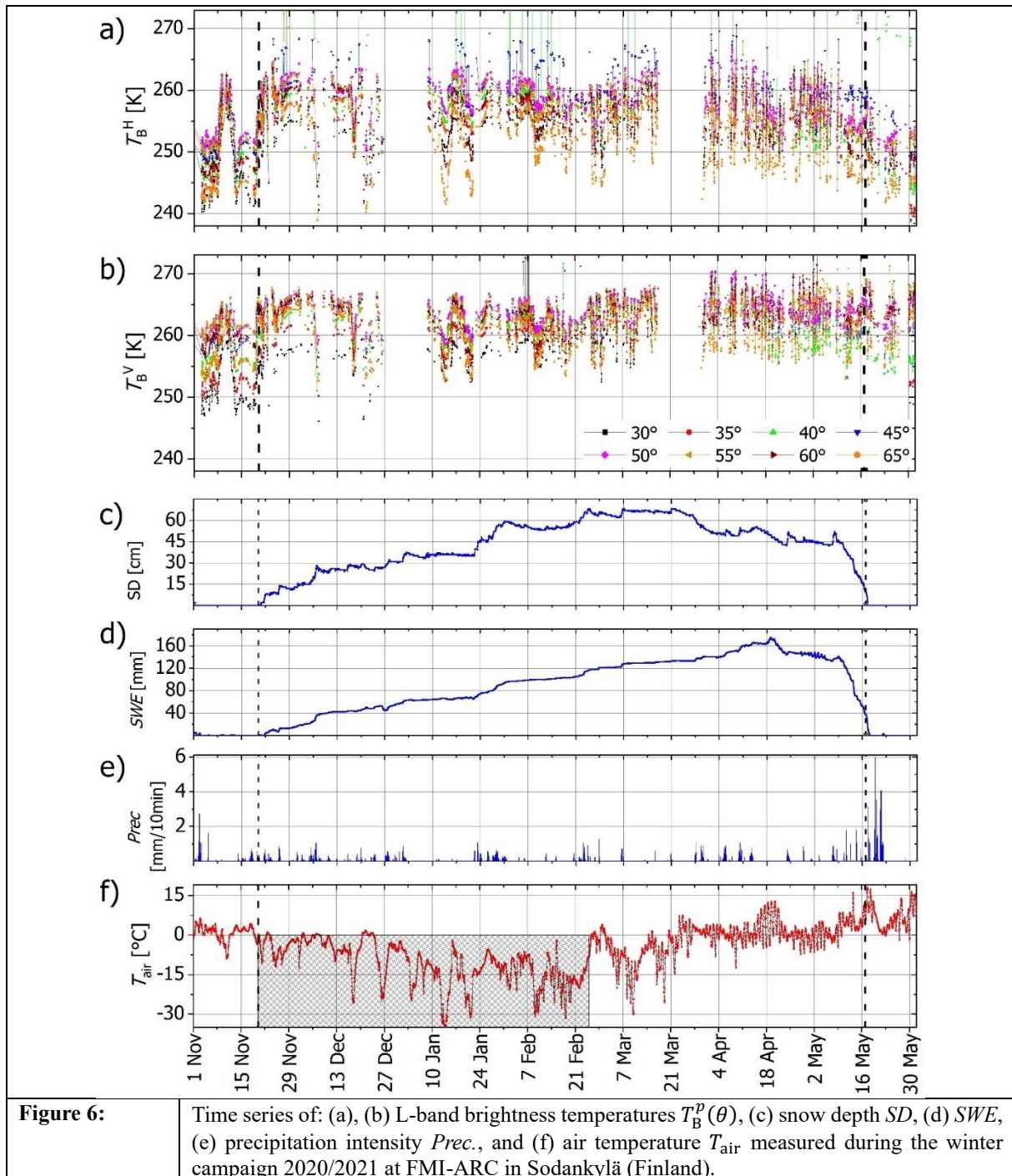
## 2.2. Results from second Campaign in Sodankylä during Winter 2020/2021

As shown in **Figure 5**, two ELBARA radiometers were installed at the bottom and at the 23 m platform of the ICOS tower at FMI-ARC in Sodankylä. The downward looking Above-Canopy (AC) ELBARA radiometer measures L-band  $T_B^p(\theta)$  at a nadir angle range of  $\theta = \{30^\circ, 35^\circ, \dots, 175^\circ, 180^\circ\}$  thus measuring the L-band thermal emission of the ground and canopy, the horizon, and the sky with time resolution of one hour. Here we present preliminary results derived from  $T_B^p(\theta)$  measured by the AC ELBARA-II shown in **Figure 6** for  $\theta = \{30^\circ, 35^\circ, 40^\circ, 45^\circ, 50^\circ, 55^\circ, 60^\circ, 65^\circ\}$ .



Panels (a) –(f) in **Figure 6** show the time series of L-band  $T_B^p(\theta)$ , snow depth  $SD$ ,  $SWE$ , precipitation intensity  $Prec.$ , and air temperature  $T_{air}$  2 m above the surface, respectively. The length of winter time with  $T_{air} < 0^\circ\text{C}$  is noticeably different between Sodankylä and Davos-Laret (compare **Figure 3**). As shown in **Figure 6** (f), with a few exceptions  $T_{air}$  stays below  $0^\circ\text{C}$  for about four months between mid-November 2020 to late-March 2021 indicating dry snow conditions.

In **Figure 6** the onset of snow cover on 20 November 2020 and its complete melt on 17 May 2021 are marked with vertical dashed lines in all panels. It is evident in **Figure 6** (a) that the onset of snow cover has a distinct increasing effect on the  $T_B^H(\theta)$  which itself is dependent on the observation nadir angle  $\theta$ . Similarly, the complete melt of snow cover has an effect on  $T_B^H(\theta)$  such that  $T_B^H(\theta)$  falls by as much as 10 K as a response to the vanished snow. L-band  $T_B^V(\theta)$  at vertical polarization  $p = V$  (**Figure 6** (b)) also respond to the snow cover changes but less distinctly compared to  $T_B^H(\theta)$ . The closer  $\theta$  to the Brewster angle, the less distinct the response of  $T_B^V(\theta)$  to snow cover variations.



### 3. WIDEBAND SCATTEROMETRY OF SEASONAL SNOW COVER

#### 3.1. Results from first Campaign in Davos-Laret during Winter 2019/2020

We investigated relationships between snow–ground SPs and backscattering coefficient  $\sigma_{pp}^0(f)$ . Due to the antennas’ wide field of view, differences between backscattering coefficients  $\sigma_{HH}^0(f)$  and  $\sigma_{VV}^0(f)$  are depressed; therefore, we present only  $\sigma_{VV}^0(f)$ . Our analysis of the measured backscatter signals is based on considering single-scattering mechanisms originating from three elements ( $\equiv$  regimes) of the snow–ground compartment:

- 1) scattering from the snow–air interface
- 2) volume scattering from the snowpack
- 3) scattering from the snow–ground interface.

Therefore, the overarching question of our investigation is given as follows:

*What is the relative strength of each of the mentioned three scattering elements at a given frequency for different snow states?*

Snow wetness is also of critical importance as a primary influencer of  $\sigma_{pp}^0(f)$  due to increased propagation losses with increasing snow liquid water content. The answer to mentioned overarching question is presented in **Table 1** with qualitative indicators (negligible, medium, and high) based on the presented experimental observations. The three rows in **Table 1** list the aforementioned scattering elements (air–snow interface, snow volume, and snow–ground interface). The six columns [cases (1)–(6)] list, in pairs, the three WBSCAT frequency ranges (1–4, 4–12, and 12–40 GHz) each under dry and wet snow conditions as estimated from passive L-band measurements over the “large reflector area” (see **Figure 2**). The table must be read in columns. The relative strength of a given scattering element is indicated in each table cell. In the following, we present examples of  $\sigma_{VV}^0(f)$  related to cases in **Table 1** and provide physical reasoning behind the applied assignments.

	L- and S-bands		C- and X-bands		Ku- to Ka-bands	
	low frequency (1 – 4 GHz)		intermediate frequency (4 – 12 GHz)		high frequency (12 – 40 GHz)	
	dry	wet	dry	wet	dry	wet
	(1)	(2)	(3)	(4)	(5)	(6)
air-snow interface	negligible	medium	negligible	medium	negligible	high
snow volume	medium	high	medium	high	high	medium
snow-ground interface	high	negligible	high	negligible	medium	negligible

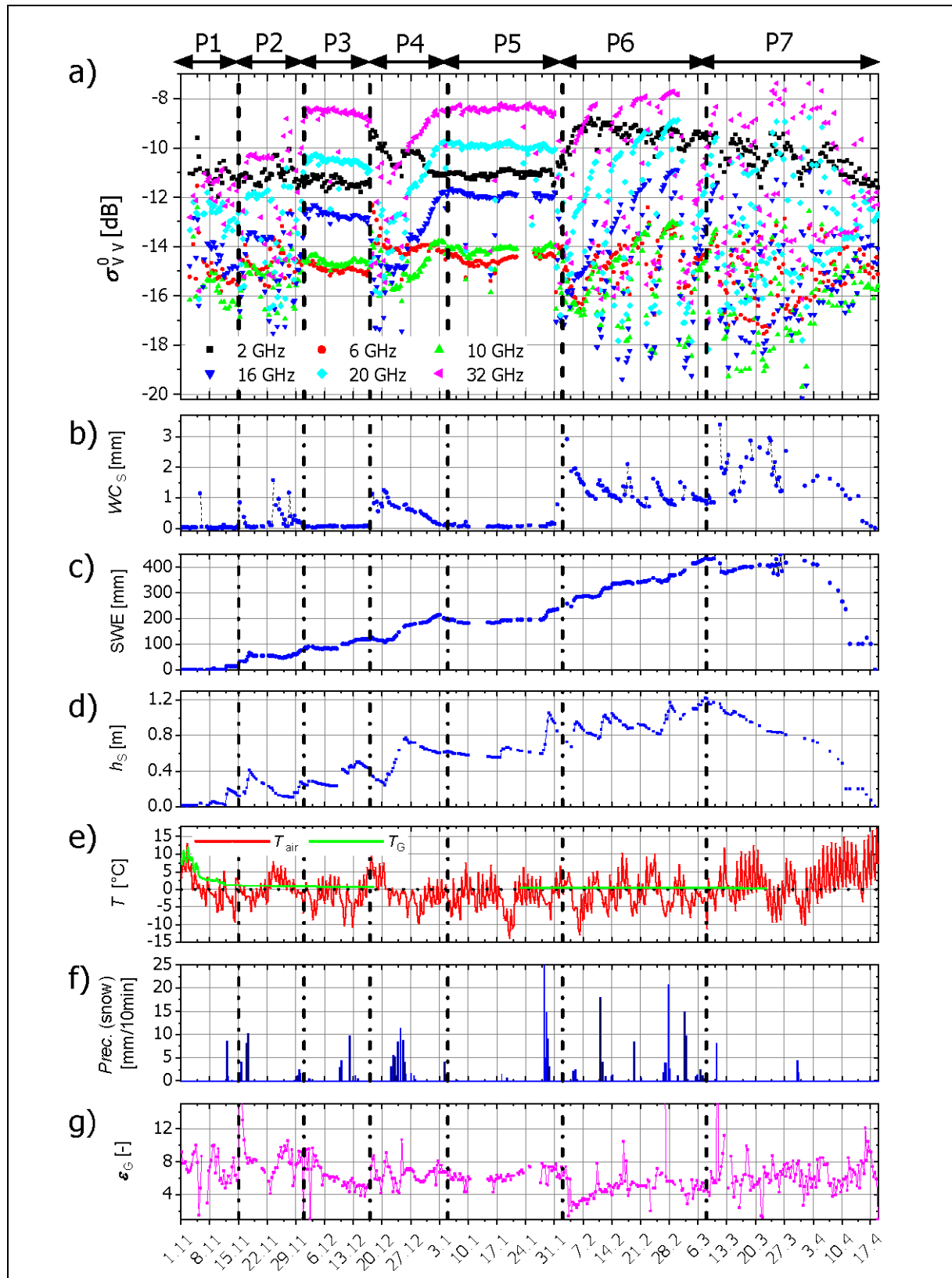


**Figure 7:** Time series of (a) backscattering coefficient  $\sigma_{VV}^0(f)$  and (b) snow liquid water column  $WC_S$  retrieved from L-band radiometry. (c)–(g) In situ measured SWE, snow height  $h_S$ , ground and air temperature, snow precipitation, and ground permittivity, respectively.

**Figure 7** shows the time series of:

- 1) calibrated backscattering coefficients  $\sigma_{VV}^0(f)$  measured at antenna nadir angle  $35^\circ$  and at six frequencies representing WBSCAT's frequency range from L- to Ka-bands;
- 2) snow liquid water column  $WC_S$  retrieved from L-band radiometry;
- 3)–6) SWE, snow height  $h_S$ , air- and Ground temperatures  $T_{air}$  and  $T_G$ , and snow precipitation Prec. measured by the on-site AWS; and
- 7) Permittivity  $\epsilon_G$  of the sand layer in the “charcoal–sand area.” Snow precipitation Prec. is considered as the precipitation taken place at  $T_{air} \leq 0^\circ\text{C}$ .

To better understand the temporal variations of  $\sigma_{VV}^0(f)$ , we first assess the snow cover conditions during Winter 2019/2020 according to the three main State-Parameters (SPs):  $h_S$ ,  $WC_S$ , and SWE. **Figure 7(d)** shows that the onset and complete melt of snow cover over the site happened on November 15, 2019, and April 17, 2020, respectively. The onset of snow cover was not a sudden clear-cut event with heavy snowfall, rather roughly one week of fluctuating increases of  $h_S$ . It is important to note the strong relative  $h_S$  fluctuations and the effect of increased snow volume scattering under dry snow conditions.

A closer look at the time series of  $WC_S$  (and  $h_S$ ) indicates that the entire winter season can be broken down into seven periods (P1—P7) marked at the top of **Figure 7**. This classification is beneficial to describe and understand the temporal variations of  $\sigma_{VV}^0(f)$  and their relationship with SPs of the ground–snow compartment.

**1) Period 1 [Snow-Free Period (November 1, 2019 – November 15, 2019)]:**

As mentioned in **Section 2**, permittivity and temperature measurements indicate unfrozen moist ground during this period.

**2) Period 2 [First Wet Snow Period (November 15, 2019 – December 1, 2019)]:**

A thin wet snowpack appears over the unfrozen ground. Snowpack height undergoes significant fluctuations reaching a maximum of  $h_S \approx 40$  cm and dropping down to a minimum of  $h_S \approx 15$  cm.

**3) Period 3 [First Dry Snow Period (December 1, 2019 – December 17, 2019)]:**

Snow accumulation continues,  $T_{air}$  decreases, and snow is dry according to  $WC_S$  derived from L-band radiometry performed over the “large reflector area.”

**4) Period 4 [Second Wet Snow Period (December 17, 2019 – December 5, 2020)]:**

Snow accumulation continues, accompanied by  $T_{air} > 0^\circ$ . This results in increased snow wetness demonstrated by  $WC_S > 0$  mm.

**5) Period 5 [Second Dry Snow Period (January 5, 2020 – February 2, 2020)]:**

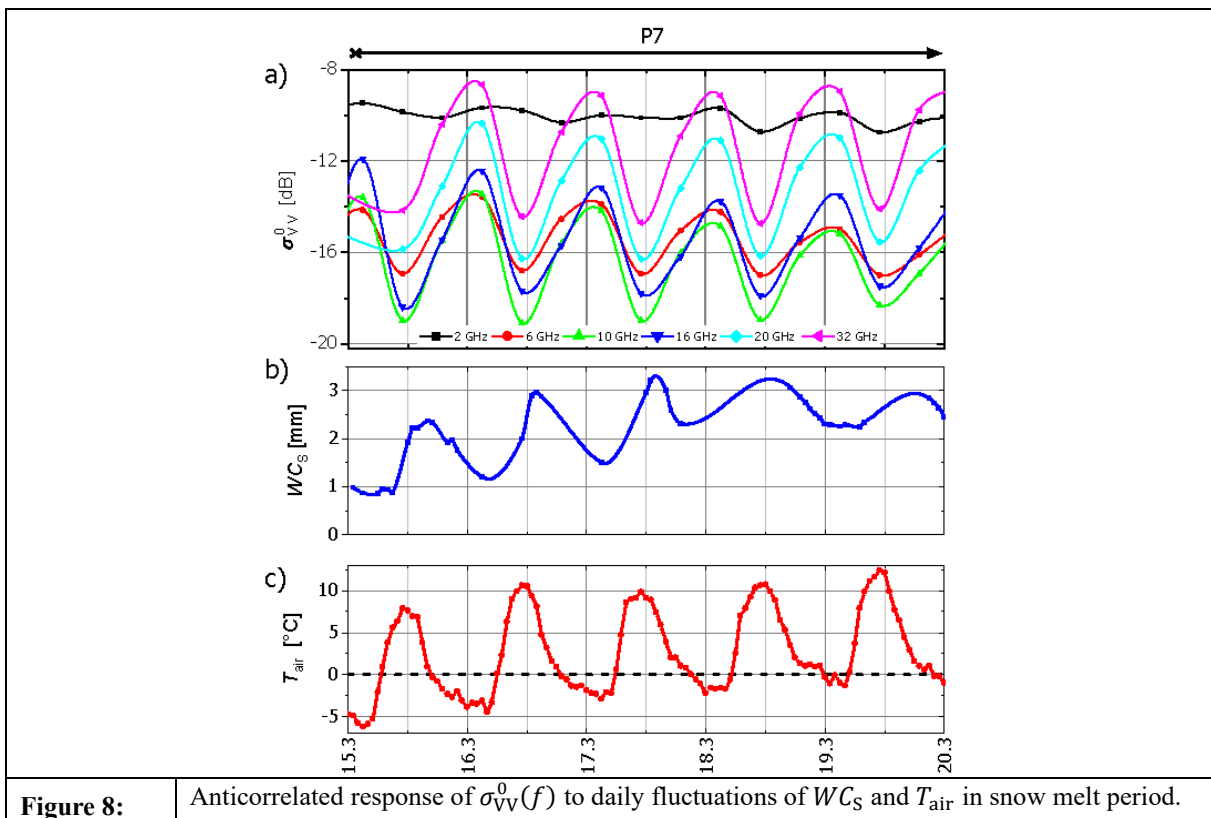
Snowpack enters a second dry period with  $h_S \approx 70$  cm. Near the end of period 5, a strong dry snow precipitation event increases snowpack height to  $h_S \approx 100$  cm.

**6) Period 6 [Early Spring Period (February 2, 2020 – March 8, 2020)]:**

$T_{air}$  follows a nearly weekly fluctuation pattern where temperature reaches a maximum of  $\sim 10$  °C and drops to a minimum of  $\sim -14$  °C. As a result, snow liquid water-column fluctuates while never dropping to  $WC_S = 0$  mm. It is noteworthy that snow accumulation continues resulting in steadily increasing SWE and an increasing trend in  $h_S$ , including significant fluctuations.

**7) Period 7 [Snow Melt and Run-Off (March 8, 2020 – April 19, 2020)]:**

Air temperature  $T_{air}$  increases significantly and mostly stays above melting point even with daily fluctuations of more than 10 °C. The snowpack starts to melt evidenced by continuously high  $WC_S$  and steadily decreasing  $h_S$  throughout period 7. Decrease in SWE is delayed by approximately one month compared to the decrease in  $h_S$  as the result of snow compaction.



Of all the snow, subnivean ground layer, and meteorological SPs in **Figure 7**, the effects of snow liquid water-column  $WC_S$  and, to a lesser extent, onset of snow cover represented by  $h_S$  on  $\sigma_{VV}^0(f)$  are clear. These effects are explained with some distinguishable examples. During the dry snow periods P3 and P5,  $\sigma_{VV}^0(f)$  takes on an almost steady trend; however, with fluctuating  $WC_S$  during early spring (P6) and snow melt (P7) periods, backscattering at all frequencies fluctuates in response to  $WC_S$ . **Figure 8** (a)–(c) shows a zoomed-in view of  $\sigma_{VV}^0(f)$ ,  $WC_S$ , and  $T_{air}$ , respectively, during snow melt period (P7). It is evident that all three parameters

show a diurnal fluctuation. Fluctuations of  $WC_S$  are delayed by 2–5 h with respect to  $T_{\text{air}}$  due to ice latent heat and thermal insulation of snow [5]. It is noteworthy that the aforementioned delay has an inverse relation with the observation frequency. Nevertheless,  $WC_S$  from L-band radiometry provides a comprehensive insight to the temporal evolution of  $\sigma_{\text{VV}}^0(f)$ , influenced by varying snow liquid water content, without the  $WC_S$  retrievals reaching saturation.

Increasing liquid water means higher propagation losses at all frequencies leading to decreasing  $\sigma_{\text{VV}}^0(f)$ . The frequency dependence of this effect is highlighted by pointing out the average fluctuation amplitude of  $\sigma_{\text{VV}}^0(f)$ , which is about 5.5 dB at  $f = 32$  GHz and only  $\sim 0.8$  dB at  $f = 2$  GHz. It is noteworthy that, for dry snow, the penetration depth of microwaves is  $>100$  m at 2 GHz [6] and decreases to about 1 m at 40 GHz [7]. This partially explains the qualitative assessment of the relative influence intensities (negligible, medium, and high) assigned to the different scattering elements (air–snow interface, snow volume, and snow–ground interface) for wet snow scenarios outlined in **Table 1** (cases 2, 4, and 6). At high frequencies, with high propagation losses (low penetration depths) in the uppermost few millimetres to centimetres of the snowpack, the air–snow surface is the major scattering element, while, during the snow melt period (P7), the ground is almost entirely invisible to high-frequency microwaves (Ku–Ka bands). This finding is supported by previous works, such as [8] and [7]. Accordingly, the snow–ground interface has a negligible scattering contribution leaving a medium (to negligible) contribution from the snow volume, which itself depends on the actual liquid water content and height of the snowpack. Similarly, for “low” (1–4 GHz) and “intermediate” (4–12 GHz) frequency observations, during wet snow conditions, the snow–ground interface becomes a negligible scattering element (cases 2 and 4 in **Table 1**).

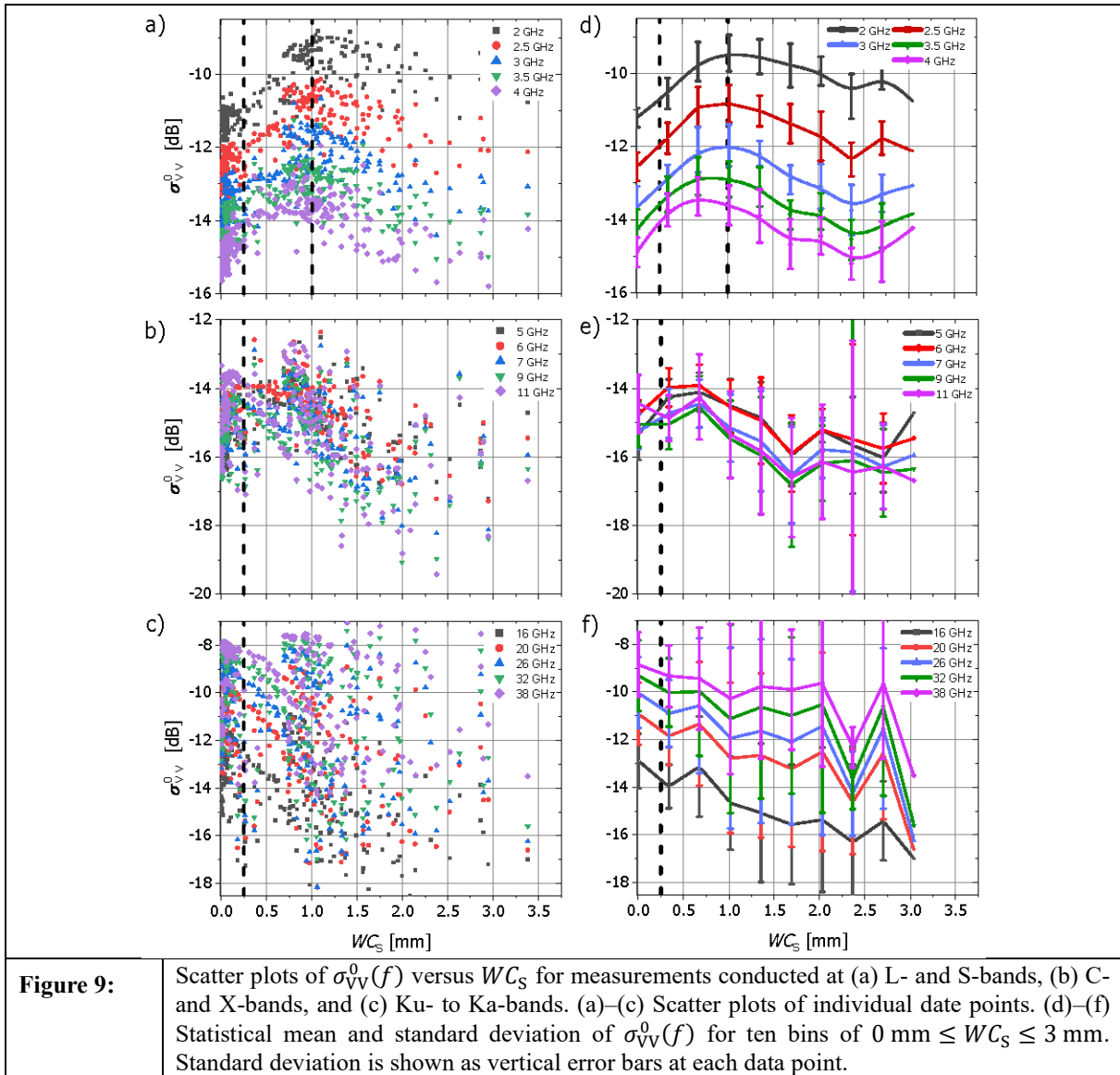


**Figure 7** clearly shows an effect of snow liquid water column  $WC_S$  on backscatter  $\sigma_{VV}^0(f)$ , and **Figure 8** highlights this relationship and demonstrates the anticorrelation between  $WC_S$  and  $\sigma_{VV}^0(f)$ . To investigate this relationship, scatter plot of  $\sigma_{VV}^0(f)$  versus  $WC_S$  are shown in **Figure 9** (a)–(c), where the panel refer to the “low,” “intermediate,” and “high” Frequency Bands (FBs) defined in **Table 1**. **Figure 9** (d)–(f) are prepared based on the data in **Figure 9** (a)–(c) to highlight the key features of the data shown in the scatter plots. To this aim, the average  $\sigma_{VV}^0(f)$  for given ranges of  $WC_S$  at each frequency is computed and plotted. The error bars indicate the standard deviation of each statistical sample. Here, we emphasize that this is not a polynomial fitting exercise, rather a more compact statistical representation of the same data in **Figure 9** (a)–(c).

The following key observations are made based on the plots of  $\sigma_{VV}^0(f)$  versus  $\sigma_{VV}^0(f)$   $WC_S$  in **Figure 9**:

- 1) According to **Figure 9** (a)–(c), for nearly dry snow ( $0 \text{ mm} \leq WC_S \leq 0.25 \text{ mm}$ ), backscattering coefficient  $\sigma_{VV}^0(f)$  at no frequency shows any relationship with snow liquid water column. This is expected from respective low penetration loss of microwaves in dry snow. This also implies the higher relevance of the snow–ground interface and snow volume as scattering elements. It also explains why the air–snow interface’s relative scattering contribution at all bands is set to “negligible” for dry snow in **Table 1** (cases (1), (3), and (5)).
- 2) For wet snow and at “low” and “intermediate” frequencies, there exists a clear anticorrelation between  $\sigma_{VV}^0(f)$  and  $WC_S$ . Panels (d) and (e) in **Figure 9** demonstrate this inverse relationship, which results in  $\sim 4 \text{ dB}$  drop in  $WC_S$  in the range  $1 \text{ mm} \leq WC_S \leq 2 \text{ mm}$  for “low” frequencies (panel (d)) and  $\sim 2.2 \text{ dB}$  drop in  $WC_S$  in the range  $0.6 \text{ mm} \leq WC_S \leq 1.7 \text{ mm}$  for “intermediate” frequencies. Panels (d) and (e) in **Figure 9** show that the definition of snow wetness states depends on the frequency of observation. Accordingly, for “low” and “intermediate” frequencies, “wet” snow refers to  $WC_S \geq 1 \text{ mm}$  and  $WC_S \geq 0.6 \text{ mm}$ , respectively.
- 3) Scatter plots in **Figure 9** (a)–(c) show that for high snow wetness  $WC_S$  (2 mm, 1.7 mm, 1 mm) for “low”, “intermediate”, and “high” frequencies, respectively, the sensitivity of backscattering coefficient to snow liquid water column decreases, and thus, their anticorrelation diminishes. Only less than 5% of the total data lie at  $WC_S \geq 2 \text{ mm}$ ; therefore, extra caution must be used in drawing conclusions on the relationship between  $\sigma_{VV}^0(f)$  and  $WC_S$  in this range (especially in **Figure 9** (d) and (e)).
- 4) At “high” frequencies (see **Figure 9** (c) and (f)), except for a generally decreasing  $\sigma_{VV}^0(f)$  with increasing  $WC_S$ , no firm conclusion can be drawn on the relationship between  $\sigma_{VV}^0(f)$  and  $WC_S$ . This is also clear from the generally larger error bars in **Figure 9** (f) compared to the ones in **Figure 9** (d) and (e) for every given  $WC_S$ . As reflected in **Table 1** (case 6) for wet snow, the main scattering element is the air–snow interface where snow surface roughness plays a key role.
- 5) According to **Figure 9** (a),  $\sigma_{VV}^0(f)$  initially increases with increasing snow liquid water column  $0.25 \text{ mm} \leq WC_S \leq 1.0 \text{ mm}$  before taking on the inverse relationship described in Point 2 above. At this range of  $WC_S$ , the snowpack is still semitransparent at low frequencies, meaning that backscattering from snow–ground interface is noticeable. Simultaneously, liquid water enhances the snow volume scattering. This is because structural heterogeneities inside snow volume become more effective scatterers when their permittivity increases with increasing snow liquid water content. These two mechanisms (backscatter from the ground and snow volume scattering) have a reinforcing effect resulting in higher  $\sigma_{VV}^0(f)$ . However, the losses for wet snow ( $WC_S \geq 2 \text{ mm}$ )

create an opaque snowpack and, thus, negligible backscattering from the snow–ground interface (case (2) in **Table 1**).

It is reiterated that  $WC_S$  on the horizontal axis of plots in **Figure 9** is estimated from L-band radiometry, which has a larger penetration depth in moist snow compared to measurements at higher frequencies. The lack of a clear correlation between  $WC_S$  retrieved from L-band radiometry and  $\sigma_{VV}^0(f)$  measured at the highest FBs (see **Figure 9** (c)) is expected. Accordingly,  $WC_S$  is much more representative of the snowpack’s liquid water-column, while  $\sigma_{VV}^0(f)$  at 16–38 GHz is predominantly sensing liquid water in the snowpack’s near surface layer.

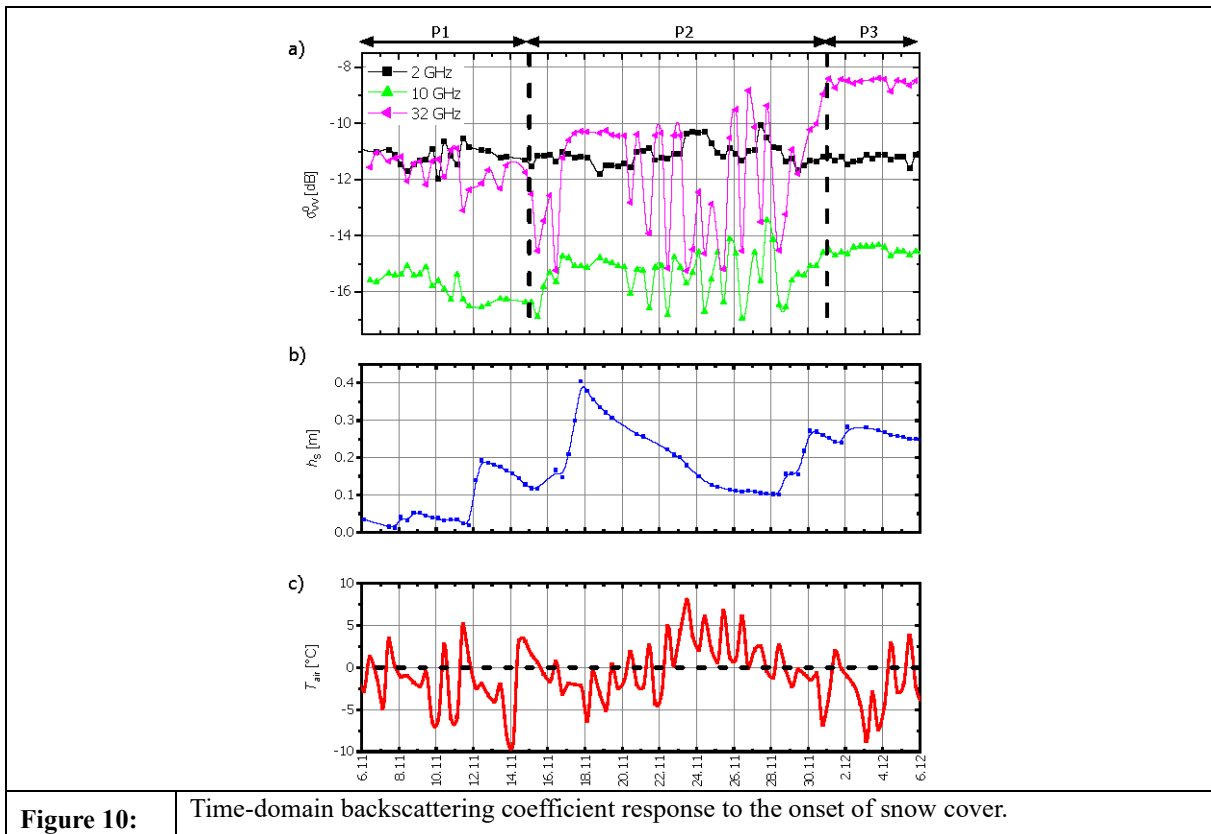


**Figure 10:** Time-domain backscattering coefficient response to the onset of snow cover.

As mentioned earlier in this section, in addition to  $WC_S$ , the backscattering coefficient shows a distinguishable response to the onset of snow cover represented by  $h_s$ . **Figure 10** (a)–(c) shows the time series of  $\sigma_{VV}^0(f)$ ,  $h_s$ , and  $T_{air}$  for the first month of snow cover over the site. P1, P2, and P3 refer to the snowfree period, first period of thin moist snow, and first period of dry snow, respectively. **Figure 10** shows that, with the snowpack reaching  $h_s = 0.4$  m  $\sigma_{VV}^0(f = 32$  GHz) increases, on average, by  $\sim 1.9$  dB during the period November 6–20, 2019. With the start of P3 and due to effective dry snow volume scattering,  $\sigma_{VV}^0(f = 32$  GHz) reaches average values of  $\sim 8.5$  dB creating a relative difference of  $\sim 3.6$  dB compared to the snow-free P1. This suggests that higher frequency measurements (such as 32 GHz) can be used for detection of the onset of snow especially if the snowpack is dry.

Between November 11 and 16, 2019, there exists only a thin snow cover ( $h_S < 0.2$  m). Accordingly, on November 11, increasing  $T_{\text{air}}$  to  $\sim 5$  °C causes snow melt and a drop of  $< 2$  dB in  $\sigma_{\text{VV}}^0(f = 32 \text{ GHz})$  because: 1) due to the thin snowpack, volume scattering is negligible and 2) snow wetness causes high propagation loss. With  $T_{\text{air}}$  falling below 0 °C,  $\sigma_{\text{VV}}^0(f = 32 \text{ GHz})$  rises by about 1 dB from the evening of November 11 until the morning of November 14. Once again with  $T_{\text{air}} > 0$ °C from the afternoon of November 14 until late evening of November 15,  $\sigma_{\text{VV}}^0(f = 32 \text{ GHz})$  drops by  $\sim 2.5$  dB. The aforementioned issues together decrease  $\sigma_{\text{VV}}^0(f = 32 \text{ GHz})$  compared to thicker and/or dry snowpack. The fluctuations of  $T_{\text{air}}$  between November 21 and 29, 2019, induce daily fluctuations of  $WC_S$ . Similarly, as discussed in **Figure 8**, the amplitudes of daily  $\sigma_{\text{VV}}^0(f)$  fluctuations seen in **Figure 10** increase with increasing measurement frequency.

It is highlighted here that the onset of snow cover has no prominent signature on  $\sigma_{\text{VV}}^0(f = 6 \text{ GHz})$ , and it is practically undetectable by  $\sigma_{\text{VV}}^0(f = 2 \text{ GHz})$ . However, a similar investigation of measurements at all available frequencies suggests that reliable detection of the onset of snow cover is possible using  $\sigma_{\text{VV}}^0(f)$  at Ku- to Ka-bands.

### 3.2. Results from second Campaign in Sodankylä during Winter 2020/2021

**Figure 11** (a,b) shows the time series of co-polarized radar cross sections  $\sigma_{\text{VV,C}}(f)$  and  $\sigma_{\text{VV,G}}(f)$  measured approximately over the Canopy and treeless Ground areas, respectively (see **Figure 5** (d)). In **Figure 11** (a,b) radar cross sections are shown for the frequencies  $f = \{2,6,10,16,20,32\}$  GHz. It is noteworthy that the approach for the computation of normalized radar cross section  $\sigma_{pp}^0(f)$  ( $\equiv$  backscattering coefficients) from WBSCAT measurements, given in [1], assumes that the instrument is sufficiently far from the observed target area as is the case for example for airborne and satellite measurements. However, WBSCAT was installed at 19-m height above ground and looked into the canopy whose height is as much as 16 m. As a result, the conventional method for the computation of backscattering coefficients  $\sigma_{pp}^0(f)$  is not exactly applicable. Therefore, we demonstrate  $\sigma_{\text{VV}}(f)$  in dBsm (dB square meters). However, it is still possible to extract qualitative information by inspecting the temporal evolution of  $\sigma_{\text{VV}}(f)$  in response to ground and snow conditions and by comparing  $\sigma_{\text{VV,C}}(f)$  and  $\sigma_{\text{VV,G}}(f)$  to infer the differences between scattering from bare ground and the ground underneath canopy. **Figure 11** (c) – (e) show the time series of snow depth, precipitation intensity, and air temperature, respectively. These data are identical to the set shown in **Figure 6**, only repeated here for better readability next to the time series of  $\sigma_{\text{VV,C}}(f)$  and  $\sigma_{\text{VV,G}}(f)$ . Two vertical dashed lines are included in each panel in **Figure 11** to indicate the onset and melt of the snowpack.

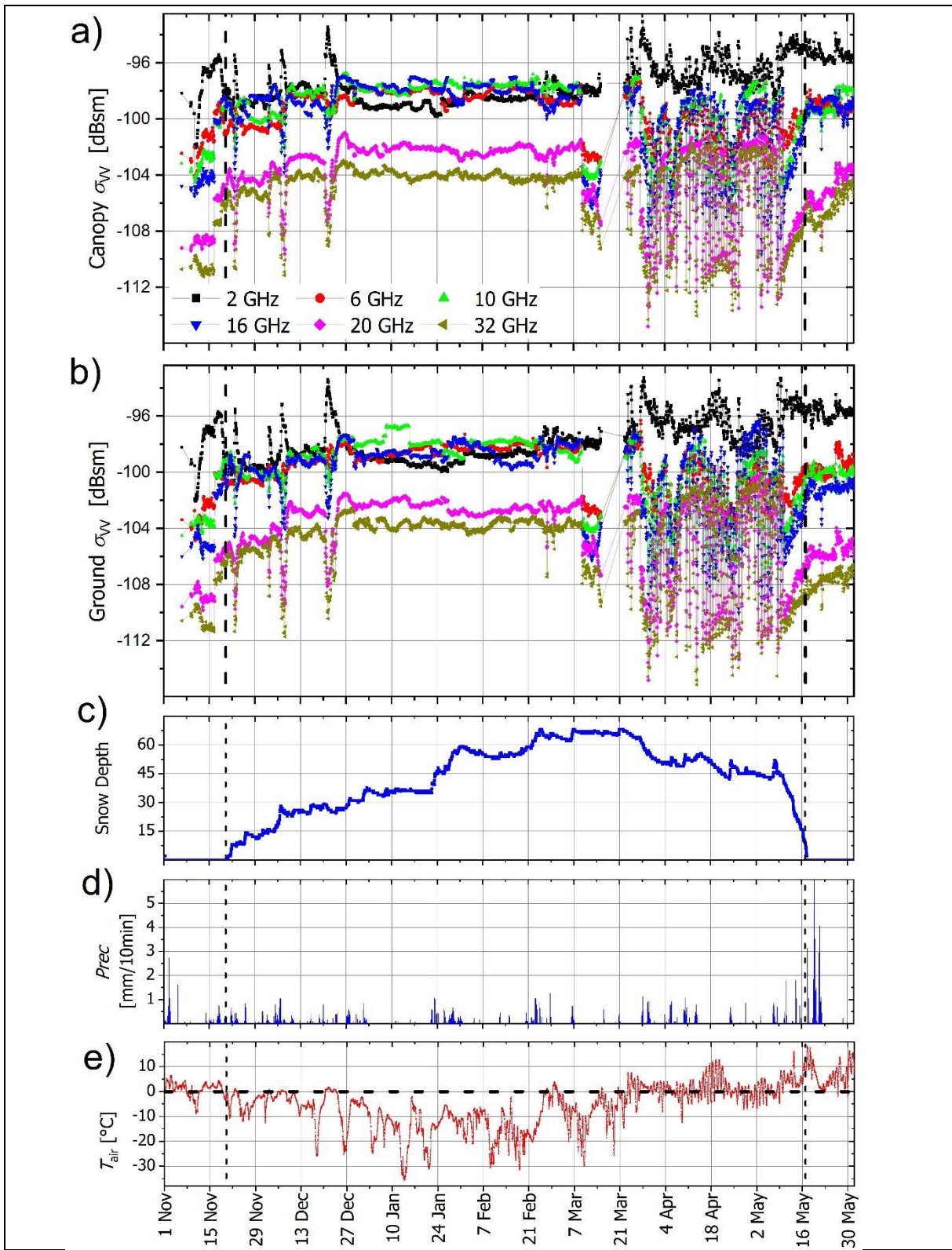


**Figure 11:** (a, b) time series of co-polarized radar cross sections  $\sigma_{VV,c}(f)$  and  $\sigma_{VV,G}(f)$  measured over the Canopy and treeless Ground areas, respectively (see **Figure 5** (d)). Time series of: (c) snow depth, (d) precipitation intensity, and (e) air temperature.

The response of  $\sigma_{VV,C}(f)$  and  $\sigma_{VV,G}(f)$ , especially at  $f > 2$  GHz, to the onset of snow cover is evident in **Figure 11** (a,b).  $\sigma_{VV}(f)$  increases by as much as 4 dB as a result of snow depth increasing from 0 cm to 15 cm. Between 27 December 2020 and 7 March 2021,  $\sigma_{VV,C}(f)$  and  $\sigma_{VV,G}(f)$  seem to be stable which itself is a sign of dry snow and cold winter conditions. As shown in [1] and discussed in Section 3.1., during cold winter period, backscattering still responds to precipitation, changes in the underlying ground and even SWE.

Between 27 March 2021 and 9 May 2021,  $\sigma_{VV,C}(f)$  and  $\sigma_{VV,G}(f)$  show daily fluctuations, which as shown in [1] and in Section 3.1. is a sign of snow melt. As expected, the amplitude of these fluctuations depends on the frequency of observation. In simplified terms, the higher the frequency, the stronger the fluctuations in response to snow wetness variations during the melting period (compare Section 3.1. specifically **Table 1**).

Other preliminary findings reveal increasing differences between  $\sigma_{VV,C}(f)$  and  $\sigma_{VV,G}(f)$  at a given frequency growing from snow cover times to snow-free times after winter. This is possibly a hint to the increased scattering effect and contribution of the canopy when it is unfrozen. Furthermore, this difference between frozen and unfrozen canopy conditions is generally larger at higher frequencies. This is because at longer wavelengths, propagation losses are smaller, and the scattering elements with dimensions comparable with the wavelengths are simply fewer and contributing less. At higher frequencies, small branches and even needle leaves contribute to backscattering. Therefore, during unfrozen times when the canopy becomes an effective part of total backscattering, these elements add to the total backscatter from the canopy.

## 4. THERMAL INERTIA ANALYSIS

Understanding the variability of snow thermal inertia and exploring synergies with microwave data can be useful for remote sensing perspectives, overall for improving the estimation of SWE, which is a crucial parameter in snow hydrology. In this context (WP 400), we conducted a dedicated analysis at the “Davos-Laret Remote Sensing Field Laboratory” [3], using a combination of different field data. The possibility to detect snowmelt periods and to get meaningful estimates of snow density from optical/thermal remote sensing is particularly relevant and, currently, it still represents a great challenge. In this Section of the Final Report (FR), we show the results related to the possibility to detect snow phases and snow density from thermal inertia and a preliminary comparison between thermal inertia, microwave time series and snow properties.

### 4.1. Data and Method

In the recent study [9] it is hypothesized that remotely sensed thermal inertia could be a useful indicator for snowmelt properties. Thermal inertia is a physical property of the surface, which determines “resistance” to temperature changes under seasonal and diurnal heating (e.g. [10]). Thermal inertia is described as,

$$P = \sqrt{k \cdot \rho \cdot c} \quad \text{in units of } [\text{J} \cdot \text{m}^{-2} \cdot \text{K}^{-1} \cdot \text{s}^{-1/2}] \quad (1)$$

where  $\rho$  is mass-density [ $\text{kg} \cdot \text{m}^{-3}$ ],  $k$  is the thermal conductivity [ $\text{J} \cdot \text{m}^{-1} \cdot \text{s}^{-1} \cdot \text{K}^{-1}$ ] and  $c$  is the specific heat [ $\text{J} \cdot \text{kg}^{-1} \cdot \text{K}^{-1}$ ]. If thermal inertia changes in space and time, it could be possible to generate maps that can be used to monitor specific snow parameters.

By using remotely sensed data, the so-called apparent thermal inertia of snow ( $AP_s$ ) can be computed instead of thermal inertia  $P$  defined by Equation (1). At the Davos-Laret site  $AP_s$  has been computed starting from available field data and using the formulation proposed by [10]:

$$AP_s = \frac{(1-\alpha)SW_{\text{in}}}{\Delta T_{(t_2-t_1)}} \frac{A_1 \cos(\omega t_1 - \delta_1) - \cos(\omega t_2 - \delta_1)}{\sqrt{\omega} \sqrt{1 + \frac{1}{b} + \frac{1}{2b^2}}} \quad \text{in units of } [\text{J} \cdot \text{m}^{-2} \cdot \text{K}^{-1} \cdot \text{s}^{-1/2}] \quad (2)$$

$\alpha$  is the snow shortwave broadband albedo averaged between 13:00 and 15:00 (local time),  $\Delta T$  is the surface temperature difference between the night-time and the day-time temperatures measured at times  $t_2$  (13:00 and 15:00) and  $t_1$  (4:00 and 6:00), respectively;  $SW_{\text{in}}$  is the daily average shortwave incoming radiation;  $\omega$  is the angular velocity of Earth rotation [ $\text{rad} \cdot \text{s}^{-1}$ ];  $A_1$  and  $b$  are the coefficients of a first-order approximation of the Fourier series (for details, see [11]), while  $\delta_1$  [rad] is the phase difference between surface temperature and shortwave incoming radiation that can be retrieved straightforward under the hypothesis that the time at which surface temperature reaches the maximum value is known [12].

All the parameters have been computed from data recorded during the hydrological years 2016/2017, 2018/2019 and 2019/2020 (until 24/02/2020). A summary list of the data is shown in **Table 2**.

<b>Table 2:</b>		Description of the available and computed data starting from the AWS and the Tower stations.	
<b>Data from</b>	<b>Name</b>	<b>Unit</b>	<b>Description (original parameter name)</b>
AWS	Tsurf	°C	Mean snow surface temperature (TSS_AVG)
AWS	SWin	W/m <sup>2</sup>	Mean incoming SW radiation (PYR_IN_W_AVG)
AWS	LWin	W/m <sup>2</sup>	Mean incoming LW radiation (PIR_IN_W_AVG)
AWS	SWout	W/m <sup>2</sup>	Mean reflected SW radiation (PYR_OUT_W_AVG)
AWS	LWout	W/m <sup>2</sup>	Mean emitted LW radiation (PIR_OUT_W_AVG)
AWS	SWE	kg/m <sup>2</sup>	Water equivalent of snow cover (SCALE_SW_TOT_AVG)
AWS	HS	mm	Mean snow depth (HS_3)
Tower	Tsurf_T	°C	Snow surface temperature from radar tower (TIRmean)
Eq.	Tsurf_LW	°C	$T_{surf\_LW} = \sqrt[4]{LW_{out}/sb}$ sb = Stefan-Boltzmann constant
Eq.	Albedo	-	Albedo = LWout / LWin
Eq.	Density_aws	Kg / m <sup>3</sup>	Density_aws = SWE / HS, Lonas et al. 2009
Eq.	APs	J/m <sup>2</sup> K s <sup>1/2</sup>	Apparent thermal inertia, Colombo et al., 2019, Eq. 2
Eq.	Density_APs	Kg / m <sup>3</sup>	Density estimated from APs, by using relation in Colombo et al., 2019 Fig. 3

Beside other properties, snow density is an essential variable for quantifying the amount of water contained in the snowpack and the water availability at the catchment scale (e.g. [13]). In particular, we were interested in testing the relationship between  $AP_s$  and snow variables that affect snowpack's thermal properties, primarily snow density. Such analysis has been conducted using linear and non-linear regressions to identify the best empirical model.

#### 4.2. Snow Phases Detection

**Figure 12** shows the temporal behaviour of the main snow parameters and snow thermal inertia. The complex interactions between all of these parameters may reveal the different phases of snow accumulation and melting. Accumulation periods and snow melting phases (i.e., warming, ripening and output phases) can be traditionally identified for each year mainly considering snow depth and temperature variations.

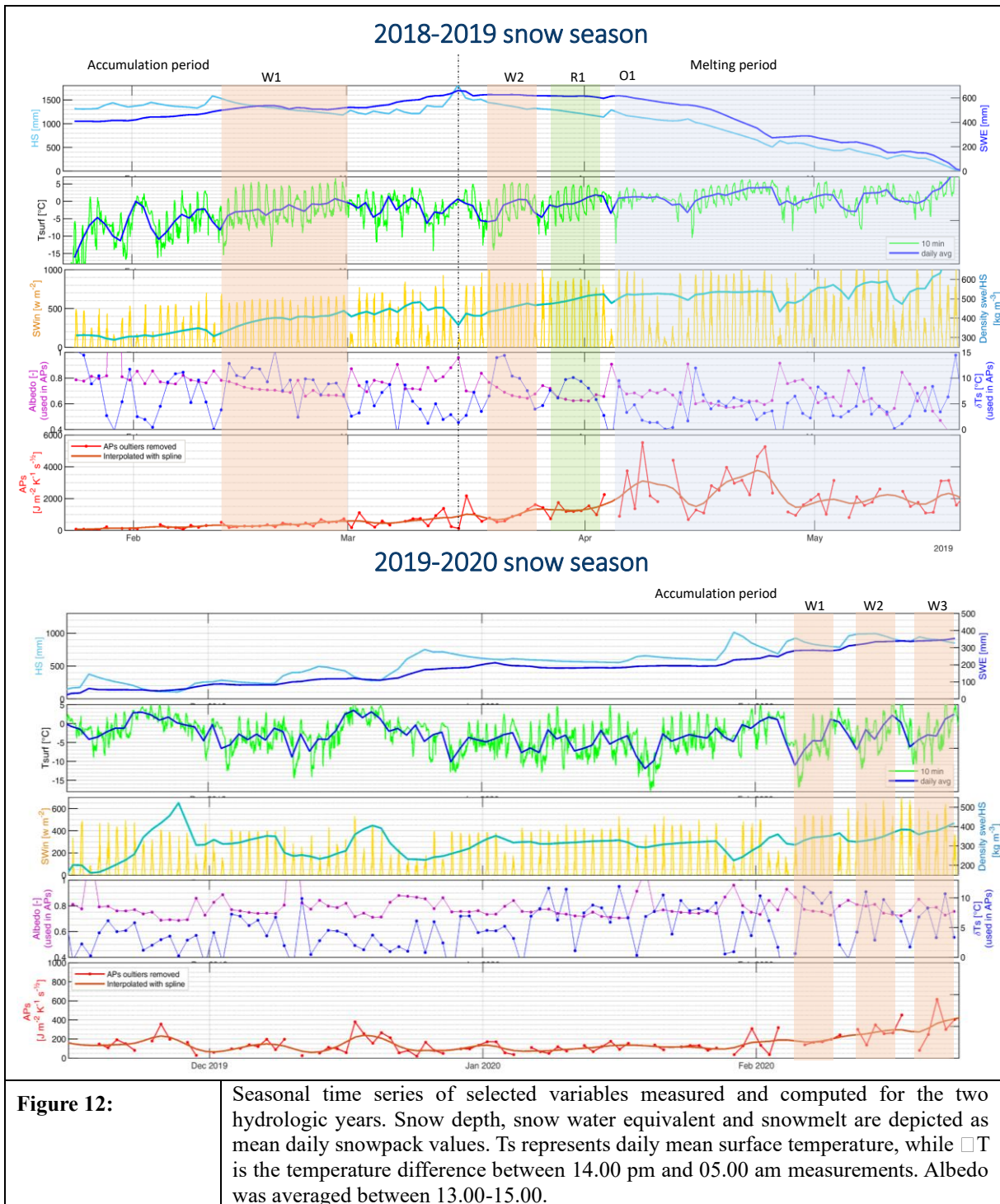


**Figure 12:**

Seasonal time series of selected variables measured and computed for the two hydrologic years. Snow depth, snow water equivalent and snowmelt are depicted as mean daily snowpack values.  $T_s$  represents daily mean surface temperature, while  $\Delta T$  is the temperature difference between 14.00 pm and 05.00 am measurements. Albedo was averaged between 13.00-15.00.

In both years, thermal inertia changes in time. During winter, in accumulation phase,  $AP_s$  show a low variability with mean value of  $220 \text{ J} \cdot \text{m}^{-2} \cdot \text{K}^{-1} \cdot \text{s}^{-1/2}$ . Greater variability and higher  $AP_s$  values can be observed in late season, where snow metamorphism occurs and the appearance of liquid water on the surface of the snow can increase apparent thermal inertia ( $\sim 3000 \text{ J} \cdot \text{m}^{-2} \cdot \text{K}^{-1} \cdot \text{s}^{-1/2}$ ). During March and April, intermediate values of  $AP_s$  ranging from 500 to  $1500 \text{ J} \cdot \text{m}^{-2} \cdot \text{K}^{-1} \cdot \text{s}^{-1/2}$  can be generally observed, indicating the transition between

warming and snowmelt processes. In the meltwater output phase the  $AP_s$  values increase over  $4000 \text{ J} \cdot \text{m}^{-2} \cdot \text{K}^{-1} \cdot \text{s}^{-1/2}$ . Highest  $AP_s$  values are often associated to uncertain estimates of  $\Delta T$  and these values were filtered out. In summary, this analysis (and Section 4.4) reinforce and indicate that thermal inertia can be a useful metric to evaluate different snow conditions.

### 4.3. Relation between $AP_s$ and Snow Density

A significant power law relationship between  $AP_s$  and snow density was found for the investigated years. The respective **Figure 13** shows the relationships between surface snow density and  $AP_s$  calculated from AWS data ( $R^2 = 0.68$ ) and from tower data ( $R^2 = 0.59$ ).

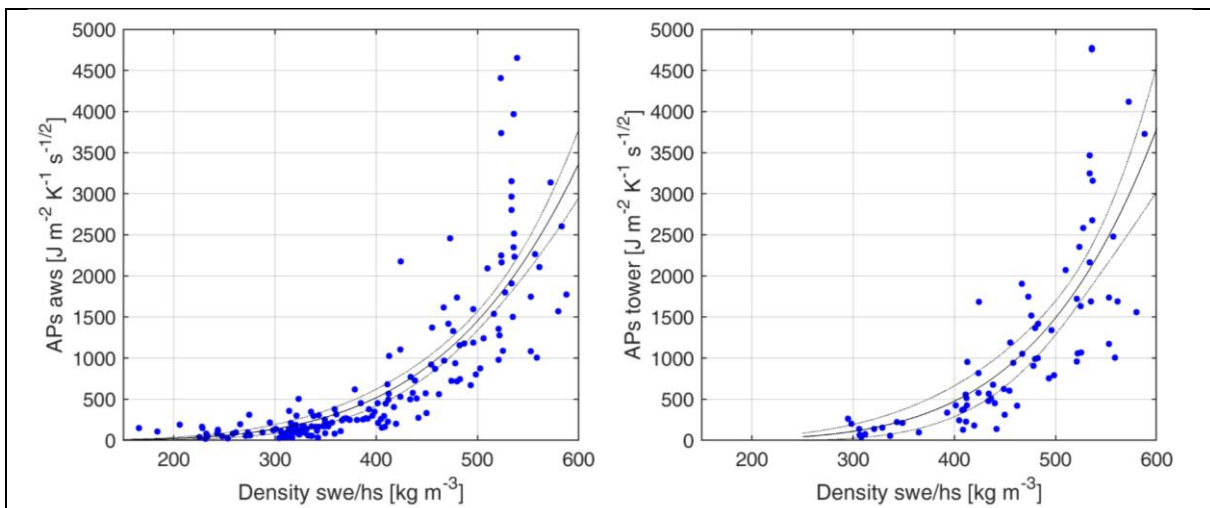


**Figure 13:** Correlation between  $AP_s$  and mean snow density for the investigated years (left, from AWS; right from tower station). Snow density is computed as  $SWE/h_s$ . The regression is statistically significant ( $p < 0.001$ ,  $\alpha = 0.05$ ) and the 95% prediction boundary of the functions are represented.

Overall, this result consolidates the findings of [9]. During the different snow phases,  $AP_s$  takes distinct values in all considered hydrological years.  $AP_s$  values in the accumulation period are almost constant with average snow density of about  $250 - 300 \text{ kg m}^{-3}$ ; during warming and ripening,  $AP_s$  assumes intermediate values with snow density of  $300 - 400 \text{ kg m}^{-3}$ , whilst in the output phases mean values of  $AP_s$  are higher and more variable and corresponding to the highest snow density values. Snow density has been also estimated by using the relationship described in [9] and results compared with those obtained from  $SWE/h_s$  (data not shown).

### 4.4. $AP_s$ and Passive L-band Snow Variables Comparison

**Figure 14** shows the seasonal time-series of selected variables available for the 2016/2017 hydrologic year. **Figure 14** (top panel) show the time evolution of the snow depth and the starting of the snowmelt at the beginning of March is clearly detectable. Middle panel shows the behaviour of the snow liquid water content, estimated from L-band radiometry (Section 2. ) using the approaches explained in [5] and the seasonal trend of  $AP_s$ .  $AP_s$  begins to increase

around the days where snow depth decreases, indicating the starting of the warming phase and hence the snowmelt period. A simple threshold approach on  $AP_s$  (e.g.  $500 \text{ J} \cdot \text{m}^{-2} \cdot \text{K}^{-1} \cdot \text{s}^{-1/2}$  corresponding to the end of the accumulation and warming phase), may help to separate cold dry snow or no melting snow with density values lower than  $300 \text{ kg m}^{-3}$  and to identify dates with higher snow density where snow is clearly in the output phase. We can also observe the ability of the L-band radiometer method to infer snow liquid water content before this phase transition. Snow liquid water content and snow thermal inertia are only poorly related, so that microwave and optical/thermal data can be exploited to retrieve different parameters and to improve snow hydrological models. **Figure 14** (bottom panel) shows the comparison between snow density retrieved from close-range passive L-band measurements [14] and  $AP_s$ . Snow density estimates from  $AP_s$  and from L-band radiometry are difficult to interpret, although a subtle agreement can be observed at the beginning of the accumulation period. Moreover, field measurements are only adequately related with the  $AP_s$  and snow density estimated from L-band radiometry (data not shown) and further investigations are needed to better understand the contribution of  $AP_s$  and L-band for snow density retrieval. In principle, it seems that snow liquid water column can be retrieved from multi-angle L-band measurements, while snow density could be inferred from the  $AP_s$  signal.

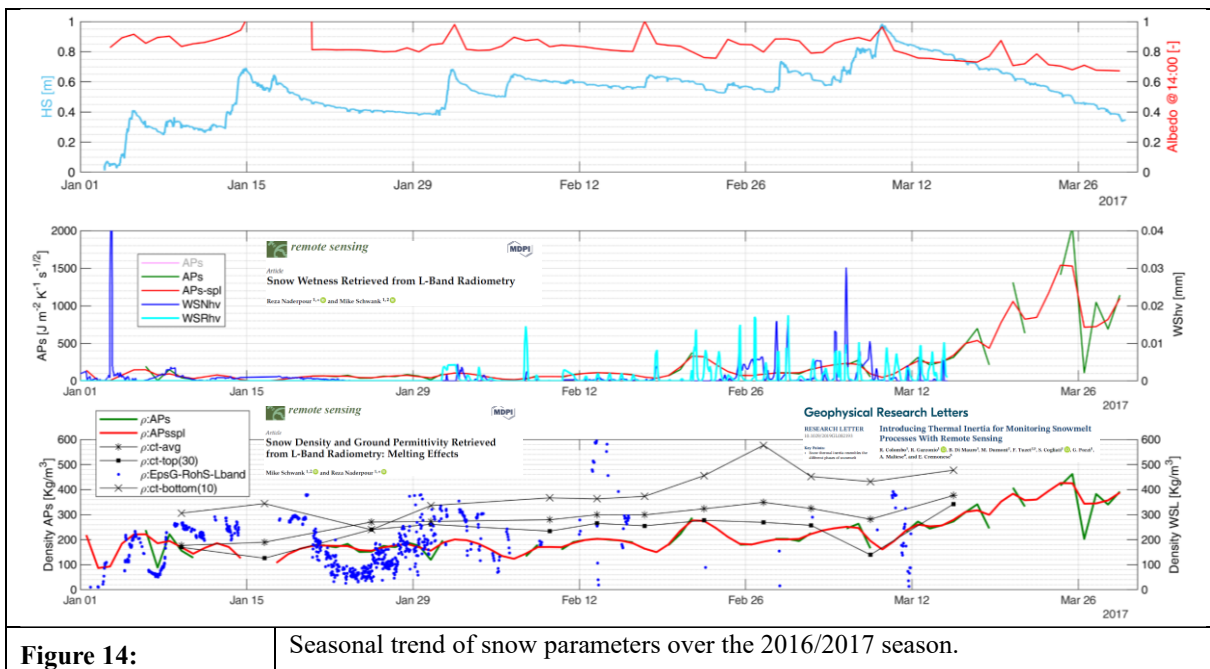


Figure 14:

Seasonal trend of snow parameters over the 2016/2017 season.

#### 4.5. Conclusions

Results provided in this study evidences that snowmelt phases can be recognized, and mean snow density can be estimated from thermal inertia observations. These results are of particular interest since  $AP_s$  is a variable that can be directly estimated from remotely sensed data. Thus,

we believe that the use of snow thermal inertia may contribute to open new applications and perspectives in Earth Observation of the cryosphere, in particular for snow hydrology and periglacial processes at the catchment scale. Currently, several satellite missions are devoted to the study of the cryosphere, but unfortunately none of these feature sufficient day/night revisit time, high spatial resolution and a combination of optical and thermal bands, suitable to monitor snow thermal inertia from space. However, optical and thermal data are often affected by the presence of clouds, so that monitoring thermal inertia from space must be consistent with other information. In this context, a strategy combining existing or future microwave radiometer and radar, and optical and thermal missions could be defined with the perspective to specifically target a better estimation of the snow water equivalent, which is the parameter directly affecting the availability of water. Here, we have only partially addressed the combination between different sources of data and further studies are needed to better accomplish their assimilation in view of a better understanding of cryosphere processes.

## 5. REFERENCES

- [1] R. Naderpour, M. Schwank, D. Houtz, C. Werner, and C. Mätzler, "Wideband Backscattering From Alpine Snow Cover: A Full-Season Study," *IEEE Transactions on Geoscience and Remote Sensing*, pp. 1-15, 2021.
- [2] R. Naderpour, M. Schwank, D. Houtz, and C. Mätzler, "L-Band Radiometry of Alpine Seasonal Snow Cover: 4 Years at the Davos-Laret Remote Sensing Field Laboratory," *IEEE Journal of selected topics in applied earth observations and remote sensing*, (accepted for publication) 2022.
- [3] R. Naderpour, M. Schwank, and C. Mätzler, "Davos-Laret Remote Sensing Field Laboratory: 2016/2017 Winter Season L-Band Measurements Data-Processing and Analysis," *Remote Sensing*, vol. 9, no. 11, p. 1185, 2017.
- [4] J. Jorge Ruiz *et al.*, "Sodsar: A tower-based 1–10 ghz sar system for snow, soil and vegetation studies," *Sensors*, vol. 20, no. 22, p. 6702, 2020.
- [5] R. Naderpour and M. Schwank, "Snow Wetness Retrieved from L-Band Radiometry," *Remote Sensing*, vol. 10, no. 3, p. 359, 2018.
- [6] M. Christian, "Applications of SMOS over terrestrial ice and snow," presented at the Proc. 3rd SMOS Workshop, Oberpfaffenhofen, Germany: DLR, 2001.
- [7] H. Rott and C. Mätzler, "Possibilities and limits of synthetic aperture radar for snow and glacier surveying," *Annals of Glaciology*, vol. 9, pp. 195-199, 1987.
- [8] M. Proksch *et al.*, "MEMLS3&a: Microwave Emission Model of Layered Snowpacks adapted to include backscattering," *Geoscientific Model Development*, vol. 8, no. 8, pp. 2611-2626, 2015.
- [9] R. Colombo *et al.*, "Introducing thermal inertia for monitoring snowmelt processes with remote sensing," *Geophysical Research Letters*, vol. 46, no. 8, pp. 4308-4319, 2019.
- [10] G. S. Nearing, M. S. Moran, R. L. Scott, and G. Ponce-Campos, "Coupling diffusion and maximum entropy models to estimate thermal inertia," *Remote sensing of environment*, vol. 119, pp. 222-231, 2012.
- [11] A. Maltese, P. Bates, F. Capodici, M. Cannarozzo, G. Ciruolo, and G. La Loggia, "Critical analysis of thermal inertia approaches for surface soil water content retrieval," *Hydrological Sciences Journal*, vol. 58, no. 5, pp. 1144-1161, 2013.
- [12] Y. Xue and A. Cracknell, "Advanced thermal inertia modelling," *Remote Sensing*, vol. 16, no. 3, pp. 431-446, 1995.
- [13] M. Sturm, B. Taras, G. E. Liston, C. Derksen, T. Jonas, and J. Lea, "Estimating snow water equivalent using snow depth data and climate classes," *Journal of Hydrometeorology*, vol. 11, no. 6, pp. 1380-1394, 2010.
- [14] M. Schwank and R. Naderpour, "Snow Density and Ground Permittivity Retrieved from L-Band Radiometry: Melting Effects," *Remote Sensing*, vol. 10, no. 2, p. 354, 2018.

ESTEC

Deliverable D2+D2a: Preliminary and Final Data Acquisition Report for Davos-Laret during Winter 2019/2020 Campaign

*SnowLab-NG*

28. Nov. 2020

**ESA CONTRACT NO. 4000130865/20/NL/FF/AN  
with  
WSL-BIRMENS DORF**

**SnowLab-NG**

**Deliverables D2 and D2a:**

**D2: Preliminary Data Acquisition Report for Davos-Laret  
during Winter 2019/2020 campaign  
D2a: Final DAR for Entire Season of Davos-Laret Campaign  
(update of D2)**

**WSL-BIRMENS DORF REFERENCE NUMBER: WSL-Birmensdorf\_ESTEC/SnowLab-NG**

Created: 25. August 2020

Authors:

Mike Schwank, WSL-Birmensdorf  
Reza Naderpour, WSL-Birmensdorf  
Derek Houtz, WSL-Birmensdorf  
Henning Löwe, WSL-Davos (SLF)



Charles Werner, GAMMA

 **GAMMA REMOTE SENSING**

## ESTEC

Deliverable D2+D2a: Preliminary and Final Data Acquisition Report for Davos-Laret during Winter 2019/2020 Campaign

*SnowLab-NG*

*28. Nov. 2020*

**TABLE OF CONTENTS**

Acronyms and Abbreviations ..... 4

1. Introduction ..... 5

2. Data Acquisition Plan..... 7

3. Passive Microwave, IR & Soil In-Situ measurements ..... 8

    3.1. Approach to Achieve Calibrated L-band Brightness Temperatures ..... 8

        3.1.1. 3<sup>rd</sup> Calibration Point ( $T_{100K}, U_{100K}^{p,ch}$ )..... 9

        3.1.2. Approach to achieve calibrated  $T_{BL}^p$  ..... 10

        3.1.3. RFI filtering..... 11

    3.2. Approach to achieve Calibrated X-band Brightness Temperatures..... 11

    3.3. Approach to achieve InfraRed Temperatures ..... 12

    3.4. L- & X-band Brightness Temperatures and InfraRed & Air Temperatures..... 12

    3.5. Segregated L-band Brightness Temperatures of “Large Reflector Area”..... 17

    3.6. Snow liquid Water Column ..... 20

        3.6.1. Retrieval Approach..... 20

        3.6.2. Retrieved  $WC_S$ ..... 21

4. In-Situ measurements ..... 23

    4.1. Soil..... 23

    4.2. Snow ..... 26

5. WBScat Measurements ..... 27

    5.1. Data Acquisition Process ..... 28

    5.2. Post Processing of WBScat Data ..... 30

    5.3. Extraction of Natural and Charcoal-Sand Area Signatures ..... 32

    5.4. Initial Analysis of WBScat Data..... 33

6. Lessons Learned ..... 40

7. References ..... 41

## ESTEC

Deliverable D2+D2a: Preliminary and Final Data Acquisition Report for Davos-Laret during Winter 2019/2020 Campaign

*SnowLab-NG*

*28. Nov. 2020*

### **ACRONYMS AND ABBREVIATIONS**

AWS	Automatic Weather Station
EC	Electrical Conductivity
IR	InfraRed
MIRA	MIcrowave RAdiometer
PDF	Probability Distribution Function
PIMA	Power Control Interface Microwave Assembly
RFI	Radio Frequency Interference
SAR	Synthetic Aperture Radar
SWE	Snow Water Equivalent
WBScat	Wide-Band Scatterometer
WTC	WBscat Temperature and Power Controller

## 1. INTRODUCTION

This report is D2: “Preliminary Data Acquisition Report for Davos-Laret during Winter 2019/2020 campaign” and D2a: “Final DAR for Entire Season of Davos-Laret Campaign (update of D2)”. It includes the close-range passive- and active microwave measurements, as well as accompanying meteorological and in-situ data collected at the Davos-Laret Remote Sensing Field Laboratory (Switzerland) [1] during the Winter campaign 2019/2020. The presented measurements also include InfraRed (IR) data measured with an IR-radiometer installed at the aperture of the L-band radiometer antenna moving every hour along three azimuth and seven elevation angles (the respective observation azimuth angle  $\varphi$  and elevation angle  $\theta$  is introduced in Figure 1 and in D1 [2]). Further, auxiliary data (air temperature  $T_{\text{air}}$ , snow surface temperature  $T_S$ , snow height  $h_S$ , precipitation  $P$ , ratios between incoming and reflected short- and long-wave radiation, Snow Water Equivalent (SWE)) measured by the Automatic Weather Station (AWS) installed at the test-site are shown.

**FIGURE 1** below shows the schematics of the Winter 2019–2020 Davos-Laret campaign setup. This figure shows the positioning of the in-situ soil sensor network over three transects, the artificially created charcoal-sand area common to both active (WBScat) and passive (radiometers) instruments, the trapezoidal reflector area for passive measurements, and the natural soil area for active and passive measurements.

Beyond what is defined for D2 and D2a we also provide time-series of  $T_{\text{BL,R}}^{p,\theta}$  representing segregated L-band brightness temperatures of the “large-Reflector-area” (see D1 [2]). Furthermore, we present time-series of Snow liquid Water-Column  $WC_S$  retrieved from  $T_{\text{BL,R}}^{p,\theta}$ . The reason for including time-series of  $WC_S$  already as part of D2/D2a is because it is seen as a fundamental reference dataset valuable for the scientific evaluation of quasi-simultaneous active- and passive microwave and IR measurements. Sensitivities of these measurements with respect to the amount of liquid water in the snowpack can be explored from time-series of  $WC_S$  retrieved from  $T_{\text{BL,R}}^{p,\theta}$ . Measurement data from the Winter 2019/2020 is presented in this report and delivered to ESA within D2/D2a of SnowLab-NG project.

Furthermore, we outline the procedures developed and applied to achieve calibrated L-band brightness temperatures  $T_{\text{BL},\phi}^{p,\theta}$  at horizontal and vertical polarization  $p = (H, V)$  measured at azimuth angles  $\varphi = (75^\circ, 125^\circ, 180^\circ)$  and at elevation angles  $\theta = (30^\circ, 35^\circ, 40^\circ, 45^\circ, 50^\circ, 55^\circ, 60^\circ)$ . The methodology developed to segregate  $T_{\text{BL,R}}^{p,\theta}$  from combining  $T_{\text{BL},180^\circ}^{p,\theta}$  measured along the azimuth  $\varphi = 180^\circ$  over the “large reflector area“ with  $T_{\text{BL},125^\circ}^{p,\theta}$  measured at  $\varphi = 125^\circ$  toward “natural area“ is outlined. Further, the retrieval approach used to achieve  $WC_S$  from  $T_{\text{BL,R}}^{p,\theta}$  is explained.

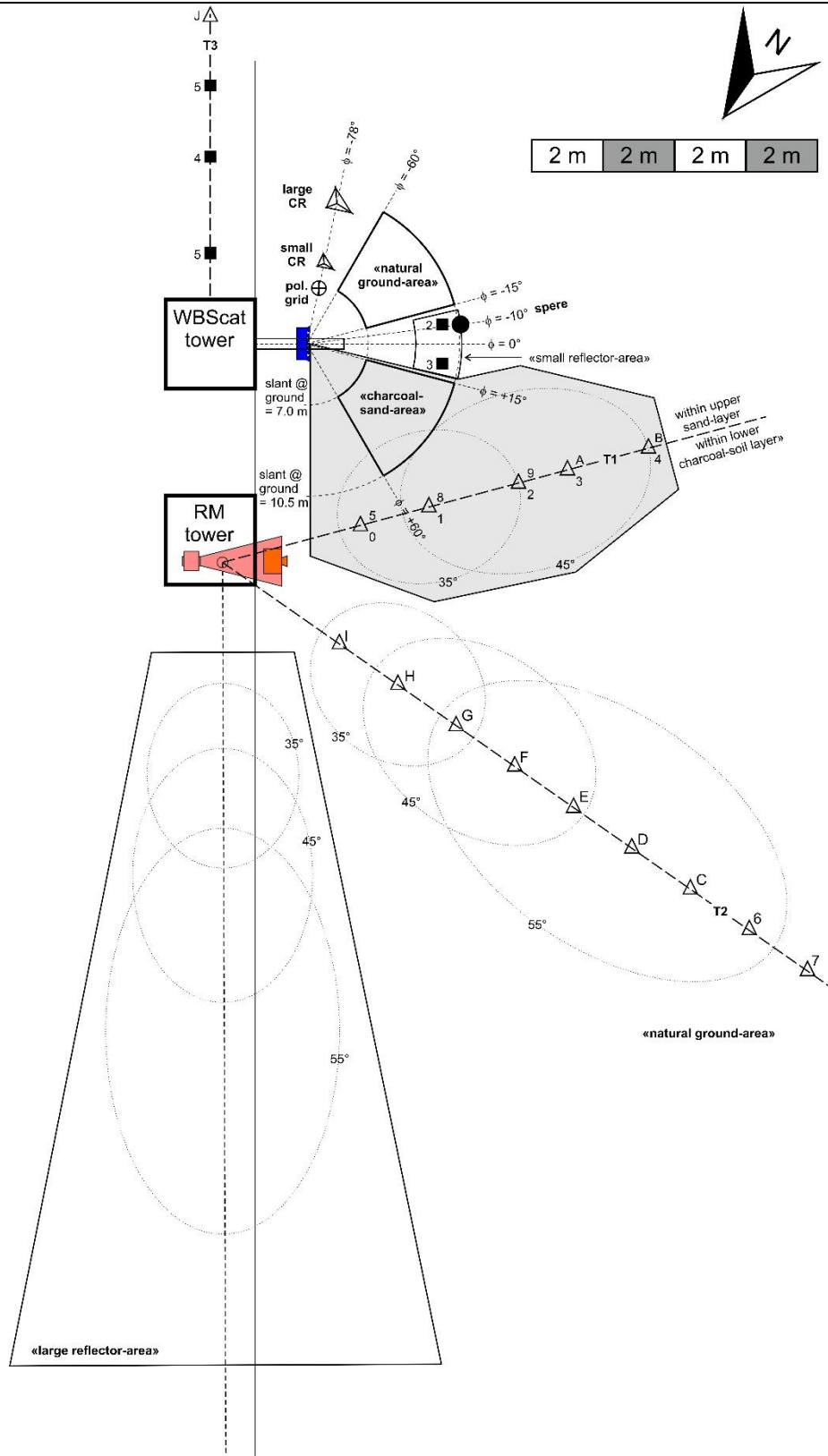


**FIGURE 1.** Schematics of the measurement setup for Winter 2019/2020 campaign at the Davos-Laret Remote Sensing Field Laboratory. Triangles and black squares represent SMT-100 and 5TE sensors, respectively.

Before presenting active measurement data from WBScat, the data acquisition process is described. Additionally, the step-by-step method for post processing of WBScat data is explained to familiarize the reader with the applied process through which calibrated radar backscatter is computed.

## 2. DATA ACQUISITION PLAN

The Davos Laret Remote Sensing Field Laboratory (48°50'53''N 9°52'19''E) in Switzerland is a 50 m × 50 m area with an approximate elevation of 1,450 m above sea level. The ground is mostly flat with some smooth slopes on the north-western side of the site. The valley, including the site area, is surrounded by mountains with an average height difference of ~400 m with respect to the site. The site area is surrounded by Lake Schwarz on the north-western side, canopy forest on the south-eastern side and local buildings on the north-eastern and south-western sides. The spring and summertime vegetation cover of the site is grass.

In total, five main measurement systems were operated during the Winter 2019/2020 campaign in Davos-Laret Remote Sensing Field Laboratory including WBScat, L-band radiometer (OMRA), X-band radiometer (MIRA), Infrared Radiometer and in-situ soil sensors. A coordinated data acquisition plan was devised and implemented to ensure comprehensive data collection for all instruments, and minimum interference between active and passive remote sensing. **FIGURE 2** shows the schedule for different types of measurements as well as data backup.

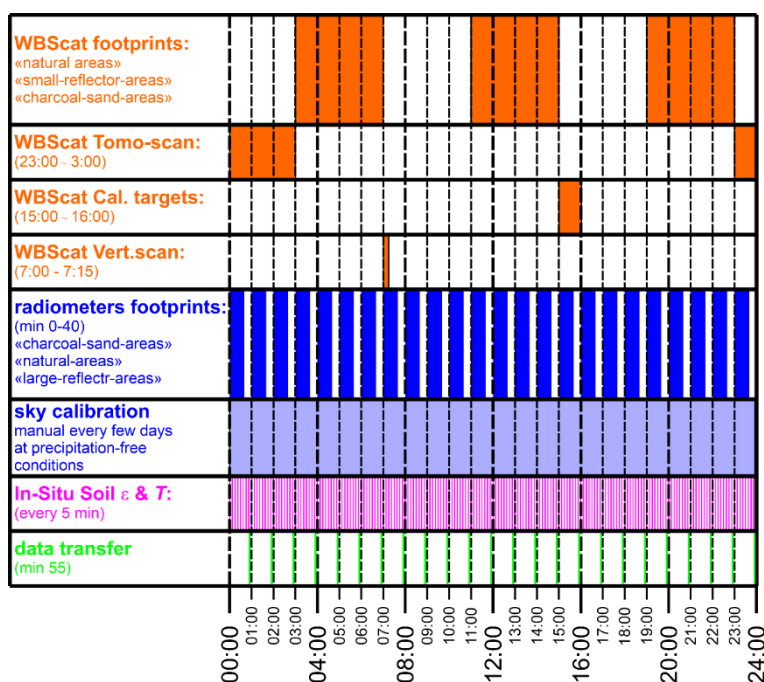


**FIGURE 2.** Standard daily acquisition schedule for the Winter campaign 2019/2020 in Davos-Laret.

### 3. PASSIVE MICROWAVE, IR & SOIL IN-SITU MEASUREMENTS

In this section, firstly the approach for calibration of each of the three radiometers' data is presented. Secondly, the time series of these calibrated measurements are presented and briefly discussed. Sections 3.5. and 3.6. specifically address the segregated L-band  $T_{BL,R}^{p,\theta}$  originating exclusively from the “large reflector area” (Figure 1 and D1 [2]), and show the time series of Snow liquid Water Column  $WC_S$  based on  $T_{BL,R}^{p,\theta}$ .

#### 3.1. Approach to Achieve Calibrated L-band Brightness Temperatures

The L-band radiometer OMRA was deployed at the Davos-Laret site during the winter campaign 2019/2020. OMRA was built by WSL-Birmensdorf which was as a subcontractor of GAMMA leading the precursor CCN of the SnowLab-NG campaign (SnowLab4000117123/16/NL/FF/mg). Details and technical specifications of OMRA are provided in [2].

OMRA is equipped with two internal resistive matched loads acting as a Cold noise Source (CS) and a Hot noise Source (HS). In theory, knowledge of the physical temperatures  $T_{HS}$  and  $T_{CS}$  of these 50- $\Omega$  matched sources as well as the respective OMRA voltage readings (raw data)  $U_{HS}^{ch}$  and  $U_{CS}^{ch}$  is sufficient to achieve calibrated brightness temperatures  $T_{BL}^{p,ch}$  of footprints from corresponding raw data  $U^{p,ch}$ . However, this would assume perfect measurements of radiometer raw-data (voltages) and perfect temperature measurements of HS and CS. Further, temperatures  $T_{HS} \approx 45^\circ \text{C}$  and  $T_{CS} \approx 5^\circ \text{C}$  are relatively close to each other and outside the range of brightness temperatures expected for footprint measurements. This implies that errors can occur in  $T_{BL}^{p,ch}$  derived from  $U^{p,ch}$  if computed simply based on linear extrapolation of the two nearby calibrations points  $(T_{HS}, U_{HS}^{ch})$  and  $(T_{CS}, U_{CS}^{ch})$  in OMRA's temperature-voltage domain. These errors in  $T_{BL}^{p,ch}$  result from uncertainties in  $(T_{HS}, U_{HS}^{ch})$  and  $(T_{CS}, U_{CS}^{ch})$  and from temperature-dependent gain changes of OMRA. To reduce these errors we consider a 3<sup>rd</sup> reference point  $(T_{100K}, U_{100K}^{p,ch})$  calibrated from sky measurements performed at  $\varphi = 190^\circ$  and  $\theta = 140^\circ$ . Noise temperature  $T_{100K} = 100 \text{ K}$  of this 3<sup>rd</sup> calibration point is closer to footprint brightness temperatures and therefore reduces errors in  $T_{BL}^{p,ch}$  associated with the mentioned linear extrapolation of only two reference points.

Section 3.1.1. outlines the approach used to determine the 3<sup>rd</sup> calibration point  $(T_{100K}, U_{100K}^{p,ch})$  from sky measurements. Section 3.1.2. explains the approach to achieve calibrated footprint  $T_{BL}^{p,ch}$  based on  $U^{p,ch}$  and all three calibration points  $(T_{HS}, U_{HS}^{ch})$ ,  $(T_{CS}, U_{CS}^{ch})$ , and  $(T_{100K}, U_{100K}^{p,ch})$ . Finally, Section 3.1.3. explains the method to identify distortions in  $T_{BL}^{p,ch}$  due to Radio Frequency Interferences (RFI).

### 3.1.1. 3<sup>rd</sup> Calibration Point ( $T_{100K}, U_{100K}^{p,ch}$ )

The Hot- (HS) and Cold (CS) matched 50  $\Omega$  noise Sources implemented in OMRA are kept at constant physical temperatures  $T_{HS} \approx 45^\circ \text{C}$  and  $T_{CS} \approx 5^\circ \text{C}$ . Noise temperatures of the HS and CS are considered equal to their measured physical temperatures. Other components (for example Low Noise Amplifiers (LNA), filters, isolators) of OMRA's RadioMeter Assembly (RMA) are mounted on a metal-plate of large thermal mass with continuously measured temperature  $T_{\text{plate}}$ . Accordingly, OMRA's gain and inherent noise are affected by variations in  $T_{\text{plate}}$ . This effect is accounted for by performing sky measurements over a range of  $T_{\text{plate}}$  to yield data-pairs ( $T_{\text{RMA,sky}}^p, U_{\text{sky}}^{p,ch}(T_{\text{plate}})$ ) of noise temperatures  $T_{\text{RMA,sky}}^p$  at the RMA-inputs  $p = (H, V)$  and radiometer raw-data (voltages)  $U_{\text{sky}}^{p,ch}(T_{\text{plate}})$  measured at  $T_{\text{plate}}$ . Here,  $ch = (1, 2)$  indicate the two frequency channels measured by OMRA within the protected part 1.400 GHz – 1.427 GHz of the L-band (1 GHz – 2 GHz). Noise temperature  $T_{\text{RMA,sky}}^p$  are computed from simulated  $T_{\text{sky}}$  at the antenna aperture:

$$T_{\text{RMA,sky}}^p = T_{\text{sky}} + \Delta T_{\text{TL}}^p \quad (1)$$

We used the model outlined in [3] to simulate  $3.5 \text{ K} \leq T_{\text{sky}} \leq 5 \text{ K}$  for measured air temperature  $T_{\text{air}}$ , the sky observation nadir angle  $\theta = 140^\circ (= 40^\circ \text{ relative to zenith})$ , and the altitude  $Z = 1.4 \text{ km}$  above sea level of the Davos-Laret site.  $\Delta T_{\text{TL}}^p$  in equation (1) expresses the thermal noise added via Transmission Losses (TL) between the antenna and the RMA input-ports:

$$\Delta T_{\text{TL}}^p = (1 - t_{\text{TL}}^p)(T_{\text{air}} - T_{\text{sky}}) \quad (2)$$

Respective transmissivity  $t_{\text{TL}}^p$  is mainly due to losses  $L_{\text{TL}}^p = 0.20 \text{ dB}$  of the cables connecting the antenna ports  $p = (H, V)$  to the corresponding RMA input-ports:

$$t_{\text{TL}}^p = 10^{-L_{\text{TL}}^p/10} \quad (3)$$

Accordingly, each sky measurement performed at measured  $T_{\text{air}}$  and  $T_{\text{plate}}$  yields the data pairs ( $T_{\text{RMA,sky}}^H, U_{\text{sky}}^{H,1}(T_{\text{plate}})$ ), ( $T_{\text{RMA,sky}}^H, U_{\text{sky}}^{H,2}(T_{\text{plate}})$ ), ( $T_{\text{RMA,sky}}^V, U_{\text{sky}}^{V,1}(T_{\text{plate}})$ ), ( $T_{\text{RMA,sky}}^V, U_{\text{sky}}^{V,2}(T_{\text{plate}})$ ). Next, we apply a linear fit to each of these four pairs of data ( $T_{\text{RMA,sky}}^p, U_{\text{sky}}^{p,ch}(T_{\text{plate}})$ ) and the two data pairs ( $T_{\text{CS}}, U_{\text{CS}}^{ch}$ ) and ( $T_{\text{HS}}, U_{\text{HS}}^{ch}$ ) associated with the internal CS and HS measured at  $ch = (1, 2)$  at the same time and therefore at the same  $T_{\text{plate}}$ . **FIGURE 3** shows an example for  $T_{\text{air}} = 16.7^\circ \text{C}$  and  $T_{\text{plate}} = 43.7^\circ \text{C}$ . Once the four linear fits are computed for  $p = (H, V)$ , and  $ch = (1, 2)$ , the associated 3<sup>rd</sup> data pairs ( $T_{100K}, U_{100K}^{p,ch}$ ) (green in **FIGURE 3**) are computed.

This procedure applied to a large number of sky measurements performed at  $23^\circ \text{C} \lesssim T_{\text{plate}} \lesssim 45^\circ \text{C}$  yields  $U_{100K}^{p,ch}(T_{\text{plate}})$  as a function of  $T_{\text{plate}}$  as shown in **FIGURE 4**. These experimentally derived relations  $U_{100K}^{p,ch}(T_{\text{plate}})$  are approximated by four second-order polynomial models:

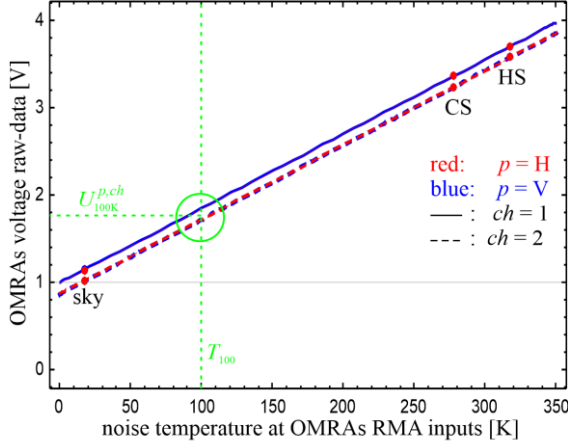


**FIGURE 3.** The OMRA's temperature-voltage domain. Points show data pairs  $(T_{\text{RMA,sky}}^p, U_{\text{sky}}^{p,ch})$ ,  $(T_{\text{CS}}, U_{\text{CS}}^{ch})$ ,  $(T_{\text{HS}}, U_{\text{HS}}^{ch})$  measured simultaneously at  $T_{\text{plate}} = 43.7^\circ\text{C}$  and  $T_{\text{air}} = 16.7^\circ\text{C}$ . Each of the four lines is a linear fit to these three data pairs.

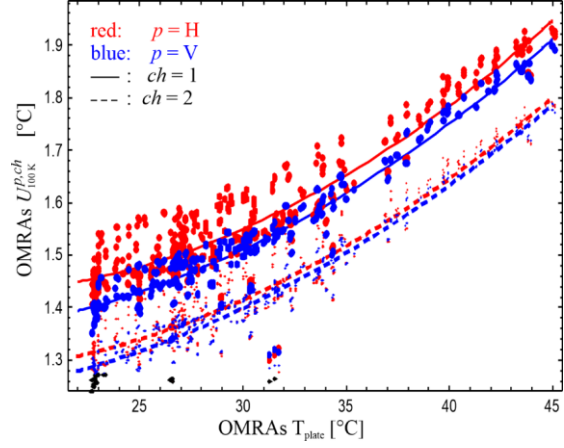


**FIGURE 4.** Dependency of OMRA's voltages  $U_{100\text{K}}^{p,ch}(T_{\text{plate}})$  on the plate temperature  $T_{\text{plate}}$ . Measured data pairs  $(T_{\text{RMA,sky}}^p, U_{\text{sky}}^{p,ch}(T_{\text{plate}}))$  are shown as points, lines represent the second-order polynomial models given by equations (4a-4d).

$$U_{100\text{K}}^{\text{H},1}(T_{\text{plate}}) = 1.50322 - 0.0143077 \cdot T_{\text{plate}} + 0.000536833 \cdot T_{\text{plate}}^2 \quad (4a)$$

$$U_{100\text{K}}^{\text{H},2}(T_{\text{plate}}) = 1.30040 - 0.01012810 \cdot T_{\text{plate}} + 0.000473613 \cdot T_{\text{plate}}^2 \quad (4b)$$

$$U_{100\text{K}}^{\text{V},1}(T_{\text{plate}}) = 1.37795 - 0.00979533 \cdot T_{\text{plate}} + 0.000478126 \cdot T_{\text{plate}}^2 \quad (4c)$$

$$U_{100\text{K}}^{\text{V},2}(T_{\text{plate}}) = 1.22688 - 0.00716161 \cdot T_{\text{plate}} + 0.000433903 \cdot T_{\text{plate}}^2 \quad (4d)$$

### 3.1.2. Approach to achieve calibrated $T_{\text{BL}}^p$

Footprint brightness temperatures  $T_{\text{BL}}^{p,ch}$  at  $p = (\text{H}, \text{V})$  and  $ch = (1, 2)$  are computed from the three reference calibration points  $(T_{\text{HS}}, U_{\text{HS}}^{ch})$ ,  $(T_{\text{CS}}, U_{\text{CS}}^{ch})$ , and  $(T_{100\text{K}}, U_{100\text{K}}^{p,ch})$  where  $U_{100\text{K}}^{p,ch}(T_{\text{plate}})$  is given by equations (4a) – (4d). Thereto, the three known calibration points in the temperature-voltage domain are first fitted with linear models (including the fit parameters  $a = T_{\text{RMA},0}^{p,ch}$  and  $b = dT_{\text{RMA}}^{p,ch}/dU$ ) to compute the noise temperature  $T_{\text{RMA}}^{p,ch}$  at the RMA inputs associated with the voltage  $U^{p,ch}$  measured by OMRA pointing toward a footprint:

$$T_{\text{RMA}}^{p,ch} = a + b \cdot U^{p,ch} \quad (5)$$

Finally, for each polarization  $p = (\text{H}, \text{V})$  and frequency channel  $ch = (1, 2)$  brightness temperature  $T_{\text{BL}}^{p,ch}$  is computed by correcting the respective  $T_{\text{RMA}}^{p,ch}$  for the Transmission Losses (TL) between the antenna and the RMA input-ports:

$$T_{\text{BL}}^{p,ch} = \frac{T_{\text{RMA}}^{p,ch} - T_{\text{air}} \cdot (1 - t_{\text{TL}}^p)}{t_{\text{TL}}^p} \quad (6)$$

L-band brightness temperatures  $T_{\text{BL}}^p$  ultimately used for scientific analysis are computed from RFI-free  $T_{\text{BL}}^{p,ch}$  as:

$$T_{BL}^p = (T_B^{p,1} + T_B^{p,2})/2 \quad (7)$$

### 3.1.3. RFI filtering

The same Radio Frequency Interference (RFI) flags are applied to both, OMRA footprint- and sky measurements. An RFI flag is raised if one of the following criteria is fulfilled:

- 1) The difference between the mean of measured brightness temperatures of one sample (consisting of 2400 single measurements performed at 800 Hz) and the mean of the Gaussian fit to the PDF of the measured sample exceeds 2 K. This approach is described in detail in Section 4.2 in [1] and quantifies the amount of non-thermal emission contained in a measurement sample.
- 2) The difference between  $T_{BL}^{p,ch}$  measured at  $ch = 1$  and  $ch = 2$  is larger than 4 K. This makes use of the two frequency channels  $ch = (1, 2)$  within the protected part (1.400 GHz – 1.427 GHz) of the microwave L-band (1 GHz – 2 GHz) measured by OMRA and it allows to detect out-of-band RFI because this kind of RFI is often frequency dependent.

$T_{BL}^{p,ch}$  being subject to the mentioned RFI criteria is excluded from the dataset provided to ESA and shown in D2/D2a.

## 3.2. Approach to achieve Calibrated X-band Brightness Temperatures

The X-band radiometer MIRA [4] is assembled at the aperture of the L-band radiometer's horn antenna as is shown with Figure 1 in D1 [2]. Passive X-band brightness temperatures  $T_{BX}^V$  at vertical polarization are collected for the same azimuth- and elevation angles  $\varphi = (75^\circ, 125^\circ, 180^\circ)$  and  $\theta = (30^\circ, 35^\circ, 40^\circ, 45^\circ, 50^\circ, 55^\circ, 60^\circ)$ , respectively.

MIRA's raw voltage data  $U_{MIRA}$ , measured over footprints, are used to derive X-band brightness temperatures  $T_{BX}^V$  of footprints via:

$$T_{BX}^V = A + B \cdot U_{MIRA} \quad (8)$$

The offset  $A$  and the gradient  $B$  are computed from two reference data pairs  $(U_{sky}, T_{sky})$  and  $(U_{abs}, T_{abs})$ . The latter corresponds to the MIRA output voltage  $U_{abs}$  when measuring on an external microwave absorber (abs) of temperature  $T_{ref}$ , while  $(U_{sky}, T_{sky})$  represents MIRA output voltage  $U_{sky}$  measured toward the sky of X-band brightness temperature  $T_{sky} \approx 10K$ .

$$A = (T_{abs} \cdot U_{sky} - T_{sky} \cdot U_{abs}) / (U_{sky} - U_{abs}) \quad (9a)$$

$$B = (T_{sky} - T_{abs}) / (U_{sky} - U_{abs}) \quad (9b)$$

The value used for  $U_{sky} \cong -2.872V$  was determined from the collectively of all the sky measurements available from the time-period when MIRA was functioning (15 October 2019

– 21 November 2019). The reference voltage  $U_{\text{abs}}$  and associated  $T_{\text{abs}}$  were considered as  $U_{\text{abs}} = 1\text{V}$  and  $T_{\text{abs}} = 273.15\text{K}$ .

We acknowledge that the second pair of reference data ( $U_{\text{abs}}, T_{\text{abs}}$ ) used with equations (8) and (9a,b) does not yield the most accurately calibrated X-band brightness temperatures  $T_{\text{BX}}^{\text{V}}$  because measurement of ( $U_{\text{abs}}, T_{\text{abs}}$ ) was performed several years ago. Therefore, the ageing effects could have caused a change of radiometer performance and thus resulting in less accurate calibration results. An attempt will be made to fix MIRA and measure ( $U_{\text{ref}}, T_{\text{ref}}$ ) to achieve more reliably calibrated  $T_{\text{BX}}^{\text{V}}$ . However, for now the X-band brightness temperatures  $T_{\text{BX}}^{\text{V}}$  provided with this deliverable are considered as scientifically useful. This is because passive X-band observations are only used to assess snow states in a qualitative manner, rather than using  $T_{\text{BX}}^{\text{V}}$  in a retrieval approach based on the inversion of a physical microwave emission model.

### 3.3. Approach to achieve InfraRed Temperatures

As is the case with MIRA [4], the thermal InfraRed (IR) radiometer Everest Interscience 4000.4ZH is attached to OMRA's antenna aperture to measure IR surface-temperatures  $T_{\text{IR}}$  synchronous and collocated with L- and X-band brightness temperatures at azimuth- and elevation angles  $\varphi = (75^\circ, 125^\circ, 180^\circ)$  and  $\theta = (30^\circ, 35^\circ, 40^\circ, 45^\circ, 50^\circ, 55^\circ, 60^\circ)$ , respectively.

The IR radiometer's raw voltage data  $U_{\text{IR}}$  measured over footprints are used to derive  $T_{\text{IR}}$  via:

$$T_{\text{IR}} = U_{\text{IR}}/G \quad (10)$$

According to the IR radiometer's spec-sheet the gain is  $G = 10\text{mV} \cdot ^\circ\text{C}^{-1}$  and the voltage output  $U_{\text{IR}}$  is zero for a measurement on a blackbody target of  $0^\circ\text{C}$ .

### 3.4. L- & X-band Brightness Temperatures and InfraRed & Air Temperatures

**FIGURE 5**, **FIGURE 6**, and **FIGURE 7** show the calibrated L- and X-band brightness temperatures measured at azimuth directions  $\varphi = 75^\circ$  (mainly charcoal-sand area),  $\varphi = 125^\circ$  (natural ground), and  $\varphi = 180^\circ$  (large reflector-area), respectively. The red crosses in panels (a–c) refer to the corrupted data in the beginning of the campaign most probably caused by a temporal instrument or data logging system failure. The time series of air temperature  $T_{\text{air}}$ , precipitation  $P$ , snow height  $h_{\text{S}}$ ,  $SWE$ , and radiation intensity-ratios—all measured by the on-site AWS—are the same for the three figures. It is important to highlight that the L-band brightness temperatures measured at  $\varphi = 180^\circ$  are not corrected for the partial contribution of the surrounding natural ground. The method for this correction and its result are presented in Section 3.5.

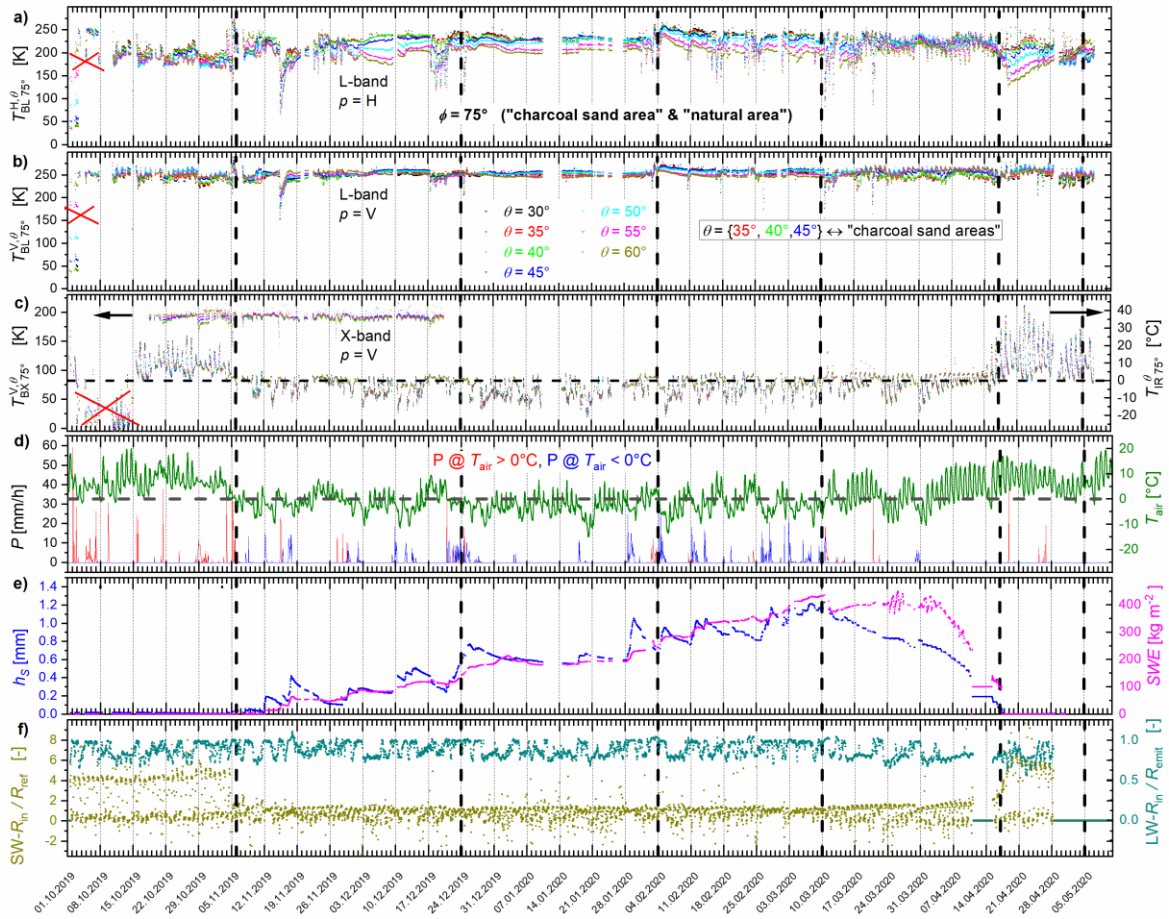


**FIGURE 5.** L-band brightness temperatures  $T_{BL,\phi}^{p,\theta}$  measured at the azimuth angle  $\phi = 75^\circ$  and nadir angles  $\theta = (30^\circ, 35^\circ, 40^\circ, 45^\circ, 50^\circ, 55^\circ, 60^\circ)$  at **a)** horizontal ( $p = H$ ) and **b)** vertical ( $p = V$ ) polarization; **c)** corresponding X-band brightness temperatures  $T_{BX,\phi}^{V,\theta}$  at  $p = V$  (left axes) and IR temperatures  $T_{IR,\phi}^{\theta}$  (right axes); **d)** precipitation (left axes)  $P$  and air temperature (right axes)  $T_{air}$ .

A closer look at the time-series of all presented data, especially in terms of snow cover state, implicates six distinctly different periods during the Winter 2019/2020 campaign. Vertical dashed lines in **FIGURE 5**, **FIGURE 6**, and **FIGURE 7** help distinguish these periods. In the following, the main features of each period, characterized by radiometry at different frequencies, are described:

### 1. Snow-Free period (1.10.2019 – 6.11.2019)

- 1.1. As a result of direct exposure of the ground to sunlight and air, there exist daily  $T_{BL,\phi}^{p,\theta}$  fluctuations during snow-free period for  $\phi = (75^\circ, 125^\circ)$  at all nadir elevation angles  $\theta$  and both polarizations  $p = (H, V)$ .
- 1.2. Such daily fluctuations are absent over the large reflector area. However,  $T_{BL,125^\circ}^{p,\theta}$  does respond to rain fall due to increased moisture of short grass ( $\lesssim 2$  cm).

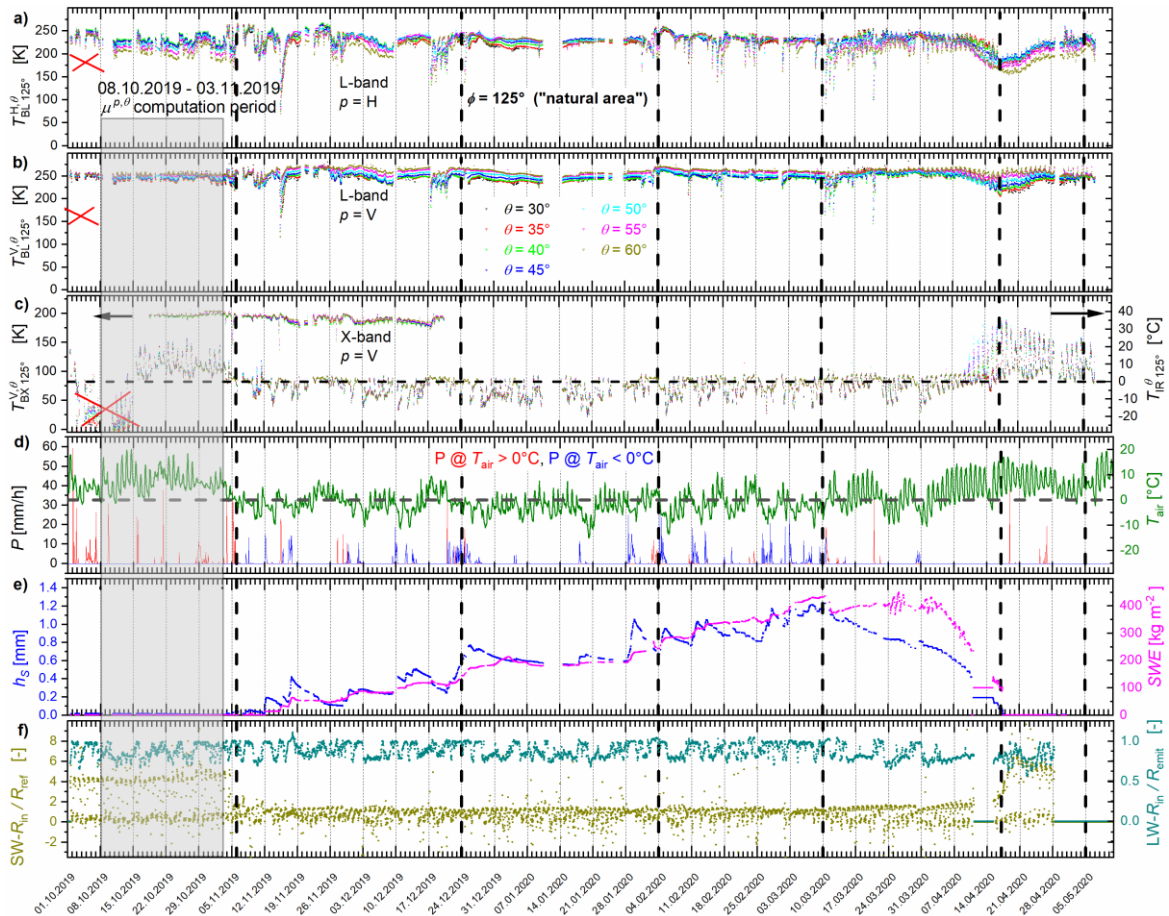


**FIGURE 6.** Same as **FIGURE 5** but for  $\phi = 125^\circ$ . The grey shaded area marks the time-period used to compute weighting factors  $\mu^{p,\theta}$  used to compute L-band  $T_{BL,R}^{p,\theta}$  originating exclusively from the “large Reflector area” (Section 3.5.).

1.3. Infrared  $T_{IR,\phi}^\theta$  and air  $T_{air}$  temperatures are both above freezing point with significant daily fluctuations of up to 15° C. Already with the appearance of a very thin layer of snow (<10 cm), the infrared temperatures can drop below 0 °C.

## 2. Early-Winter period (6.11.2019 – 24.12.2019)

2.1.  $T_{BL,75}^{H,\theta}$  and  $T_{BL,125}^{H,\theta}$  clearly respond to the onset of snow in form of a roughly 25-Kelvin jump in brightness temperature on 12 November 2019. This response at  $p = V$  is minimal.

2.2. There is virtually no response of  $T_{BL,180}^{p,\theta}$  (reflector area) to the onset of the snow-cover; because as theoretically expected, dry snow does not have self-emission at L-band.

2.3. Irregular (as opposed to daily) fluctuations of  $T_{BL,75}^{p,\theta}$  and  $T_{BL,125}^{p,\theta}$  (especially at  $p = H$ ) continue until about 31 December 2019 due to wet or dry snow precipitation occasionally accompanied by  $T_{air} > 0^\circ \text{C}$ . These fluctuations are caused by a combined effect of

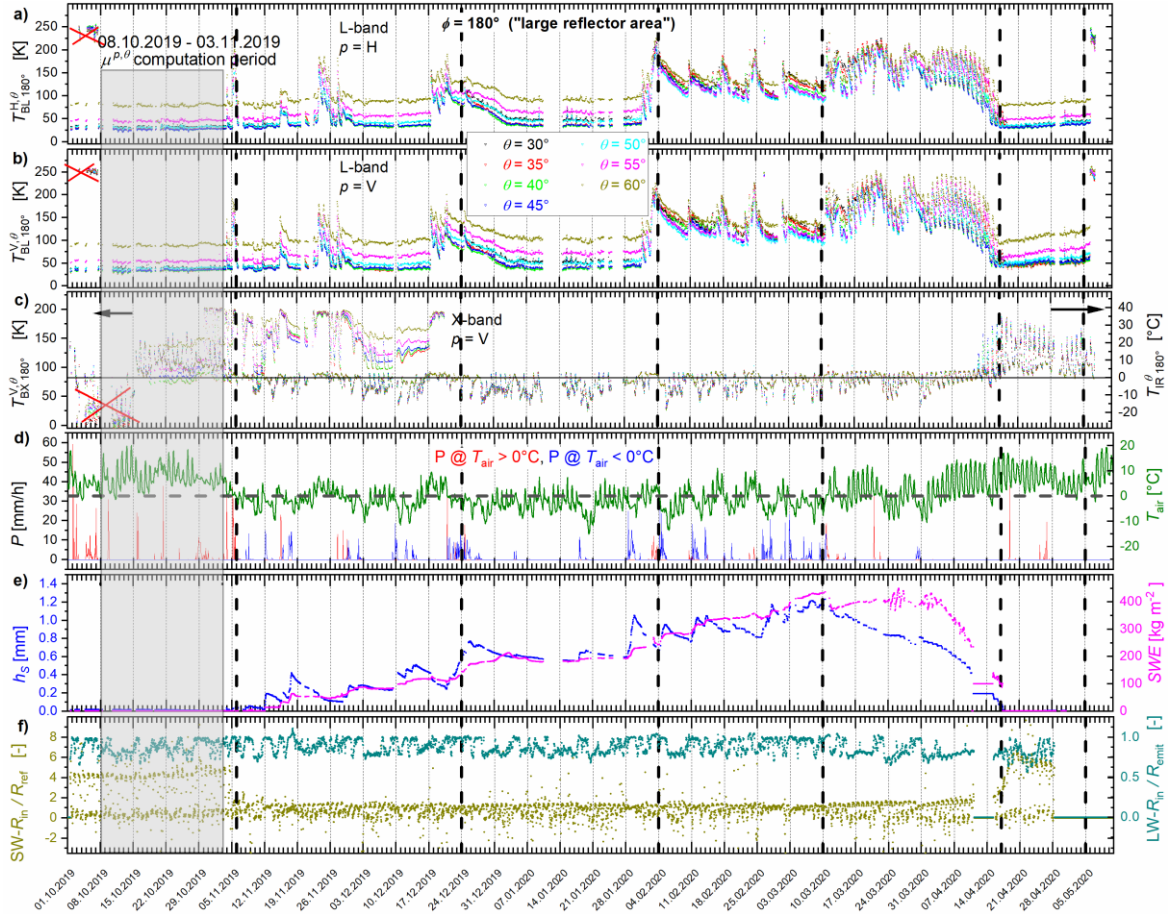


**FIGURE 7.** Same as **FIGURE 5** but for  $\phi = 180^\circ$ . The grey shaded area marks the time-period used to compute weighting factors  $\mu^{p,\theta}$  used to compute L-band  $T_{BL,R}^{p,\theta}$  originating exclusively from the “large Reflector area” (Section 3.5. ).

changing snow density (due to metamorphosis and precipitation) and snow wetness (due to air temperature and wet snowfall).

2.4.  $T_{BL,180}^{p,\theta}$  responds to precipitation at positive temperatures due to increased snow wetness.

### 3. Cold-Winter period (24.12.2019 – 4.2.2020)

3.1. In this period air temperature is generally below  $0^\circ\text{C}$  only with occasional short peaks of positive temperatures during the day.

3.2. The snowpack is dry, and precipitation is in form of dry snow. Therefore,  $T_{BL,\phi}^{p,\theta}$  at both polarizations and the three areas is almost steady with no significant variation.

3.3. Infrared temperatures, which are sensitive to the surface of the snow, remain below  $0^\circ\text{C}$  with daily variations caused by  $T_{\text{air}}$  changes.

### 4. Early-Spring period (4.2.2020 – 10.3.2020)

- 4.1. Towards the end of the Cold-Winter period, duration of daily positive air temperatures increases, resultantly the ice latent heat of the snowpack is gradually reached. This ends in appearance of small amounts of liquid water from approximately 1 February 2020. During the early-spring, air temperature follows a somewhat weekly fluctuation trend causing weekly fluctuations in  $T_{BL,180^\circ}^{p,\theta}$ .
- 4.2. Similar fluctuations exist for  $T_{BL,75^\circ}^{p,\theta}$  and  $T_{BL,125^\circ}^{p,\theta}$  (more severely for  $p = H$ ). However, because of the underlying ground's emission contribution, these fluctuations are not as distinguished as for  $T_{BL,180^\circ}^{p,\theta}$  measured over the large reflector area.
- 4.3. During this period  $T_{BL,180^\circ}^{p,\theta}$  never drops to its values observed during the Cold-Winter period indicating that the snowpack was constantly moist during this time.
- 4.4. Until about 10 March 2020, snow height  $h_S$  (**FIGURE 5. e**) is either increasing or steady. However, after this time, the snowpack starts to melt and thus the snow height shrinks.

### 5. Melting period (10.3.2020 – 17.4.2020)

- 5.1. Steadily decreasing snow height in **FIGURE 5. e**) indicates constant snow melt until complete melt by approximately 17 April 2020. During this time snowpack is constantly wet with snow wetness changing daily following the  $T_{air}$  fluctuations.  $T_{BL,180^\circ}^{p,\theta}$  shows the same daily pattern with as much as 100 K variations.
- 5.2.  $T_{BL,75^\circ}^{p,\theta}$  and  $T_{BL,125^\circ}^{p,\theta}$  at both polarizations also show daily variations only with limited amplitude of  $\sim 40$  K and  $< 10$  K for  $p = H$  and  $V$  polarizations, respectively. It is reiterated that generally,  $T_{BL,\varphi}^{V,\theta}$  measurements at vertical polarization are less influenced by the snowpack properties ergo their lower fluctuation amplitude.

### 6. After-Melt period (17.4.2020 – 5.5.2020)

- 6.1. The effect of complete melt of the snowpack immediately shows itself in rapid decrease of  $T_{BL,75^\circ}^{p,\theta}$  and  $T_{BL,125^\circ}^{p,\theta}$  by about 50 K. This response is best visible for measurements at horizontal polarization over the natural ground ( $T_{BL,125^\circ}^{p,\theta}$  at all elevation angles and  $T_{BL,75^\circ}^{p,\theta}$  at  $\theta = (55^\circ, 60^\circ)$ ).
- 6.2. For the large reflector area measurements,  $T_{BL,180^\circ}^{p,\theta}$  at both polarizations quickly drops to values observed during the Snow-Free period. However,  $T_{BL,180^\circ}^{V,\theta}$  (exclusively at  $p = V$ ) gradually increases by  $\sim 25$  K over two weeks after snow melt-down. This is due to the vertically oriented weed growing through the reflector mesh. Therefore, its emission is more pronounced at vertical polarization than at horizontal polarization.
- 6.3. The air temperature during this period stays entirely above  $0^\circ\text{C}$  and with no snow cover acting as a thermal blanket, the infrared temperatures  $T_{IR,\varphi}^\theta$  rise above  $0^\circ\text{C}$ .

### 3.5. Segregated L-band Brightness Temperatures of “Large Reflector Area”

Segregated L-band brightness temperatures  $T_{BL,R}^{p,\theta}$  originating exclusively from the “large Reflector area” are proven as very useful to quantify the thermal emission of solely the snowpack’s thermal emission [5]. This instance finds its application, for example, in the quantification of snow liquid water content  $W_S$  retrievable from  $T_{BL,R}^{p,\theta}$  and the respective snow liquid water column estimated as  $WC_S = W_S \cdot h_S$  for a homogeneous snowpack of height  $h_S$  (Section 3.6.1. ). Accordingly, L-band  $T_{BL,R}^{p,\theta}$  provide important reference information on the wetness of the snowpack, which is crucial for the interpretation of other types of close-range microwave- and IR measurements performed at the Davos-Laret site. Because of this central scientific role, in D2/D2a we include L-band  $T_{BL,R}^{p,\theta}$  and thereon based estimates of  $WC_S$  (Section 3.6.2). Of course, this requires the subsequent description of the approach used to achieve  $T_{BL,R}^{p,\theta}$ : Even when pointing OMRA exactly along the central line of the “large reflector area” at the azimuth angle  $\varphi = 180^\circ$ , the respective brightness temperatures  $T_{BL,180^\circ}^{p,\theta}$  include a significant contribution from radiance emanating from the “natural area” surrounding the “large reflector area”. This is a consequence of the finite antenna field-of-view as explained in D1 [2]. Assuming low spatial heterogeneity of natural areas outside the reflector, radiance from just outside the reflector area can be approximated by OMRA brightness temperature  $T_{BL,125^\circ}^{p,\theta}$  over the “natural area” measured at the azimuth angle  $\varphi = 125^\circ$ . This means that  $T_{BL,180^\circ}^{p,\theta}$  can be expressed as a weighted sum of quasi time-synchronous  $T_{BL,R}^{p,\theta}$  and  $T_{BL,125^\circ}^{p,\theta}$ :

$$T_{BL,180^\circ}^{p,\theta} = \mu^{p,\theta} \cdot T_{BL,R}^{p,\theta} + (1 - \mu^{p,\theta}) \cdot T_{BL,125^\circ}^{p,\theta} \quad (11)$$

Conversely, solving equation (11) for  $T_{BL,R}^{p,\theta}$  yields brightness temperatures originating exclusively from the “large Reflector area” expressed by quasi-simultaneous measurements  $T_{BL,180^\circ}^{p,\theta}$  and  $T_{BL,125^\circ}^{p,\theta}$ :

$$T_{BL,R}^{p,\theta} = [T_{BL,180^\circ}^{p,\theta} - (1 - \mu^{p,\theta}) \cdot T_{BL,125^\circ}^{p,\theta}] / \mu^{p,\theta} \quad (12)$$

The crucial point with this simple approach lies in the knowledge of the weighting factors  $\mu^{p,\theta}$  for different observation nadir angles  $\theta = (30^\circ, 35^\circ, 40^\circ, 45^\circ, 50^\circ, 55^\circ, 60^\circ)$  and polarizations  $p = (H, V)$ . Theoretically,  $\mu^{p,\theta}$  can be computed as the convolution of the antenna sensitivity pattern and the geometry of the “large reflector area” seen from the position and orientation of OMRA’s Picket horn-antenna. Such a theoretical estimation has been done prior the installation of the experimental setup to define the most appropriate layout of the “large reflector area”, which led to its trapezoid shape to achieve similar  $\mu^{p,\theta}$  for different  $\theta$ .

However, we determine  $\mu^{p,\theta}$  from measured  $T_{BL,180^\circ}^{p,\theta}$  and  $T_{BL,125^\circ}^{p,\theta}$  as the corresponding experimental approach is more representative for the actual setup. The experimental approach does not rely on accurate knowledge of the antenna sensitivity pattern and it is not subject to errors introduced via uncertainties in the actual geometry of the reflector and its position relative

to the radiometer antenna. We use calibrated and RFI filtered  $T_{BL,125^\circ}^{p,\theta}$  and  $T_{BL,180^\circ}^{p,\theta}$  measured during snow-free conditions at the beginning of the campaign corresponding to the time-period 8 October 2019 – 3 November 2019 marked in **FIGURE 6** and in **FIGURE 7**.

Once the most adequate time-series of  $T_{BL,125^\circ}^{p,\theta}$  and  $T_{BL,180^\circ}^{p,\theta}$  are selected, the following Cost Function is minimized to compute  $\mu^{p,\theta}$  for each  $\theta = (30^\circ, 35^\circ, 40^\circ, 45^\circ, 50^\circ, 55^\circ, 60^\circ)$  and  $p = (H, V)$ :

$$CF(\mu^{p,\theta}) = \sum (T_{BL,180^\circ}^{p,\theta} - [\mu^{p,\theta} \cdot T_{sky}^\theta + (1 - \mu^{p,\theta}) \cdot T_{BL,125^\circ}^{p,\theta}])^2 \quad (13)$$

Summation runs over all the brightness temperatures  $T_{BL,125^\circ}^{p,\theta}$  and  $T_{BL,180^\circ}^{p,\theta}$  measured during the  $\mu^{p,\theta}$ -computation period marked in grey in **FIGURE 6** and in **FIGURE 7**.

**FIGURE 8** shows resulting  $CF(\mu^{p,\theta})$  evaluated for the examples of  $\theta = (30^\circ, 45^\circ, 60^\circ)$ . The term  $[\mu^{p,\theta} \cdot T_{sky}^\theta + (1 - \mu^{p,\theta}) \cdot T_{BL,125^\circ}^{p,\theta}]$  in equation (13) represents theoretically expected brightness temperature for measurements along the azimuth angle  $\varphi = 180^\circ$  pointing along the central line of the “large reflector area”. This term corresponds with equation (11) considering the replacement  $T_{BL,R}^{p,\theta} \rightarrow T_{sky}^\theta$  expressing the assumption of reflector reflectivity equal to one and thus full reflection of downwelling sky radiance  $T_{sky}^\theta$  by the “large reflector area”. This assumption may not be always true; however, deviations from this ideal case are at least partially included in the final  $\mu^{p,\theta}$  which is another advantage of its experimental determination.

$CF(\mu^{p,\theta})$  defined by equation (13) expresses the sum of squared differences between measured and simulated brightness temperatures along the azimuth angle  $\varphi = 180^\circ$ . This implies that the specific  $\mu^{p,\theta}$  yielding the minimum of  $CF(\mu^{p,\theta})$  represents the value of the retrieved  $\mu^{p,\theta}$  used later to compute  $T_{BL,R}^{p,\theta}$  from measurements  $T_{BL,180^\circ}^{p,\theta}$  and  $T_{BL,125^\circ}^{p,\theta}$  using equation (12).

**FIGURE 9** shows the final  $\mu^{p,\theta}$ -values achieved for  $\theta = (30^\circ, 35^\circ, 40^\circ, 45^\circ, 50^\circ, 55^\circ, 60^\circ)$  and polarization  $p = (H, V)$ . These

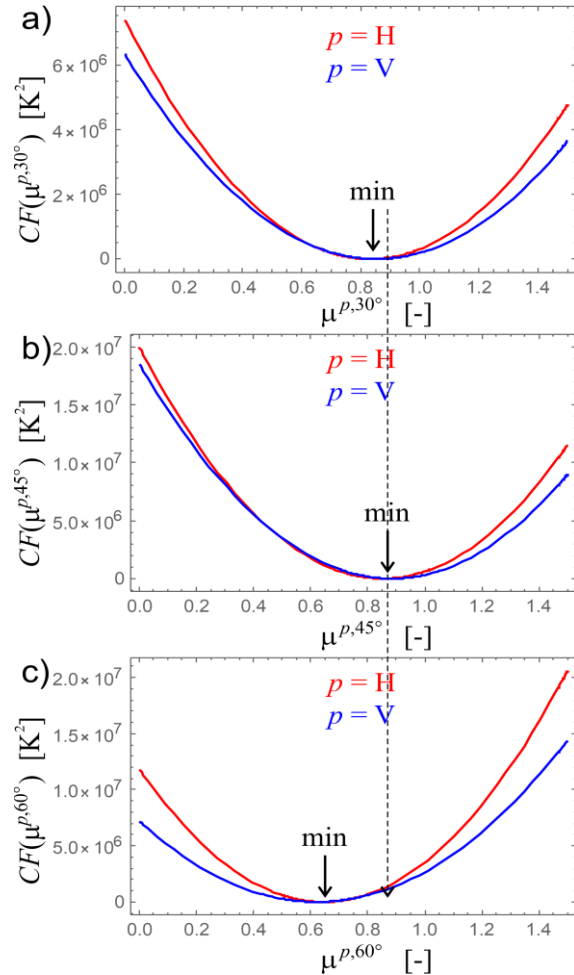


**FIGURE 8.** Cost Functions  $CF(\mu^{p,\theta})$  defined by equation 13 for  $p = H$  (red) and  $p = V$  (blue) for **a)**  $\theta = 30^\circ$ ; **b)**  $\theta = 45^\circ$ , **c)**  $\theta = 60^\circ$ .

$\mu^{p,\theta}$ -values are considered as constants in time and, as mentioned earlier, used to compute time-series of segregated  $T_{BL,R}^{p,\theta}$  of solely the “large reflector area” based on  $T_{BL,125^\circ}^{p,\theta}$  and  $T_{BL,180^\circ}^{p,\theta}$  measured toward “natural ground” and “large reflector area”, respectively.

The resulting time-series of  $T_{BL,R}^{p,\theta}$  for the entire winter 2019/2020 are shown in panels a) and b) of **FIGURE 11** for  $p = H$ , and  $p = V$ , respectively. **FIGURE 11 c)** shows precipitation  $P$  (left axes) and air temperature  $T_{air}$  (right axes). **FIGURE 11 d)** shows snow height  $h_S$  (left axes) and SWE (right axes).

Even though D2/D2a does not present detailed interpretation of the measurement data it is still worthwhile to mention some points:

- 1) During snow-free periods at the beginning and at the end of the winter,  $T_{BL,R}^{p,\theta}$  are low and close to  $T_{BL,R}^{p,\theta} = T_{sky}^\theta \simeq 3K - 5K$  which is the theoretically expected range for  $\theta = 30^\circ - 60^\circ$ . It can be seen that  $T_{BL,R}^{p,\theta}$ -values after total snow-clearance (at around 18 April 2020) drop to very similar values as during the snow-free period (8 October 2019 – 3 November 2019) selected for the  $\mu^{p,\theta}$ -computation. This corroborates that assuming a constant  $\mu^{p,\theta}$  for a given  $\theta$  and  $p$  for the entire winter campaign is a valid assumption.
- 2) The temporal pattern of  $T_{BL,R}^{p,\theta}$  suggests different characteristic states of the snowpack. This is predominantly a result of changing snow-wetness, which distinctly impacts microwave absorption/emission. For instance, the very low  $T_{BL,R}^{p,\theta}$  during 1. – 30. January 2020 suggests that the snowpack was nearly transparent at L-band and therefore rather dry during this mid-winter period. It is also apparent that during the late winter period (beginning with ~10 March 2020),  $T_{BL,R}^{p,\theta}$  follows diurnal cycles much more than during earlier winter periods. However, a more detailed assessment of the valuable information on snow-wetness contained in  $T_{BL,R}^{p,\theta}$  will be provided in Section 3.6.2. where we show Snow liquid Water Column  $WC_S$  retrieved from  $T_{BL,R}^{p,\theta}$ .
- 3) The subsequent Section 3.6.1. outlines the approach used to retrieve  $WC_S$  from  $T_{BL,R}^{p,\theta}$  and Section 3.6.2. provides and discusses resulting time-series of  $WC_S$ .

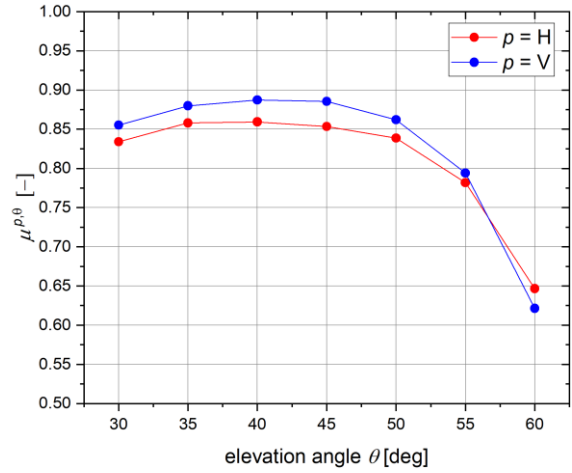


**FIGURE 9.**  $\mu^{p,\theta}$ -factors derived from  $T_{BL,180^\circ}^{p,\theta}$  and  $T_{BL,125^\circ}^{p,\theta}$  measured during the  $\mu^{p,\theta}$ -computation period marked in **FIGURE 6** and **FIGURE 7**.

### 3.6. Snow liquid Water Column

#### 3.6.1. Retrieval Approach

The L-band Specific Microwave Emission Model for Layered Snowpack (LS-MEMLS) [6] in its single layer version is used as the forward operator to retrieve volumetric snow liquid water content  $W_S$ . Accordingly,  $W_S$  is interpreted as representative for the average liquid water content of the snowpack of height  $h_S$ , which allows the estimation of  $WC_S$  as:

$$WC_S = h_S \cdot W_S \quad (11)$$

FIGURE 10 illustrated the setup of the single-layer LS-MEMLS used to retrieve  $W_S$  from multi-angle  $T_{BL,R}^{p,\theta}$ . Here, we skip detailed description related to LS-MEMLS, because its formulation can be found in literature, such as in [1, 5, 7-9].

The actual retrieval of  $W_S$  is achieved by minimizing the Cost Function ( $CF$ ) expressing the sum of squared differences between simulated  $T_{BL,R,sim}^{p,\theta}$  and measured  $T_{BL,R}^{p,\theta}$ :

$$CF(W_S) = \sum_{p,\theta} (T_{BL,R,sim}^{p,\theta} - T_{BL,R}^{p,\theta})^2 \quad (14)$$

Depending on the selected Retrieval Mode  $RM = ("HV", "H", "V")$  summation runs over both polarizations  $p = (H, V)$ ,  $p = H$ , or  $p = V$ , respectively. Furthermore, summation in equation (14) runs over the nadir angles  $\theta$  of undistorted  $T_{BL,R}^{p,\theta}$  included in an elevation scan. We required at least 5 sane tuples  $(T_{BL,R}^{H,\theta}, T_{BL,R}^{V,\theta})$  out of the 7 tuples measured for elevation angles  $\theta = (30^\circ, 35^\circ, 40^\circ, 45^\circ, 50^\circ, 55^\circ, 60^\circ)$  to perform a multi-angle retrieval of  $W_S$ .

The information on snow mass-density  $\rho_S$  necessary to simulate  $T_{BL,R,sim}^{p,\theta}$  is computed from  $SWE$  and  $h_S$  measured by the AWS at the Davos-Laret test site:

$$\rho_S = SWE/h_S \quad (15)$$

Measured  $T_{BL,R}^{p,\theta}$  which are smaller than  $T_{sky}^\theta$  simulated for the respective  $\theta$  are replaced by the minimum physically meaningful value  $T_{BL,R}^{p,\theta} = T_{sky}^\theta$ . However, as can be seen from FIGURE 11 the number of unphysical  $T_{BL,R}^{p,\theta} < T_{sky}^\theta$  is very limited and only occurs during snow-free periods where  $W_S$  is inherently zero. The third model parameter (beside  $W_S$  and  $\rho_S$ ) used to simulate  $T_{BL,R,sim}^{p,\theta}$  is the temperature  $T_S$  of the snowpack. It is considered as the snow surface

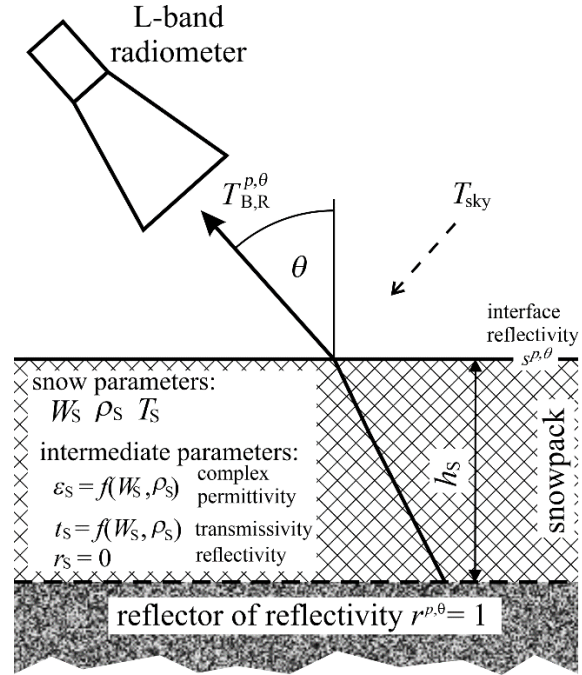
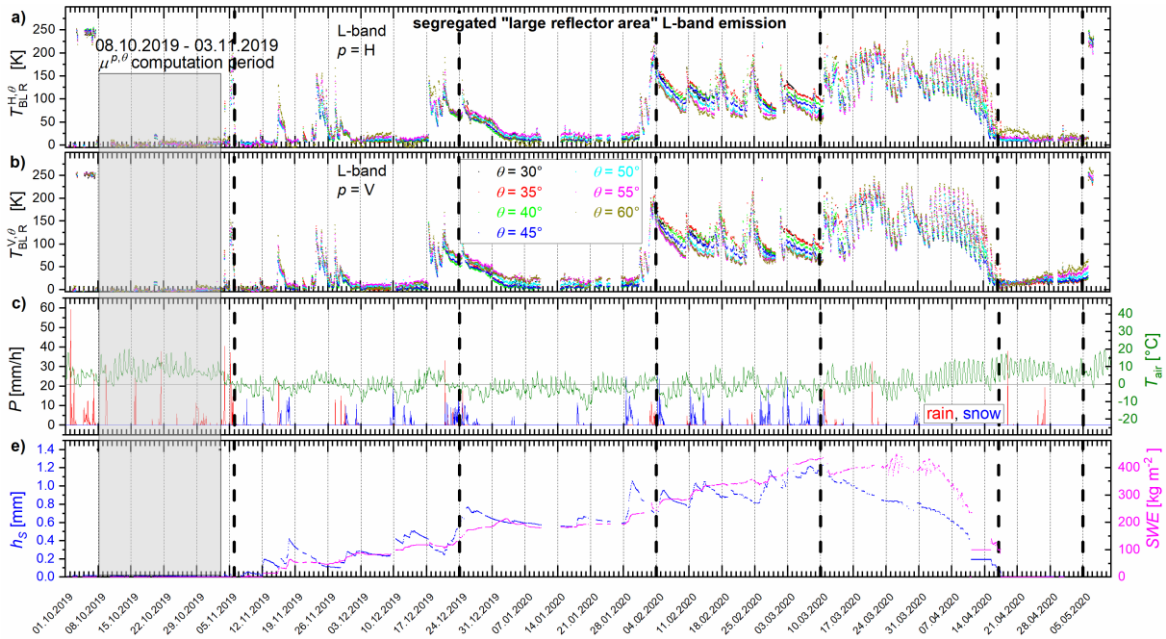


FIGURE 10. Setup of the single-layer LS-MEMLS used to retrieve  $W_S$  from multi-angle  $T_{BL,R}^{p,\theta}$ .



**FIGURE 11.** Brightness temperatures  $T_{BL,R}^{p,\theta}$  for  $\theta = (30^\circ, 35^\circ, 40^\circ, 45^\circ, 50^\circ, 55^\circ, 60^\circ)$  of “large Reflector area” at **a)** horizontal polarization, and **b)** vertical polarization; **c)** precipitation  $P$  and air temperature  $T_{air}$ ; **d)** snow height  $h_s$  and  $SWE$ .

temperature measured by the IR sensor operated at the AWS. The thereby introduced error in  $T_{BL,R,sim}^{p,\theta}$  is acceptable. It vanishes totally if the snowpack is dry because in this case the snowpack’s own emission is nearly zero. If the snowpack contains small amounts of liquid water, its temperature is  $T_S \leq 0^\circ C$  close to the freezing point.

### 3.6.2. Retrieved $WC_S$

**FIGURE 12** shows time-series of snow liquid water column  $WC_S$  retrieved from multi-angle  $T_{BL,R}^{p,\theta}$  accompanied by in-situ measured precipitation  $P$ , air temperature  $T_{air}$ , snow height  $h_S$ ,  $SWE$ , and mean snow density  $\rho_S$  in three separate panels. All the in-situ parameters are measured by the AWS except for  $\rho_S$  which is estimated as  $\rho_S = SWE/h_S$ .

$WC_S$  shown in **FIGURE 12 a)** is derived from the snowpack’s volumetric liquid water content  $W_S$  retrieved from measured  $T_{BL,R}^{p,\theta}$  using the Retrieval Mode  $RM = “HV”$ .  $WC_S$  was also computed using  $RM = (“H”, “V”)$ . However, differences between  $WC_S$  achieved with different  $RM$ ’s are negligible and thus only  $WC_S$  achieved with dual polarization  $RM = “HV”$  is shown.

In analogy to the brief discussion on the temporal features seen in  $T_{BL,R}^{p,\theta}$  (**FIGURE 11**) the  $WC_S$  time-series shown in **FIGURE 12** reveal:

- 1)  $WC_S$  is close to zero during most times of the snow-free period at the beginning and at the end of Winter 2019/2020. The sole exception at around 6<sup>th</sup> November is associated with grass wetted by intense rain.

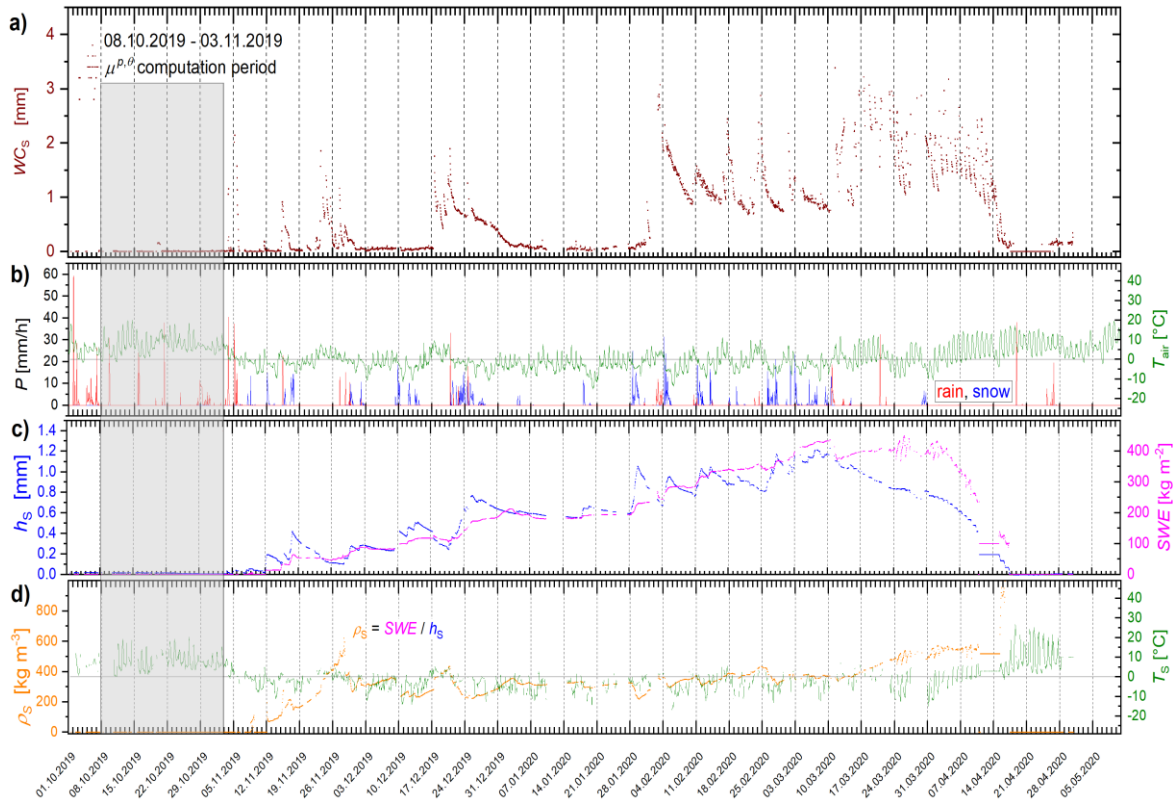


**FIGURE 12.** a) snow liquid water column  $WC_S$  estimated from the snowpack’s mean liquid water content  $W_S$  retrieved from measured  $T_{BL,R}^{p,\theta}$  shown in **FIGURE 5**; b) precipitation  $P$  and air temperature  $T_{air}$ ; c) snow height  $h_s$  and  $SWE$ ; d) mean mass-density  $\rho_s = SWE/h_s$  of the snowpack and snow surface temperature  $T_s$ .

- 2) Different wetness-states of the snowpack can be identified from the temporal pattern of  $WC_S$  time-series.  $WC_S$  are partially correlated with air temperature  $T_{air}$  fluctuations around and above the freezing point. For example, daily  $T_{air}$  fluctuations between 10 March - 14 April are correlated with  $WC_S$  such that with warming and cooling of air temperature, the snowpack liquid water column increases and decreases, respectively. Furthermore, snowpack liquid water column  $WC_S$  shows delayed increases when  $T_{air}$  rises above  $0^\circ\text{C}$ , and  $WC_S$  shows no response if  $T_{air}$  is not long enough above  $0^\circ\text{C}$  to overcome snow latent heat.
- 3) Rain and wet snow precipitation clearly increase  $WC_S$  as is shown with multiple examples in **FIGURE 12**, such as the period 4 February - 3 March.
- 4) Snow liquid-Water Column  $WC_S$  retrieved from  $T_{BL,R}^{p,\theta}$  is a derivate dataset which is valuable for the interpretation of other simultaneous close-range active and passive measurements. Therefore,  $WC_S$  shown in **FIGURE 12** is seen as a reference data-product for the interpretation of WBScat microwave backscatter as well as IR measurements.

## 4. IN-SITU MEASUREMENTS

### 4.1. Soil

A network of in-situ soil characterization sensors was deployed on three transects over the test site for regular automated measurements of soil state parameters. **FIGURE 1** shows these transects and the IDs of sensors deployed along each. A total of five 5TE fork sensors and 25 SMT-100 sensors were installed with the former measuring soil temperature  $T_G$ , volumetric water content  $WC$ , and electrical DC conductivity  $EC$ , and the latter measuring relative permittivity of soil  $\epsilon_G$  and temperature  $T_G$ .

Transect-1 sensors were deployed to measure the permittivity and temperature within the sand layer and the charcoal-mix layer, which together formed the “charcoal-sand area”. Therefore, as shown in **FIGURE 1**, five pairs of SMT-100 sensors were installed over Transect-1 to capture the spatial heterogeneities of the charcoal-sand area as well as soil parameters at different layers. Transect 2 was deployed for the measurement of  $\epsilon_G$  and  $T_G$  within the “natural ground” footprint areas observed by the radiometers. As shown in **FIGURE 1**, Transect 3 was deployed next to the WBScat tower along the azimuth direction  $\varphi = 0^\circ$  to best characterize the status of the natural ground area of WBScat scanning. It is noteworthy that unlike Transect 2

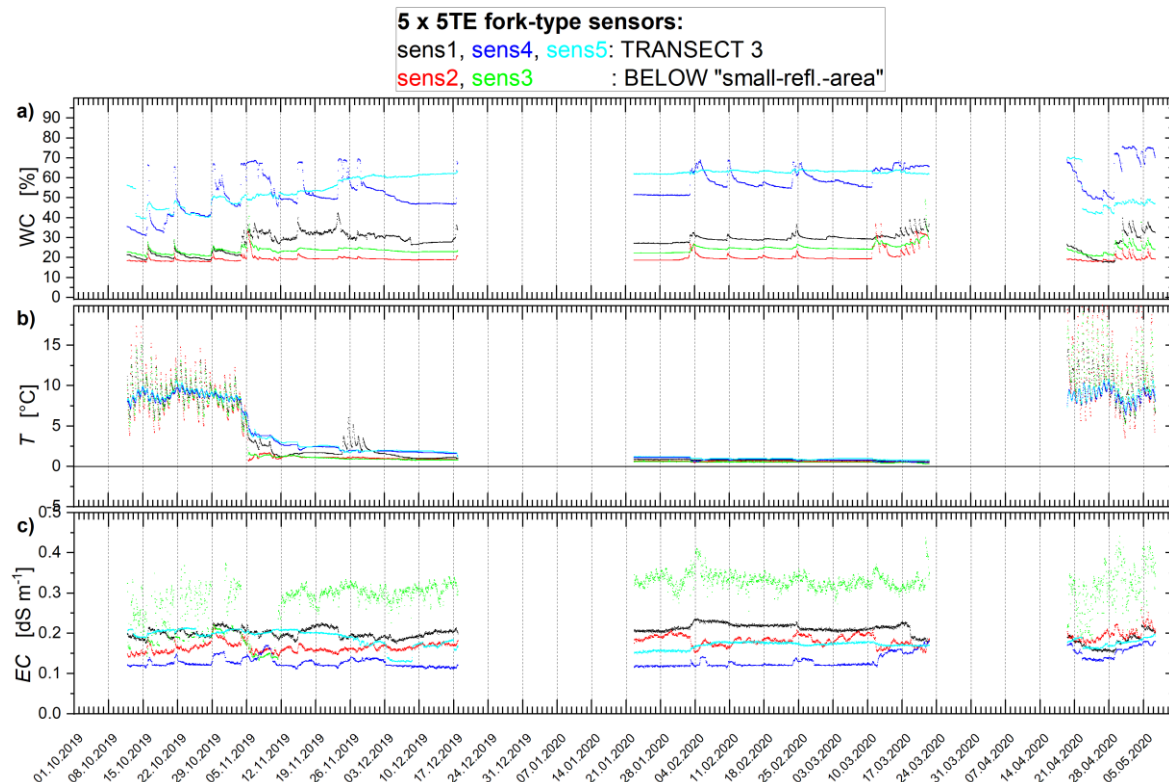


**FIGURE 13.** Measurements from 5TE sensors deployed on Transect 3 and below the “small reflector” shown in the site schematics in **FIGURE 1**. **a)** Volumetric liquid water content ( $WC$ ) of soil; **b)** soil temperature; and **c)** DC Electrical Conductivity ( $EC$ ).

for the radiometer footprint areas, Transect-3 sensors were intentionally placed outside WBScat's field-of-view to avoid spurious scattering from the sensor wires leaking in active measurements.

Additionally, two 5TE sensors (5TE-2 and 5TE3) were placed approximately 5 cm below the soil underneath the “small reflector area” in front of the WBScat (**FIGURE 1**). The idea was to experimentally investigate whether placing such a mesh reflector influences the temporal evolution of underlying soil permittivity and temperature and thus changing the boundary conditions at the snow-ground interface.

The time series of measurements from the in-situ sensors are presented in **FIGURE 13** and **FIGURE 14**. Due to a technical failure of the data logger DT80, two separate gaps are present in in-situ soil measurements: 18 Dec. 2019 — 23 Jan. 2020 and 23 Mar. 2020 — 20 Apr. 2020. Even though it is not ideal to have gaps in the time series, they happened in presence of snowpack with its thermal insulating property. Therefore, it is safe to state that the soil permittivity and temperature did not change significantly especially during the first gap.

Temperature measurements of all sensors (**FIGURE 13 b**) and **FIGURE 14 b), d)**) show that the soil temperature never dropped below 0 °C indicating that the ground at the test site was unfrozen throughout the entire winter. Measurements of volumetric liquid water content ( $WC$ ) and permittivity ( $\epsilon$ ) of natural soil in **FIGURE 13 a)** and **FIGURE 14 c)**, respectively, show that noticeable heterogeneities exist over the site. However, these heterogeneities exhibit themselves more in the absolute value of  $WC$  and  $\epsilon_G$  while the temporal variations are similar. This also means that sensors respond similarly to changes in soil conditions due to air temperature variations (snow-free times), precipitation, and snow melt.

**FIGURE 13 b)** and **FIGURE 14 b), d)** show that the temperature variations gradually diminish with the appearance and thickening of snowpack as shown in **FIGURE 5 e)**. Temperatures decrease gradually from 5 November 2019 when a thin layer of snow (~5 cm) appears over the test site and from 12 November 2019, the temperature values drop close to 0 °C. This effect is due to thermal insulation of snowpack. Comparing soil temperatures measured at different snowpack height  $h_S$  (**FIGURE 5**) shows that upon the melting of the snowpack, the soil temperature resumes its daily fluctuations.

In **FIGURE 13**, sensors 5TE-2 and 5TE-3 (below the “small reflector”) show close values to Sensor 5TE-1 (close to the tower) and they have a similar temporal pattern of temperature and water content variations as 5TE-1. This similarity is true for both snow-free and snow-covered periods, which indicates that the small mesh reflector has not had any tangible effect on the state and temporal evolution of the soil at the snow-ground interface. The reader is reminded that the “small reflector” was placed within the area observed by WBScat to allow studying the

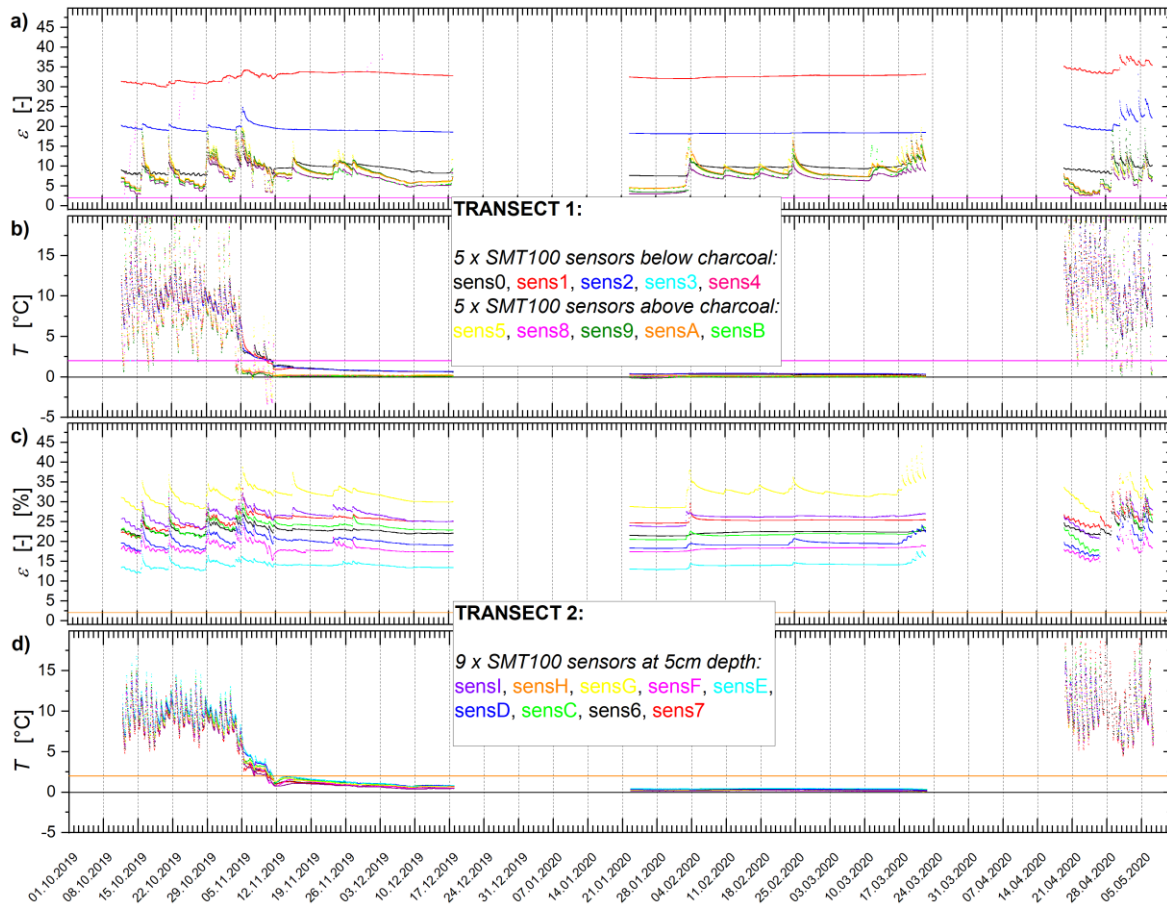


**FIGURE 14.** In-situ measurements with SMT100 sensors deployed along Transects 1 and 2 indicated in **FIGURE 1**. **a)** relative permittivity of the charcoal-mix and sand layers (making up the “charcoal-sand area”) measured with SMT100-0–4 and SMT100-5–B, respectively; **b)** Temperature measurements from sensors on Transect 1; **c)** Relative soil permittivity measured with SMT100 sensors on Transect 2; and **d)** Temperature measurements along Transect 2. Transect 2 sensors are deployed ~5 cm below the soil surface.

volume scattering of the snowpack in different conditions and at different frequencies. For the sake of applicability of such an experiment to snowpack in general, it is naturally important that such an artificial footprint should least influence neither the snow nor the snow-ground interface properties. As a side note it is emphasized once more, that availability of WBScat’s SAR azimuth mode is mandatory to achieve segregated backscatter of the “small reflector area”.

It is reiterated that sensors SMT100-0 to SMT100-4 were placed inside the charcoal-mix layer below the sand layer (see **FIGURE 1**). In **FIGURE 14**, SMT100-1, -2, and -4 clearly show higher permittivity than for sand layer which is expected for charcoal-soil mix. Furthermore, this is an experimental demonstration of the impedance matching effect of the “charcoal-sand area” where permittivity goes through a smooth transition between air ( $\epsilon = 1$ ) and the underlying ground ( $20 \lesssim \epsilon_G \lesssim 40$ ).

a) shows that the permittivity fluctuations during the snow-free period (8.10.2019—12.11.2019) are lower for the charcoal-mix layer due to the insulating effect of the sand layer above which itself undergoes stronger fluctuations in the same period. With the onset of snow cover, the permittivity fluctuations in charcoal-mix layer diminish. However, the sand layer permittivity still responds to major changes in snowpack such as SWE changes after a heavy snowfall, percolation of liquid water through snowpack due to melt, or rain on snow.

With the beginning of the snow-melt (~10 March 2020 evidenced by decreasing snow height  $h_S$  and  $WC_S \gg 0$  mm in **FIGURE 12 a), c)**), the sand layer permittivity in Transect 1 and permittivity measurements along Transect 2 show daily fluctuations. This is thought to be due to liquid water discharge from the melting snowpack whose intensity vary as a function of mainly air temperature.

**FIGURE 13 b)** and **FIGURE 14 b), d)** show that with the snowpack acting as a thermal insulator, the temperatures measured on both transects stay close to but still slightly above  $0^\circ\text{C}$  ( $T \approx 0.2^\circ\text{C}$ ). Again, this corroborates that the soil never froze over the site and hints at the possibility of a moist snow layer at the snow-ground interface. After the complete snow melt, the permittivities as well as soil temperature start an intensifying daily fluctuation as a result of direct exposure of the soil to air temperature and radiation variations.

## 4.2. Snow

The AWS on the site automatically measured snow state parameters such as SWE, snow depth, snow surface temperature etc. Additionally, weekly in-situ snow characterization was conducted by SLF (Davos, Switzerland) to provide both regular reference values for the aforementioned parameters and further measurements such as density and temperature profile, optical and Near-InfraRed (NIR) imagery, as well as Snow Micro Pen (SMP) measurements which yield mass-density and Specific Surface Area (SSA) profiles of the snowpack. These measurements were conducted once a week on Tuesdays between 12 November 2019 and 15 April 2020. Snow density was measured with a 3-cm density cutter.

**FIGURE 15 a)** shows the in-situ measured density profiles during the campaign at the Davos-Laret site. Profiles are color coded based on their measurement date. Additionally, **FIGURE 15 b)** shows a comparison between manual SWE probe and SWE computed based on integrated density profiles. This figure shows the consistency of different measurements and their convergence to similar results for SWE.

The SMP measurements also yield the density and SSA profiles. The latter is of key importance for the interpretation of active remote sensing signatures and simulation of snowpack's

# ESTEC

Deliverable D2+D2a: Preliminary and Final Data Acquisition Report for Davos-Laret during Winter 2019/2020 Campaign

SnowLab-NG

28. Nov. 2020

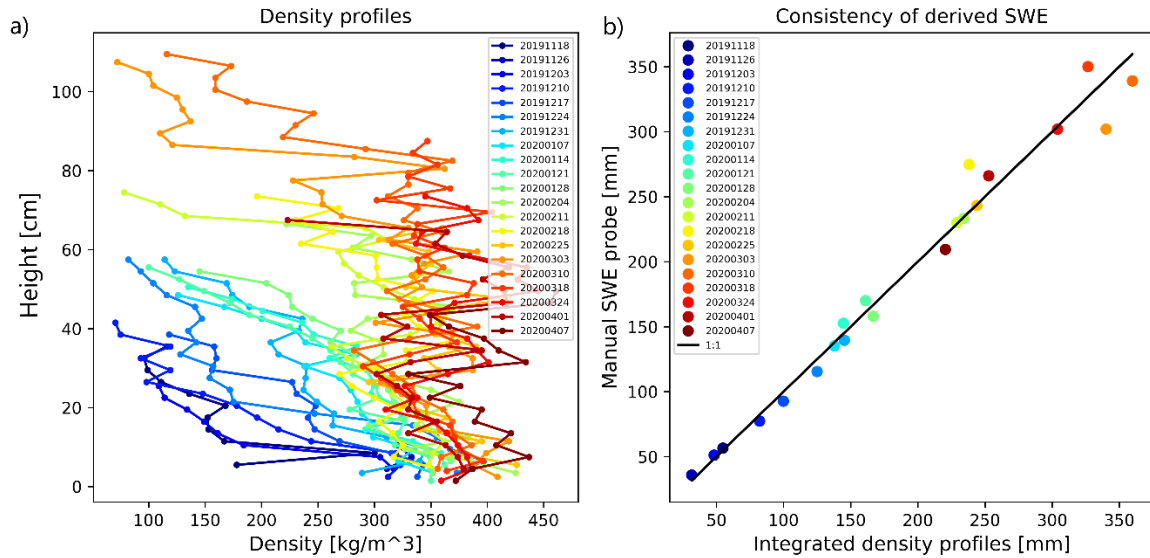


**FIGURE 15. a)** In-situ measured snow density profiles taken during the Winter 2019/2020 campaign; **panel b)** comparison between SWE measured with manual probe and computed using integrated density profiles.

backscattering coefficient at a given frequency. The latter is key to both passive and active remote sensing measurement interpretation and simulation.

Panels a) and b) in **FIGURE 16** show the snow density and SSA profiles derived from SMP measurements over the Davos-Laret site during the Winter 2019/2020 campaign. The difference between snow height measured by the AWS and the profiles, for example on 15 March 2020, is because SMP has certain hard limits on its penetration force to protect the sensor and the integrity of measurements. Therefore, sometimes full penetration through the entire snowpack does not take place.

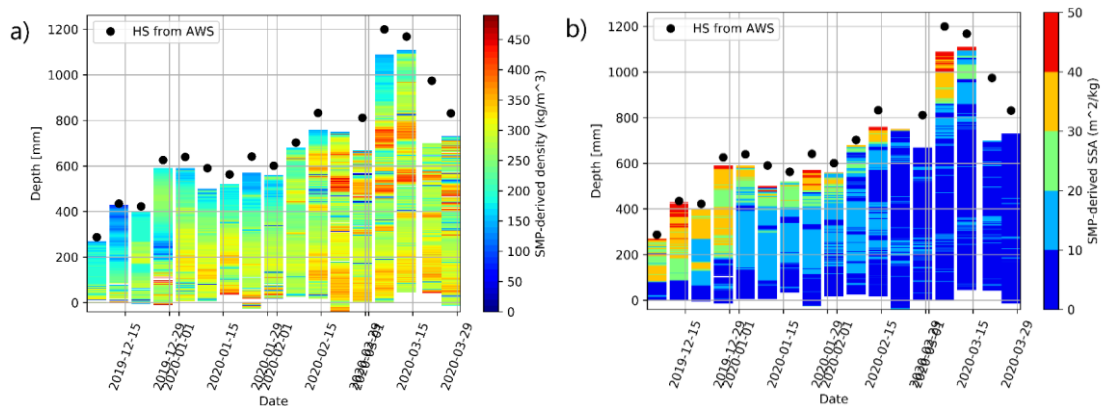


**FIGURE 16. a)** Snow density derived from SMP measurements during the Winter 2019/2020 campaign; **b)** SSA derived from SMP measurements. In both panels, the Snow Height (HS) over the site measured by the AWS is shown with black circles.

## 5. WBSCAT MEASUREMENTS

This section is dedicated to the explanation of active measurements performed with WBScat during the Winter 2019/2020 campaign in Davos-Laret. The Wide-Band Scatterometer (WBScat), under development by Gamma Remote Sensing AG for ESA since 2018, is a fully polarimetric multi-frequency coherent scatterometer designed for tower-based measurement of backscatter of natural media such as snow and/or vegetation. Detailed description of WBScat RF design and assembly can be found in [10].

WBScat is developed based on the heritage from its predecessor SnowScat [11]. While SnowScat was designed for the frequency range of 9 to 18 GHz (X-band), WBScat is designed for the frequency range from 0.1 to 44 GHz. The significantly wider range of measured frequencies necessitates the use of multiple pairs of Transmit (TX) and Receive (RX) antennas. Accordingly, quad-ridge horn antennas covering 0.8–6 GHz, 2–18 GHz, and 10–40 GHz were employed in the RF design. Due to their smaller electrical size, the directivity of these antennas' is significantly lower than for the SnowScat's aperture horn antennas at any given common frequency. Therefore, Synthetic Aperture Radar (SAR) processing is crucially important to achieve higher spatial resolution in the computation of normalized radar cross section  $\sigma^0$ .

### 5.1. Data Acquisition Process

The baseline of WBScat measurements during 2019/2020 campaign was 2D scan of the site for the measurement of scattering parameters in the azimuth range of  $\varphi = -80^\circ$  to  $+60^\circ$  ( $\varphi$  is defined in **FIGURE 19 a**) in 4-degree steps and elevation angles of  $\theta = 25^\circ$ ,  $35^\circ$ , and  $45^\circ$ . This data acquisition process would take approximately four hours to complete and it was regularly done three times a day according to the data acquisition schedule presented in **FIGURE 2**. While numerous details are involved in WBScat 2D scanning of the site, it can be simplified to an eleven-step procedure shown in **FIGURE 17** followed by a brief description of each step. Further technical details are out of the scope of D2/D2a and can be best found in a technical documentation note or user manual for WBScat (to date (25. November 2020) no user manual is officially available).

1. Every routine WBScat measurement, indicated in **FIGURE 2** and including nominal 2D field scans, is included in the Linux "crontab" file to be run diurnally.
2. Upon the defined times every day, crontab runs the "Field\_nominal.sh" shell script which then performs all the consequent 2D scan steps.
3. In this step, the WBScat frame is moved to "home" position in elevation and azimuth angles of  $\theta = 35^\circ$  and  $\varphi = 0^\circ$ , respectively.
4. WBScat is moved on the tomography rail to the 1000 mm position considered as "home" position on the rail for all the 2D scans during the campaign.

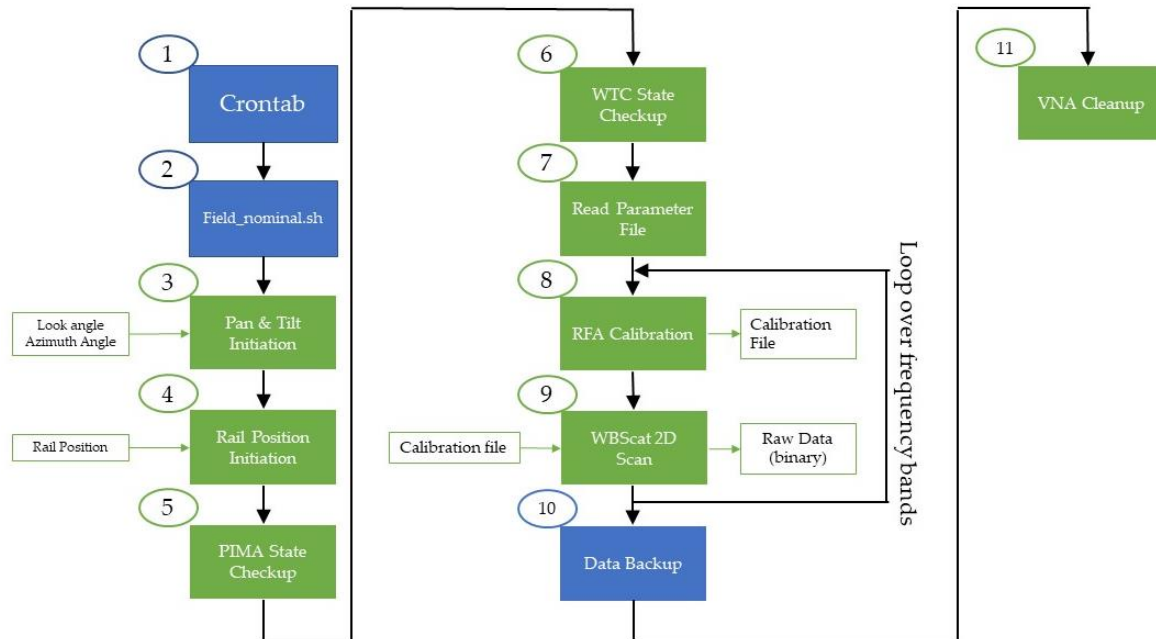


**FIGURE 17.** Flowchart Overview of WBScat nominal data acquisition.

5. The health status of WBScat's **P**ower **C**ontrol **I**nterface **M**icrowave **A**ssembly (**PIMA**) is checked and recorded.
6. The health status of the **W**BScat **T**emperature and **P**ower **C**ontroller (**WTC**) is checked and recorded.
7. The parameter file for the 2D scan is read and uploaded to the code. This parameter file (= profile) contains information on details about VNA settings, azimuth and elevation angle ranges, number of measurement cycles etc. Steps 8. and 9. in **FIGURE 17** are repeated in a loop to cover all three frequency bands considered in each 2D scan.
8. Before measuring scattering parameters of the field, internal calibration of the entire Radio Frequency Assembly (**RFA**) is performed based on the parameters indicated in the measurement profile in Step 7. The internal calibration results are saved, and they are fed to the next step for measuring calibrated scattering parameters during 2D field scan.
9. In this step, WBScat measures three scattering parameters ( $S_{11}$ ,  $S_{12}$ , and  $S_{22}$ ) within the defined frequency range at given elevation and azimuth angles. The 2D sweep is done based on stepwise movement of the instrument in azimuth and elevation. After the 2D scan is over, the loop goes to the next frequency band where a calibration is done followed by another 2D scan of the field.
10. After completion of the 2D field scan for all frequency bands, a copy of the resulting raw data is backed up on the local NAS. Respective files include calibration data, 2D scan scattering parameters, and the executive log of the entire routine task.

11. The VNA's performance may become unstable when its relatively small-sized local memory is fully occupied by temporary measurement and log files created during measurements. As a result, the VNA's memory is cleaned up at the end of each routine measurement to avoid potential VNA instability.

All four types of WBScat routine measurements (2D field scan as the baseline, as well as tomography, external calibration targets, and vertical scan) yield binary files containing  $S$  parameters. This is the “raw data product” from WBScat. However, without post-processing of  $S$  parameters, this data is not of much use and do not provide further insight to the footprint conditions.

## 5.2. Post Processing of WBScat Data

The desired end data product—which is suitable for scientific use and compatible with emission models—from a scatterometer such as WBScat is normalized radar cross section (=backscatter coefficient)  $\sigma^0$  at highest spatial resolution achievable with the setup configuration (tower-based) and post-processing techniques (SAR). The post-processing path between scattering parameter measurements ( $S$  parameters) as raw data from WBScat to  $\sigma^0$  comprises numerous steps whose details are out of the scope of this report and can be best found in textbooks on principles of radar observations and/or a technical documentation for WBScat (not yet available (25. November 2020)). Nevertheless, the entire post-processing is described briefly with four major steps:

### Step 1: Range Compression

It is the process of generating the *range profile* using the transmitted and received signals at any given WBScat elevation and azimuth angle and measurement frequency band. In this step, parameters such as propagation delays due to antenna switches and coaxial cables are considered. The result of this step is *range profile* for each scan where the intensity of received signal is plotted versus slant range. **FIGURE 18** is an example of WBScat range-compressed data in units of power (W). Since a 2D scan is performed over multiple azimuth angles, instead of a conventional two-dimensional range

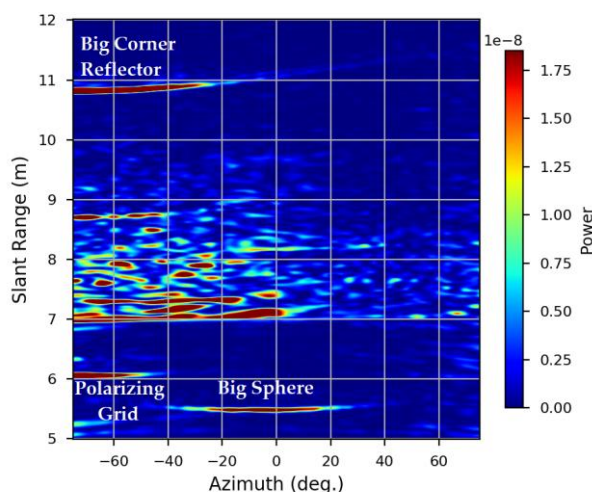


**FIGURE 18.** Colorgraph of range-compressed scattering parameters for a 2D field scan on 8 November 2019 at frequency and bandwidth of 5 GHz and 3 GHz, respectively. The graph is for co-pol VV measurements at elevation nadir angle  $\theta = 35^\circ$ . The major signatures are marked and named.

profile, a colorgraph is employed where power intensity is color coded. As marked with some examples in **FIGURE 18**, the range compressed data already shows clear signs of response to the features and scatterers over the field such as reflectors, polarizing grid, natural or charcoal-mix areas etc.

Step 2: Calibrate Range-Compressed Data

The range compressed signal is calibrated using the antennas' 2-way radiation pattern as well as its cross-polarized response. This information is available from radiation pattern measurements performed at ESTEC's anechoic chamber.

Step 3: Range Gating

Range gating is selection of signals within a given time period of the travel time of the returned signal. The "gate" allows signals to pass through only within the selected travel time. VNA performs coherent measurements of  $S$  parameters whose phase relates to the distance between the antenna and the observed ground. Therefore, signals received with the same phase are backscattered from surface elements whose distance to the antenna is in the same range bin.

Step 4: Azimuth Compression

As explained in Section 5.1. , at each programmed elevation angle the positioner moves WBScat in azimuth to a set of angles specified in the profile. The azimuth angles are selected such that there is at least a 50% overlap of the physical antenna aperture to permit later azimuth compression of the data.

Step 5: Normalized Radar Cross Section Computation

Radar cross section (units of  $m^2$ ) is a measure of how detectable an object is by radar and it can be computed using the general equation below:

$$\sigma = \frac{P_r(4\pi r^2)^2}{P_t G_t A_{eff}} \tag{16}$$

where  $P_r$  and  $P_t$  are received and transmitted power,  $G_t$  is the gain of the transmit antenna,  $A_{eff}$  is the effective aperture area of the radar receive antenna, and  $r$  is the distance between the antenna phase center to the target (slant range). In remote sensing applications, normalized radar cross-section (or backscatter coefficient) is used which is the average radar cross-section of a set of objects per unit area,

$$\sigma^0 = \left\langle \frac{RCS_i}{A_i} \right\rangle \tag{17}$$

where  $RCS_i$  is the radar cross-section of an object and  $A_i$  is the area on the ground associated with that object.

Synthetic Aperture Radar (SAR) processor includes all of the mentioned five steps and results in  $\sigma^0$  computation with high spatial resolution. One can skip step 4 and compute  $\sigma^0$  directly from calibrated range-compressed range-gated data. However, with the significantly wide

beamwidth of the WBScat antennas (see Section 5. ), the spatial resolution will be poor and discrimination between different measurement areas denoted in **FIGURE 1** is suboptimal. Since WBScat's antennas' phase center is not physically located at the same place as the center of azimuth rotation, the geometrical displacement which is the fundamental requirement for SAR processing exists. Furthermore, WBScat performs coherent signal measurements which allows for "focused" SAR processing and thus achieving a higher resolution than unfocused SAR processors.

One challenge in developing a SAR processor for WBScat is its unconventional rotational displacement/scanning mechanism as opposed to linear displacement over e.g. a horizontal rail. Another challenge of observations made with electrically small antenna's is polarization mixing at facet surface elements scale. The V and H polarizations at the antenna aperture are only the same for footprint facets at antenna boresight. However, in case of antennas with wide beamwidths, a noticeable polarization mixing exists at footprint surface elements (facets) further away from the antenna's projected boresight. For more information about this key issue the reader is referred to [12]. However, as of date of this report, there exists no complete SAR processor with polarization mixing correction for WBScat.

In this Data Acquisition Report (D2), aimed at reporting and providing raw data measured in Winter 2019 - 2020 campaign, in addition to raw WBScat data, we offer calibrated range-compressed range-gated data for 2D scans specifically for the natural and charcoal-sand areas.

### 5.3. Extraction of Natural and Charcoal-Sand Area Signatures

In order to extract the signatures of the two footprint areas, calibrated range-compressed WBScat data (Step 2 in Section 5.2) were used for range gating. According to the site schematics in **FIGURE 19 a)**, the "natural ground area" and "charcoal-sand-area" are within azimuth ranges of  $-90^\circ \leq \varphi \leq 0^\circ$  and  $-13^\circ \leq \varphi \leq 64^\circ$ , respectively. However, as shown in **FIGURE 18**, the calibration targets with large RCSs leak into a much wider azimuth range than their actual physical size. Therefore, using the combination of site schematics (**FIGURE 19 a)**) and the Slant Range-Azimuth-Power (SAP) graph, the azimuth and slant range for the two footprints was determined as marked in **FIGURE 19 b)** and given in **TABLE 1**. The power values within these ranges were averaged and reported for a measurement at given polarization combination, frequency, and elevation angle.

**TABLE 1.** Azimuth and slant ranges for two footprint areas.

Footprint	Slant Range	Azimuth Range
Natural Ground Area	7 m to 10.5 m	$-60^\circ$ to $-15^\circ$
Charcoal-Sand Area	7 m to 10.5 m	$15^\circ$ to $60^\circ$

In the following, we are going to use the term "backscatter" signal to refer to the power quantity computed using the method above.

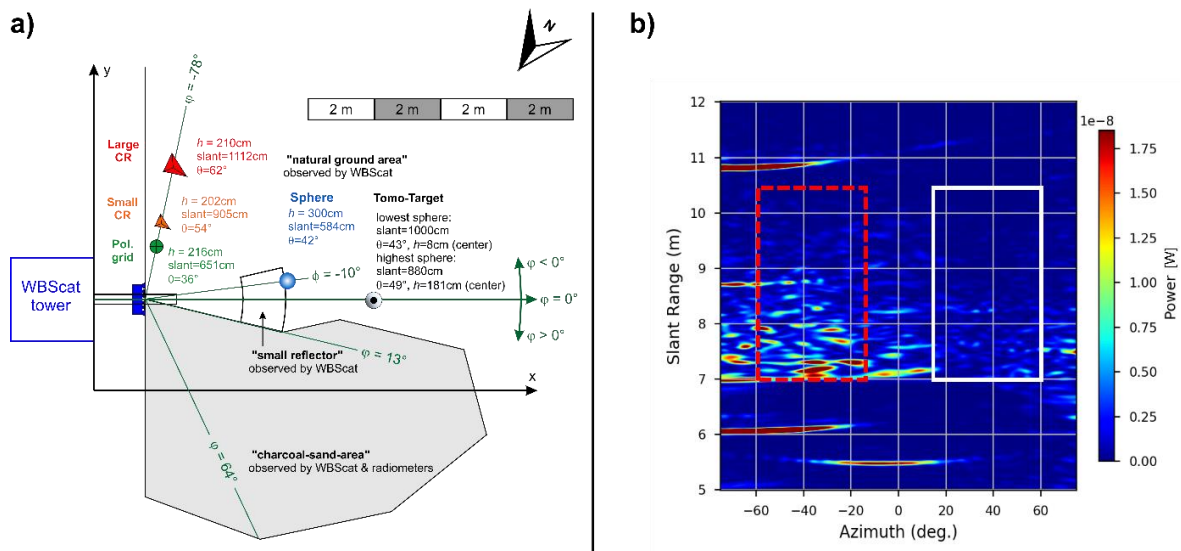


**FIGURE 19. a)** Schematics of WBScat measurement footprint areas and calibration targets; **b)** Example Slant Range-Azimuth-Power (SAP) graph for co-pol VV 2D scan at 5 GHz and elevation angle  $35^\circ$  on 8 November 2019. The dashed-red and white rectangles indicate the considered azimuth/slant-range for natural and charcoal-sand areas, respectively.

#### 5.4. Initial Analysis of WBScat Data

**FIGURE 20** shows an example time series of backscatter (= Calibrated Radar Cross-section (CRC) in units of W) for Winter 2019/2020 at ( $f = 2\text{ GHz}$ ,  $\theta = 25^\circ$ ,  $p = (\text{VV}, \text{VH}, \text{HH})$ ) for the natural and charcoal-sand areas. Several key observations are observed:

- As theoretically expected, the co-pol backscatter is consistently stronger than cross-pol.
- The charcoal-sand area was designed and implemented to prepare a semi-specular surface. It can be seen here for  $f = 2\text{ GHz}$ —and it is true in all frequency bands and elevations angles—that backscatter over “charcoal-sand area” is consistently weaker than over “natural ground area”.
- Some distinct features exist in the co-pol backscatter signals such the relatively steady signal throughout January 2020 and the distinct weekly fluctuations between 2 February

# ESTEC

Deliverable D2+D2a: Preliminary and Final Data Acquisition Report for Davos-Laret during Winter 2019/2020 Campaign

SnowLab-NG

28. Nov. 2020

to 1 March 2020. Use of in-situ measured meteorological and snow data may help better

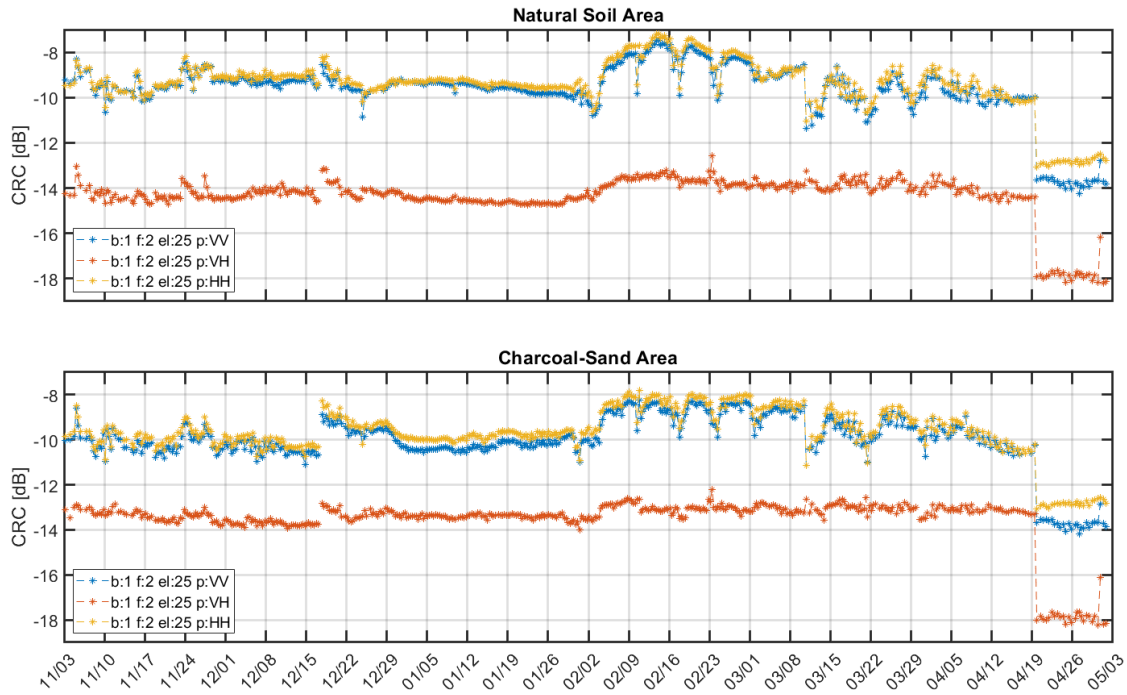


**FIGURE 20.** Time series of backscatter (units of W) measured over the “natural ground area” (top) and the “charcoal-sand area” (bottom). The frequency band, elevation angle, and polarization combination information is provided in the figure legends.

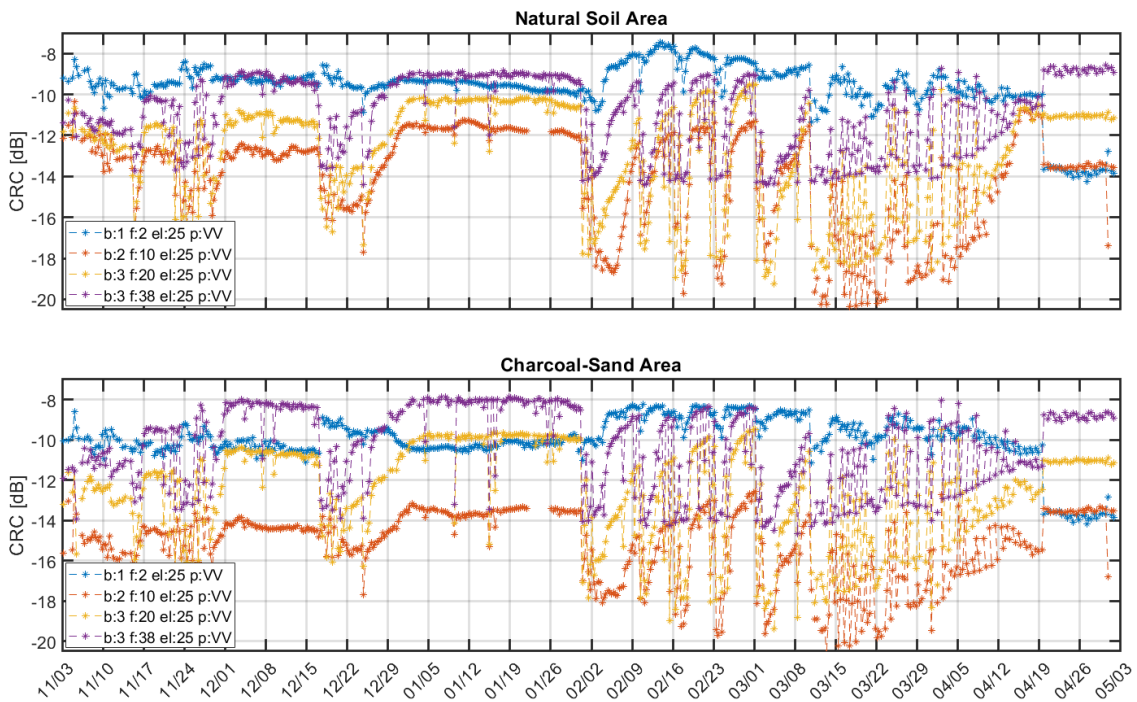


**FIGURE 21.** Time series of measured backscatter (units of W) at four different frequencies over the “natural ground area” (top) and over the “charcoal-sand area” (bottom).

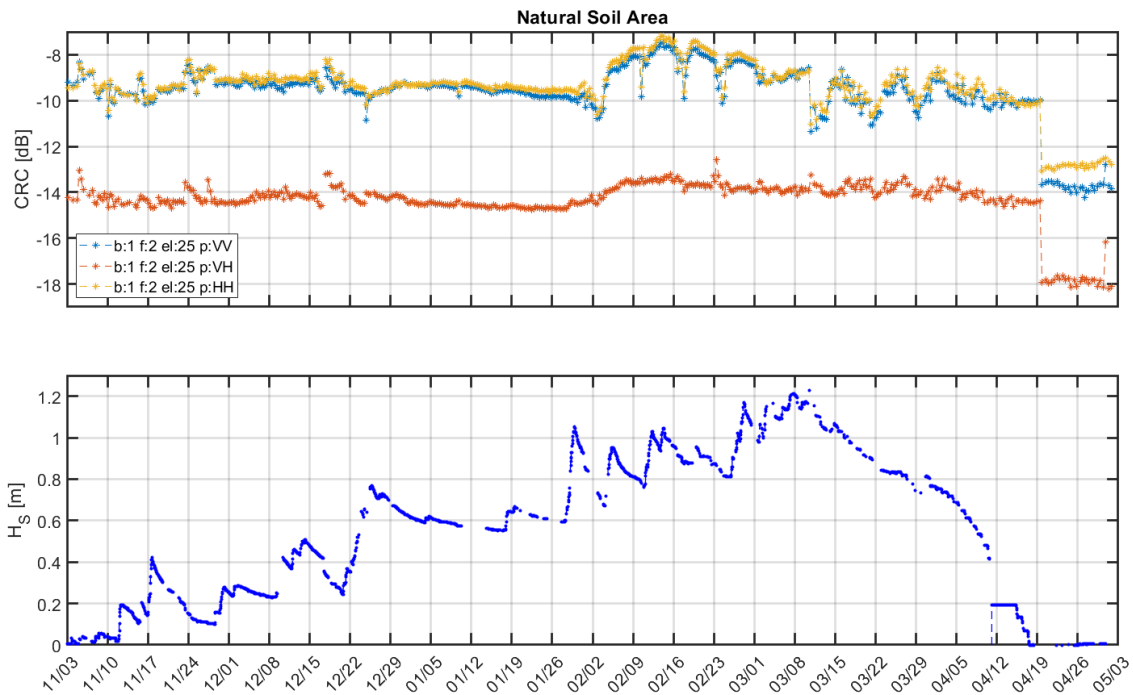


**FIGURE 22.** Upper and lower panels show backscatter time-series ( $f = 2$  GHz,  $\theta = 25^\circ$ ,  $pp = (VV, VH, HH)$ ) and snow height  $H_s$  measured by the on-site AWS.

understand this signal behavior.

- d. Due to a failure in the WBScat's QPT azimuth-elevation positioner, the instrument was mechanically frozen from 19 Apr. 2020 until the end of the campaign. This technical failure is visible in the drop in signal strength in **FIGURE 20**.
- e. **FIGURE 21** presents an example for  $pp = VV$  backscatter time-series measured at four noticeably different frequencies (2, 10, 20, and 38 GHz) across the entire WBScat's frequency range. With increasing frequency, the backscattered signal intensity decreases. This is reasonable observation and it is seen as a successful sanity check.

Better understanding of the time-series of WBScat backscatter measurements shown above requires their examination next to the in-situ measured state parameters in Section 4. and retrieved liquid water column  $WC_S$  in Section 3.6.2.

**FIGURE 22** shows that the backscatter signal responds to quick intense changes in snow height ( $H_s$ ) mainly as a result of heavy snowfall. For example, on 25 December 2019 and 29 January 2020, when  $H_s$  undergoes a rapid increase and decrease of  $\sim 50$  cm and  $\sim 40$  cm, respectively, the backscatter signal responds by dropping to a minimum and gradually recovering to pre-precipitation state.

While the relationship between backscatter and  $H_s$  is somewhat ambiguous, **FIGURE 23** shows a much clearer connection existing between backscatter and liquid water column  $WC_S$  which is

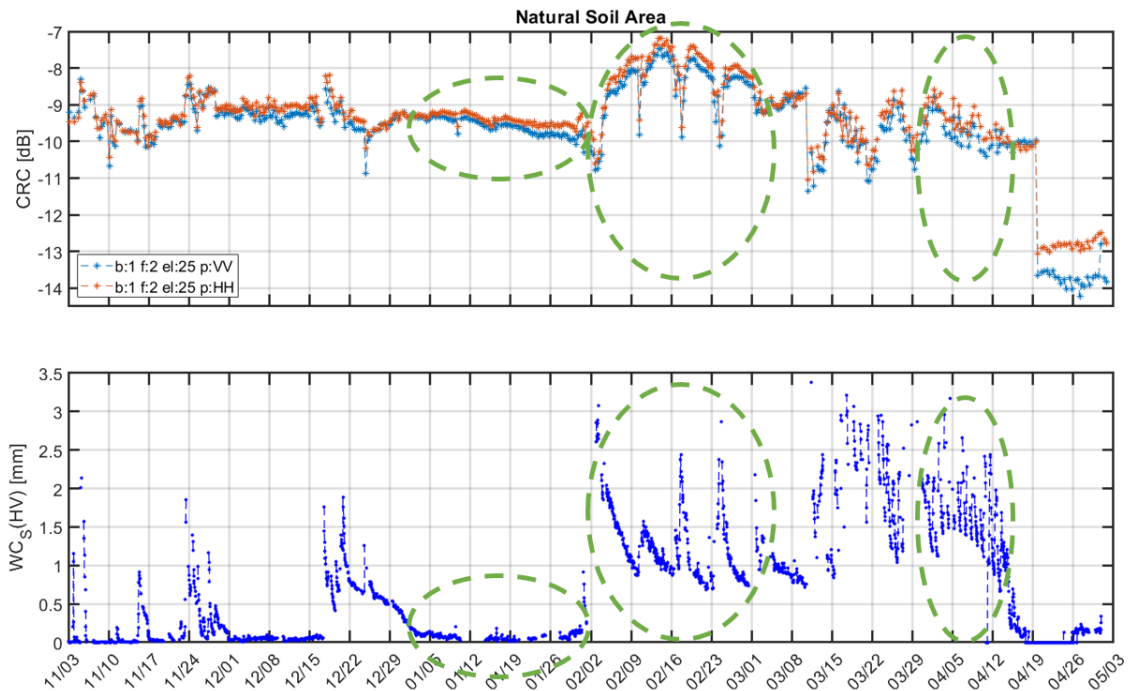


**FIGURE 23.** Time-series of backscatter (units of W) at ( $f = 2$  GHz,  $\theta = 25^\circ$ ,  $pp = (VV, HH)$ ) measured with WBScat (upper panel) and liquid water column  $WC_S$  retrieved from L-band radiometry (lower panel).

independently retrieved from L-band radiometer data over the reflector area (Section 3.6). Three focus periods are highlighted in **FIGURE 23** with green dashed ellipsoids. During almost the entire January 2020—cold winter period with virtually dry snowpack, the backscatter signal is steady. With increasing air temperatures and wet-snow/rain precipitation (**FIGURE 5 d**), the backscatter signal shows an anti-correlation with  $WC_S$  which is best visible for the period 2 February to 1 March 2020. Later during the melt-season the daily  $WC_S$  variations of the melting snowpack also seems to show influence backscatter daily signal variations. It is not easy to compare such variations on hourly basis because while  $WC_S$  from radiometry is available every hour, the WBScat measurements are only available three times per day.

Scatterplots of backscatter signal versus  $WC_S$  for three frequency bands (band 1: 1 GHz – 6 GHz; band 2: 6 GHz – 18 GHz; band 3: 18 GHz – 44 GHz) and two polarization combinations (VV and HH) are shown in **FIGURE 24**. **FIGURE 24 a)–d)** show an anti-correlation between backscatter signal and  $WC_S$  for  $WC_S \gtrsim 0.5$  mm for the frequency range 1 GHz – 16.5 GHz (bands 1 and 2) for both  $pp = HH$  and  $pp = VV$ . However, this anti-correlation is frequency dependent and it is practically missing for the highest frequency band 3 (18 GHz – 44 GHz). For small amount of snowpack liquid water column ( $0 \text{ mm} \leq WC_S \leq 0.5 \text{ mm}$ ), there is no specific relationship between backscatter signal and snow wetness. This is a reasonable

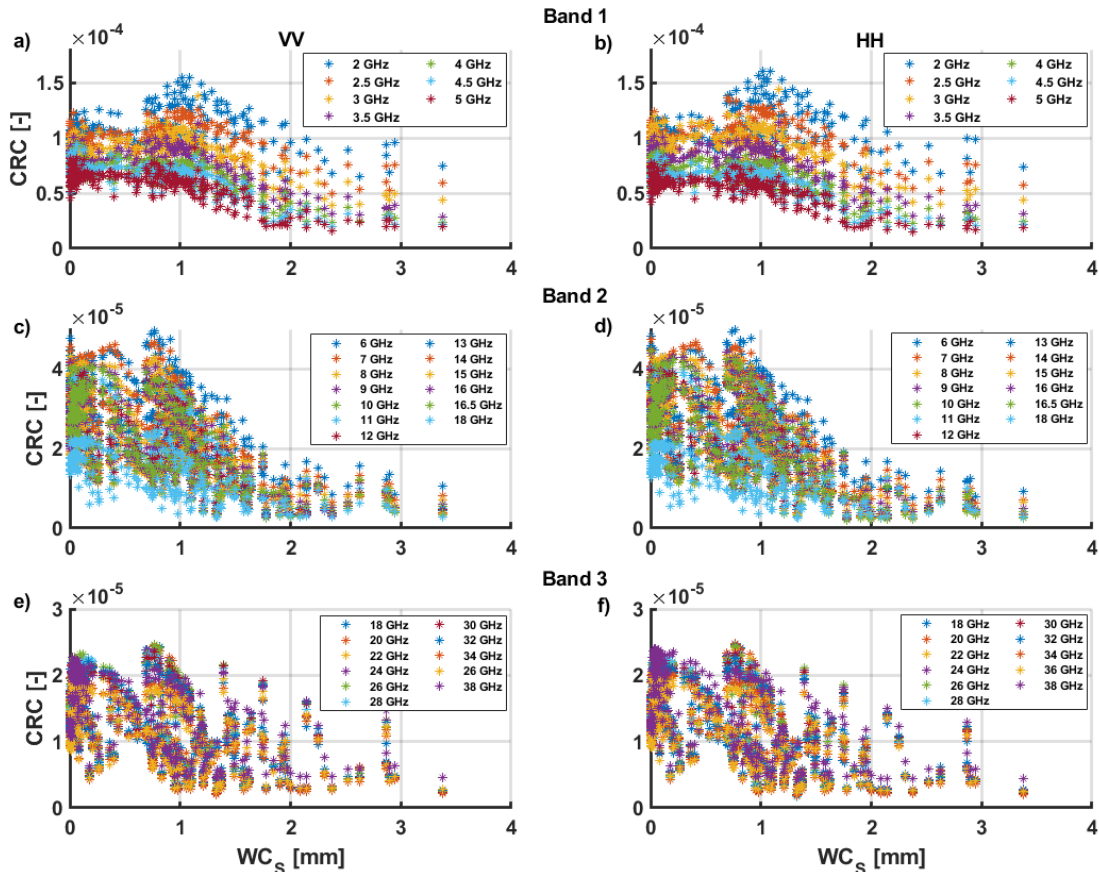


**FIGURE 24.** Scatterplots of backscatter signal versus snow liquid water column  $WC_S$ . Each row corresponds to a frequency band (Bands 1—3) and each column to polarization combination  $pp = VV$  and  $HH$ . Bands 1—3 refer to the frequency ranges band 1: 1 GHz – 6 GHz; band 2: 6 GHz – 18 GHz; band 3: 18 GHz – 44 GHz.

observation as the penetration losses as well as volume scattering in dry snow are minimal especially at lower frequencies ( $\equiv$  longer wavelength). The lack of such a relationship between backscatter and  $WC_S$  at higher frequencies is because with decreasing wavelengths, smallest changes in snowpack micro-structure (such as correlation length) can strongly influence the scattering properties of snow.

It is also noteworthy that the slope of a hypothetical linear fit to the data in **FIGURE 24 a)–d)** is more negative (steeper) for Band 2 compared to Band 1 which further illustrates the frequency dependency of backscatter as a function of  $WC_S$ .

A key snow state parameter of interest in Snowlab-NG is SWE which in its simplest form is snowpack height times its mean mass-density  $SWE = h_S \cdot \rho_S$ . Theoretically and according to the available emission models (e.g. MEMLS 3&a [13]), snowpack height and density, together with multiple other state parameters, influence the backscattering coefficient of snowpack. Furthermore, it was shown in **FIGURE 22** that the backscatter signal responds to distinct  $H_S$  variations. However, as seen in **FIGURE 25**, no obvious relationship exists between the backscatter signal and the directly measured SWE.

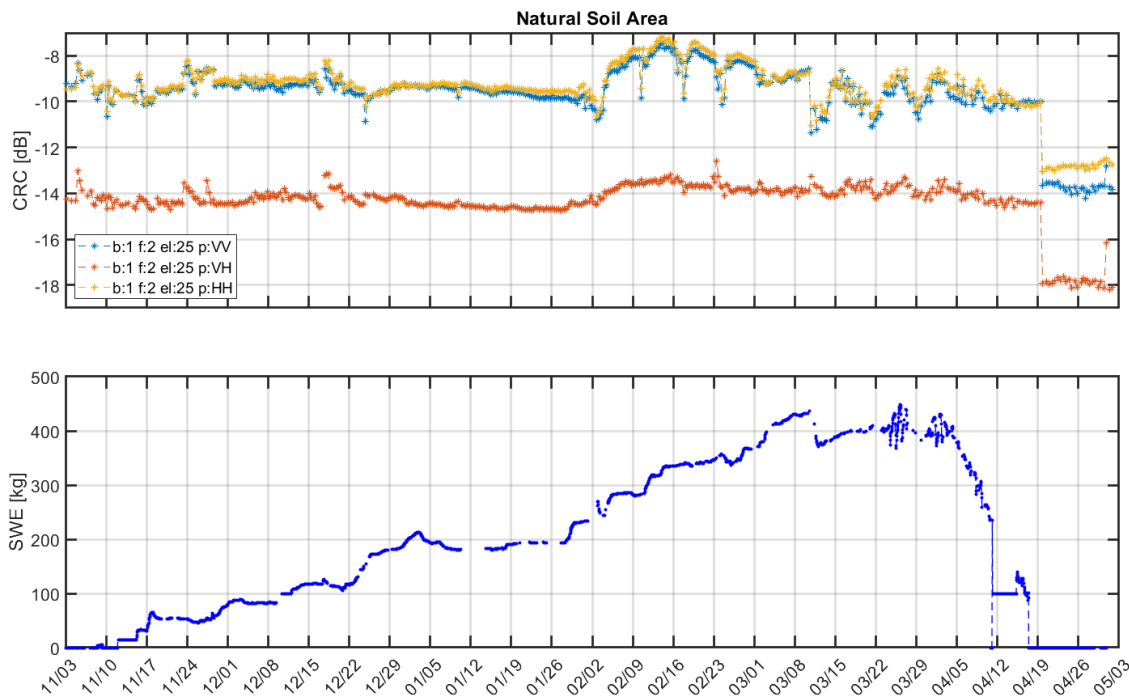


**FIGURE 25.** Upper panel: time-series of backscatter signal (units of W,  $f = 2$  GHz,  $\theta = 25^\circ$ ,  $p = (VV, VH, HH)$ ); lower panel: SWE measured with gravity gauge at the AWS.

To understand this contradiction between theoretical expectation and experimental observation, one must notice that the backscatter signal is influenced by numerous state parameters (such as  $\rho_s$ ,  $WC_s$ , SWE, microstructure etc.) where each of them has its own characteristic time-scale of changes. For example, snow wetness can change in a few hours; however, except for intense snow fall events, snow height changes over days and weeks. To further investigate the effect(s) of state parameters on the backscatter signal, cross-correlation between each of the state parameters and the backscatter at given  $(f, \theta, p)$  was computed using an asymmetric moving window of length  $T$  hours. **FIGURE 26** shows the coefficient of determination  $R^2$  for dry snow precipitation calculated using the past  $T = 96$ -hours (4 days) of measurements at each time  $t$ . **FIGURE 26** shows that for almost exclusively all instances of snow precipitation,  $R^2$  increases from  $\sim 0$  to a maximum and shortly after the end of the precipitation, the correlation between precipitation and radar backscatter also drops to zero such as the case of 22 - 30 December 2019. In some cases, the precipitation events take place regularly over several days; therefore, during that time  $R^2$  does not completely drop down to 0 before it reaches another local maximum.

# ESTEC

Deliverable D2+D2a: Preliminary and Final Data Acquisition Report for Davos-Laret during Winter 2019/2020 Campaign

SnowLab-NG

28. Nov. 2020

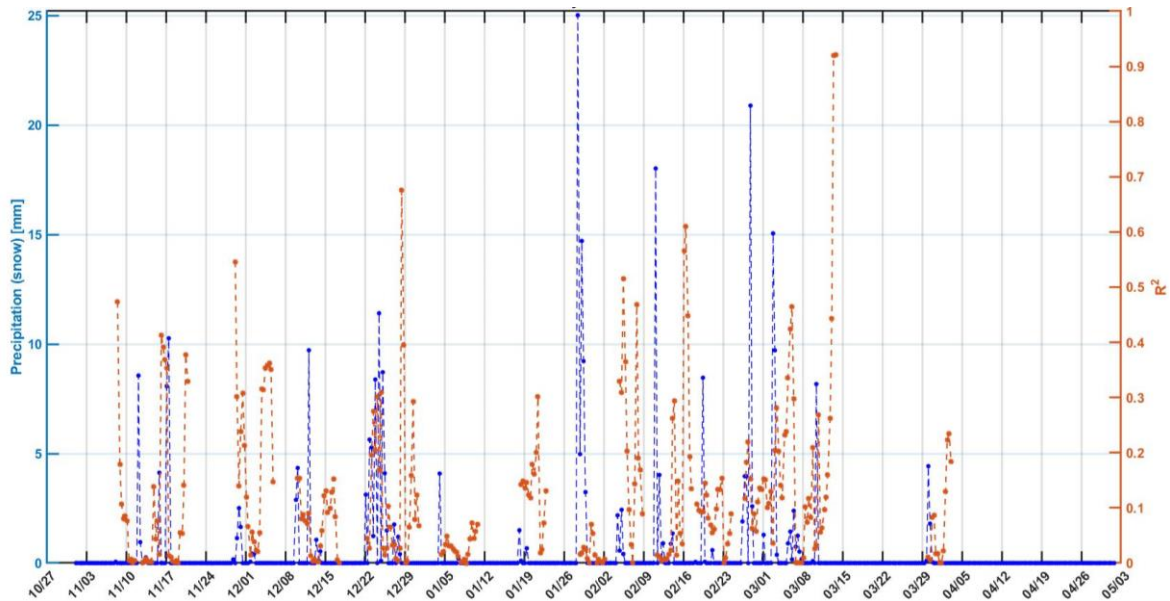


**FIGURE 26.** Left axis shows dry snow precipitation  $T_{air} < 0^{\circ}\text{C}$  with blue line. Right axis shows the coefficient of determination  $R^2$  computed between radar backscatter ( $f = 2 \text{ GHz}$ ,  $\theta = 25^{\circ}$ ,  $p = VV$ ) and snow precipitation in an asymmetric moving window of length  $T = 96$  hours (4 days).

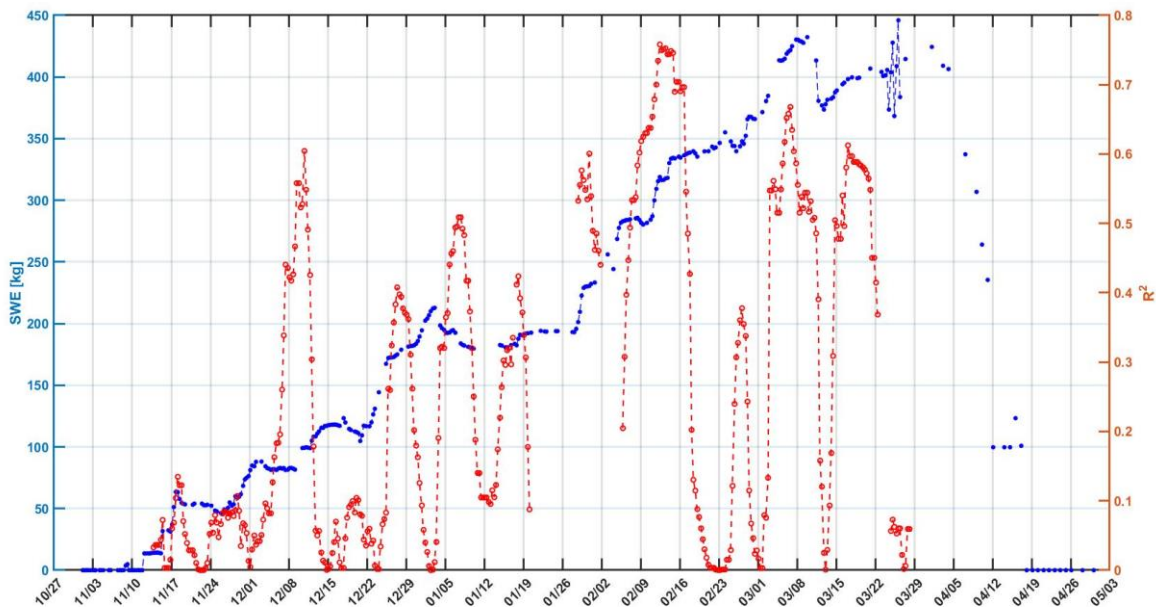


**FIGURE 27.** Left axis shows snow water equivalent (SWE) with blue line. Right axis shows the coefficient of determination  $R^2$  computed between radar backscatter ( $f=2 \text{ GHz}$ ,  $\theta = 25^{\circ}$ ,  $pp=VV$ ) and SWE in an asymmetric moving window of length  $T = 96$  hours (4 days).

For the case of SWE, choosing a short time window of four days or less, results in  $R^2$  time-series with close-to-noise pattern. Considering the expected longer SWE fluctuation time scale,  $R^2$  is calculated for  $T = 14$  days with similar results for  $12 \text{ days} \leq T \leq 16 \text{ days}$ . **FIGURE 27** shows the SWE time-series in blue (left axis) and  $R^2$  for SWE and radar backscatter ( $f =$

2 GHz,  $\theta = 25^\circ$ ,  $pp = VV$ ) in red (right axis). Our preliminary investigation on  $R^2$  for SWE and radar backscatter indicate a reasonable; yet not fully proven, relation between the two parameters. For example, on 17 November 2019 an increase of  $\sim 40$  kg in SWE over a few hours increases  $R^2$  and this correlation gradually falls to zero. A similar pattern can be seen in period 6–23 February 2020 indicating a direct relationship between  $R^2$  and radar backscatter. However, our investigation of  $R^2$  between radar backscatter and snow precipitation performed for different sets of radar backscatter ( $f, \theta, p$ ) show that such a relationship is certainly neither linear nor frequency independent. Further investigation is required using backscattering coefficients  $\sigma^0$  to gain more in-depth understanding of each state parameter's influence on the radar measurements.

The main message from the preliminary analyses presented in this section of D2/D2a is the existence of meaningful sensitivity of radar backscatter to (at least) some of the snow-ground state parameters. This sensitivity is the key requirement to determine the possibility of and later devise retrieval approaches for snow state parameters such SWE.

## 6. LESSONS LEARNED

The winter 2019-2020 campaign in Davos-Laret shed light on several technical and scientific aspects for such a complex remote sensing campaign and resulted in several precious lessons learned for improved campaigns of such sort in future. Here we count the most important lessons:

### 1. Temporal resolution of active measurements

The WBScat measurement plan was devised to achieve three main goals: measurements over three types of footprints (charcoal-sand area, natural area, and the small reflector), tomographic profiling of snow cover, and ensuring enough overlap between consecutive footprints for later azimuth focusing. This seriously reduced the temporal resolution of nominal field scans.

For the winter 2020-2021 campaign at FMI-ARC, we have decided to remove tomographic profiling as it is not a main scientific objective of APRESS or SnowLab-NG. This saves 4 hours of measurement time every day. The azimuth scanning range has also been reduced. This still allows for azimuth focusing but takes less time finish one scan. With these considerations, the temporal resolution will be improved to two hours (12 measurements per day).

### 2. Mechanical and Electrical Integrity of the Systems

WBScat frame did not have a proper cover to protect the antenna ports and the RF cables from snow and rain. We designed and built an aluminum cover which significantly helped keep these sensitive components clean.

The elevation-azimuth scanning of ELBARA was also occasionally faulty. System inspection revealed lack of sufficient input power as the main problem. Therefore, the original power supply was replaced by two stronger power supplies each one dedicated to one JVL servo motor.

## 7. REFERENCES

- [1] R. Naderpour, M. Schwank, and C. Mätzler, "Davos-Laret Remote Sensing Field Laboratory: 2016/2017 Winter Season L-Band Measurements Data-Processing and Analysis," *Remote Sensing*, vol. 9, no. 11, p. 1185, 2017.
- [2] M. Schwank, R. Naderpour, and H. Löwe, "SnowLab-NG D1: Campaign Implementation Plan (CIP) of the Davos-Laret Winter 2019/2020 Campaign," Swiss Federal Institute WSL, D1 of ESAs SnowLab-NG project May 2020 2020.
- [3] T. Pellarin *et al.*, "Two-year global simulation of L-band brightness temperatures over land.," *IEEE Trans. Geosci. Remote Sensing*, vol. 41, no. 9, pp. 2135-2139, 2003.
- [4] K. Schneeberger, C. Stamm, C. Mätzler, and H. Flüher, "Ground-based dual-frequency radiometry of bare soil at high temporal resolution," *IEEE Transactions on Geoscience and Remote Sensing*, vol. 42, no. 3, pp. 588-595, 2004.
- [5] D. Houtz, R. Naderpour, M. Schwank, and K. Steffen, "Snow wetness and density retrieved from L-band satellite radiometer observations over a site in the West Greenland ablation zone," *Remote Sensing of Environment*, vol. 235, p. 111361, 2019/12/15/ 2019.
- [6] M. Schwank *et al.*, "Model for microwave emission of a snow-covered ground with focus on L band," *Remote Sensing of Environment*, vol. 154, pp. 180-191, 2014.
- [7] M. Schwank and R. Naderpour, "Snow Density and Ground Permittivity Retrieved from L-Band Radiometry: Melting Effects," *Remote Sensing*, vol. 10, no. 2, p. 354, 2018.
- [8] R. Naderpour, M. Schwank, C. Mätzler, J. Lemmetyinen, and K. Steffen, "Snow Density and Ground Permittivity Retrieved From L-Band Radiometry: A Retrieval Sensitivity Analysis," *IEEE Journal of selected topics in applied earth observations and remote sensing*, vol. 10, no. 7, pp. 3148 - 3161, 2017.
- [9] R. Naderpour, "Passive L-Band Remote Sensing Applications Over Cryospheric Regions," Zurich, ETH Zurich, 2019.
- [10] C. Werner, M. Suess, U. Wegmüller, O. Frey, and A. Wiesmann, "The Esa Wideband Microwave Scatterometer (Wbscat): Design and Implementation," in *IGARSS 2019-2019 IEEE International Geoscience and Remote Sensing Symposium*, 2019, pp. 8339-8342: IEEE.
- [11] C. Werner, A. Wiesmann, T. Strozzi, M. Schneebeli, and C. Matzler, "The snowscat ground-based polarimetric scatterometer: Calibration and initial measurements from Davos Switzerland," in *Geoscience and Remote Sensing Symposium (IGARSS), 2010 IEEE International*, 2010, pp. 2363-2366.
- [12] R. Naderpour, D. Houtz, and M. Schwank, "Snow Wetness Retrieved from Close-Range L-Band Radiometry in the Western Greenland Ablation Zone," *Journal of Glaciology*, vol. In review, 2020.
- [13] M. Proksch *et al.*, "MEMLS3&a: Microwave Emission Model of Layered Snowpacks adapted to include backscattering," (in English), *Geoscientific Model Development*, vol. 8, no. 8, pp. 2611-2626, 2015.

ESTEC

Deliverables D8/D8a: Preliminary/Final Data Acquisition Report Sodankylä (2<sup>nd</sup> season)”

*SnowLab-NG*

4. Apr. 2022

**ESA CONTRACT NO. 4000130865/20/NL/FF/AN  
with  
WSL-BIRMENS DORF**

**SnowLab-NG**

**Deliverable D8 & D8a:**

**D8: “Preliminary Data Acquisition Report Sodankylä (2<sup>nd</sup> season)”**

**D8a: “Final Data Acquisition Report Sodankylä (2<sup>nd</sup> season)”**

**WSL-BIRMENS DORF REFERENCE NUMBER: WSL-Birmensdorf\_ESTEC/SnowLab-NG**

Created: 3. March 2022

Authors:

Reza Naderpour, WSL-Birmensdorf  
Mike Schwank, WSL-Birmensdorf  
Derek Houtz, WSL-Birmensdorf  
Henning Löwe, WSL-Davos (SLF)



 **GAMMA REMOTE SENSING**

## TABLE OF CONTENTS

1. Introduction .....	2
2. tower-based Passive Microwave radiometry.....	3
3. Meteorological and in-situ Snow Measurements .....	4
4. Tower-Based Wide-Band Scatterometry .....	5
5. Time-Series of L-Band Radiometer <b>TBp, <math>\theta</math></b> and Meteo-Data.....	6
6. Wide-Band Scatterometry .....	7
7. Lessons learned .....	10
8. Manual in-situ Snow Characterization.....	11
9. Appendix: Data Formats .....	11
10. References .....	13

## 1. INTRODUCTION

This document presents Deliverable D8 “Preliminary Data Acquisition Report Sodankylä (2<sup>nd</sup> season)” and D8a “Final Data Acquisition Report Sodankylä (2<sup>nd</sup> season)” of the SnowLab-NG project. It includes the close-range passive- and active microwave measurements, as well as accompanying meteorological and in-situ data collected at the Finnish Meteorological Institute’s Arctic Research Center (FMI-ARC) during the Winter campaign 2020/2021. In this document, an overview of the time-series of selected sets of key measurements are presented and discussed. Concise analysis of a few key features of the data are also included to both provide further insight into the campaign and examples on how the data set of active-passive Remote Sensing (RS) and in-situ measured data can be utilized in future analyses.

The SnowLab-NG’s second campaign during Winter 2020/2021, which took place in Sodankylä, aimed at studying the response of the close-range L-band brightness temperature and wide-band radar backscatter to the evolving snow cover and its underlying ground. There exist numerous key differences between SnowLab-NG’s site for the first (Davos-Laret, Switzerland) and the second (Sodankylä, Finland) measurements campaign. These differences include climate, underlying ground’s freeze/thaw state, snow cover properties, and length of the snow cover period in each winter, exposure to radiation given vastly different lengths of days etc. Thus, performing the second campaign over the Arctic circle at FMI-ARC gives the chance to study which type of information about snow and its subnivean layer can be extracted from a similar set of measurements and whether and to what extent the findings in an alpine site are applicable to the high latitude arctic region and vice versa.

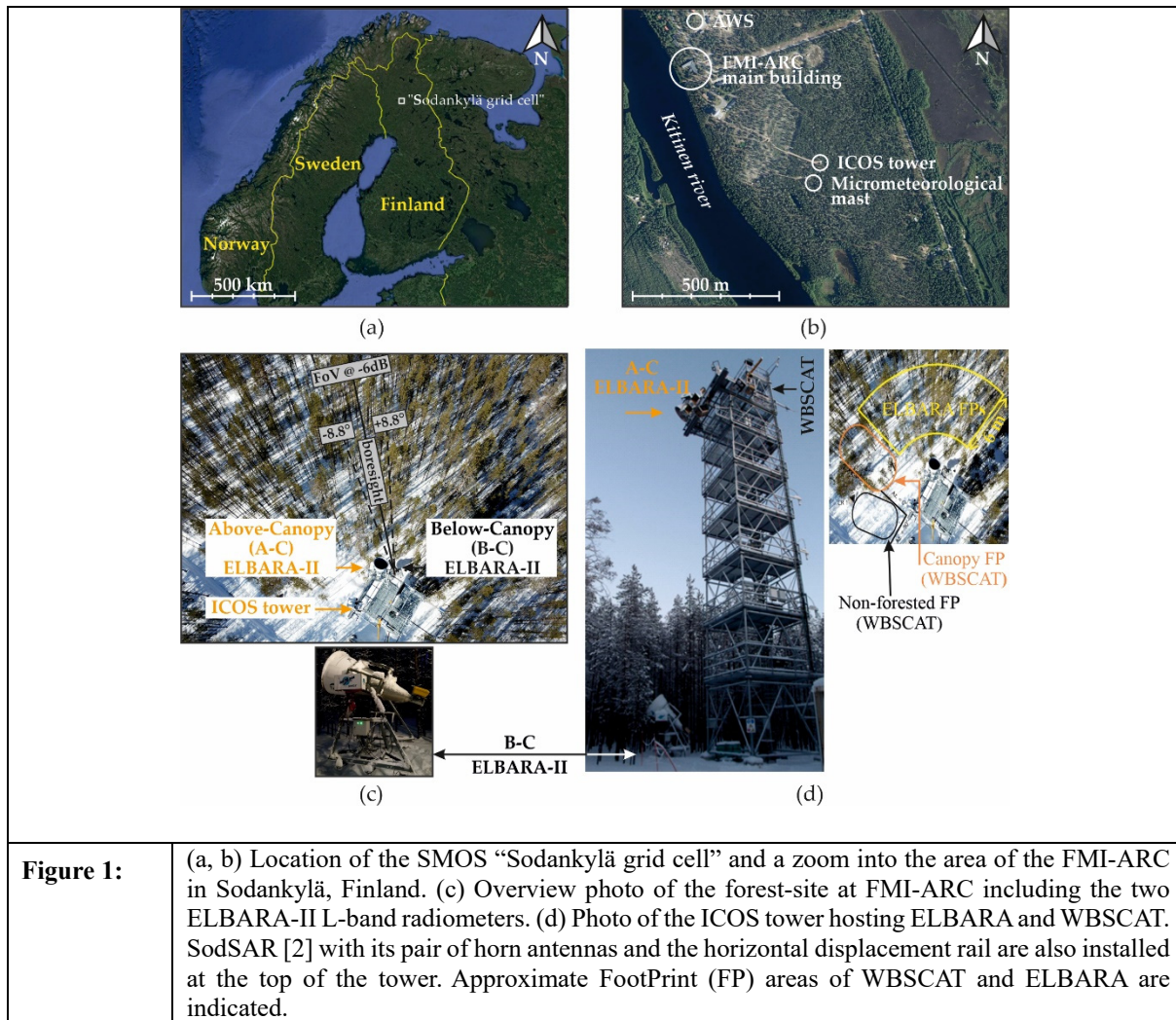
In the following, we first describe the measurement setup used for passive (Section 2. ) and active (Section 4. ) measurements, and auxiliary measurements (Section 3. ). In Sections 5. and

6. time series of measurements are provided, followed by the description of data provided with this deliverable (Appendix).

## 2. TOWER-BASED PASSIVE MICROWAVE RADIOMETRY

As shown in **Figure 1**, an ELBARA radiometer, mounted on an elevation tracking system and attached to a large Picket-horn antenna with a Field-of-View (FoV) of  $\sim 12^\circ$ , is installed at the approximate height of 23 m above the ICOS tower at FMI-ARC. This downward looking Above-Canopy (AC) ELBARA radiometer measures L-band brightness temperatures  $T_B^{p,\theta}$  at a nadir angle range of  $\theta = \{30^\circ, 35^\circ, \dots, 175^\circ, 180^\circ\}$  thus measuring the L-band thermal emission of the ground and canopy, the horizon, and the sky with time resolution of one hour. For redundancy and better statistical sample size, at each given nadir angle, several measurements were conducted. It is noteworthy that from the start of the campaign (1. November 2020) until 17 March 2021, ELBARA-II performed the downward looking Above-Canopy measurements. From 29 March 2021, an ELBARA-III was used until the end of the campaign on 1 June 2021. These two models of ELBARA have a similar Radio Frequency Assembly (RFA) design which employs an internal Resistive Source and an Active Cold Source whose noise temperature can be determined using sky measurements. The method for the computation of calibrated L-band  $T_B^{p,\theta}$  from ELBARA raw data is comprehensively explained in [1].

The data package from the Winter 2020/2021 campaign in Sodankylä includes  $T_B^{p,\theta}$  at all measurement cycles at a given time and given  $\theta$  as well as data for all the available  $\theta$ . Whenever, data is missing or has been filtered due to RFI, the value of -9999 is set. However, in this report in **Figure 2** we show time series of  $T_B^{p,\theta}$  for  $\theta = \{30^\circ, 35^\circ, 40^\circ, 45^\circ, 50^\circ, 55^\circ, 60^\circ, 65^\circ\}$ .



### 3. METEOROLOGICAL AND IN-SITU SNOW MEASUREMENTS

An Automatic Weather Stations (AWS) measures main meteorological parameters autonomously at FMI-ARC. Below is the list of sensors employed on the AWS. We provide hourly averages of measured parameters in this report and with the associated data-package.

- Sensor for temperature: PT100
- Sensor for humidity: Vaisala HMP
- Sensor for air pressure: Vaisala PTB201A
- Sensor for snow depth: Campbell Scientific SR50
- Sensor for visibility, present weather and precipitation: Vaisala FD12P (optical sensor)
- Sensor for precipitation: Ott Messtechnik GmbH & Co. Kg Pluvio2 (2013-09-04 ->)
- Sensor for wind speed and gust (22m): Vaisala WAA25
- Sensor for wind direction (22m): Vaisala WAV15
- Sensor for clouds: Vaisala CT25K

Radiation information, including Long Wave (LW) solar radiation, LW outgoing solar radiation, Reflected Radiation, and sunshine duration is taken from the FMI’s publicly available online data repository.

Additionally, a Sommer Messtechnik SSG 1000 sensor, which is installed close to the ICOS tower, measures Snow Water Equivalent (SWE) by weighting the snow accumulating over its central panel. These autonomous measurements are also taken from the FMI online data repository.

#### 4. TOWER-BASED WIDE-BAND SCATTEROMETRY

As shown in **Figure 1 d)**, ESA’s Wide-Band Scatterometer (WBSCAT) [3-6] was deployed atop the ICOS tower at the height of 19 m from the ground. WBSCAT performed two-dimensional (2D) azimuth and elevation scans to measure the radar backscatter in the frequency range of 1 GHz to 33 GHz. The WBSCAT regular scans were performed every two hours, which provided a significantly improved temporal resolution compared to three measurements per day for the first campaign (2019/2020) performed at the Davos-Laret Remote Sensing Field Laboratory (Switzerland) [7]. This was possible by saving time through first dropping the tomography measurements which could take up to 6 hours each time and second selecting six specific frequency bands within 1 GHz to 32 GHz.

**Table 1** offers a summary of the WBSCAT measurement details and settings. Approximate FootPrint (FP) areas of WBSCAT (and ELBARA) are indicated in the right part of **Figure 1 (d)**. The 2D scanning capability of WBSCAT allowed to measure backscatter along multiple directions which potentially reveals the effect of spatial heterogeneities and environmental features if and when Synthetic Aperture Radar (SAR) processing software is available for this system. Furthermore, as shown in **Figure 1 (d)**, WBSCAT was attempted to measure backscatter from both the canopy and the treeless area close to the tower and service road. The azimuth angle ranges associated with these two regions are given in **Table 1**.

**Table 1:** Summary of the WBSCAT measurement details and settings used during 2<sup>nd</sup> campaign in Sodankylä.

Parameter	Value
Central Frequencies [GHz]	2, 6, 10, 16, 20, 32
Bandwidth [GHz]	2 GHz
Azimuth $\varphi$ range	-60° to -20°
Elevation $\theta$ steps	25°, 40°
$\varphi_{\text{Ground}}$	(-60, -45)
$\varphi_{\text{Canopy}}$	(-35, -20)
Measurement times	1:00, 3:00, 5:00, 7:00, 9:00, 11:00, 13:00, 15:00, 17:00, 19:00, 21:00, 23:00

## 5. TIME-SERIES OF L-BAND RADIOMETER $T_B^{p,\theta}$ AND METEO-DATA

As mentioned in Section 1. , ELBARA-II and ELBARA-III were used at FMI-ARC in Sodankylä (Finland) during the Winter 2020/2021 campaign to measure the L-band thermal emission from above the canopy. Panels (a-f) in **Figure 2** show the time series of L-band brightness temperatures  $T_B^{p,\theta}$ , snow depth  $SD$ ,  $SWE$ , precipitation intensity  $Prec.$ , and air temperature 2 m above the surface  $T_{air}$ , respectively.

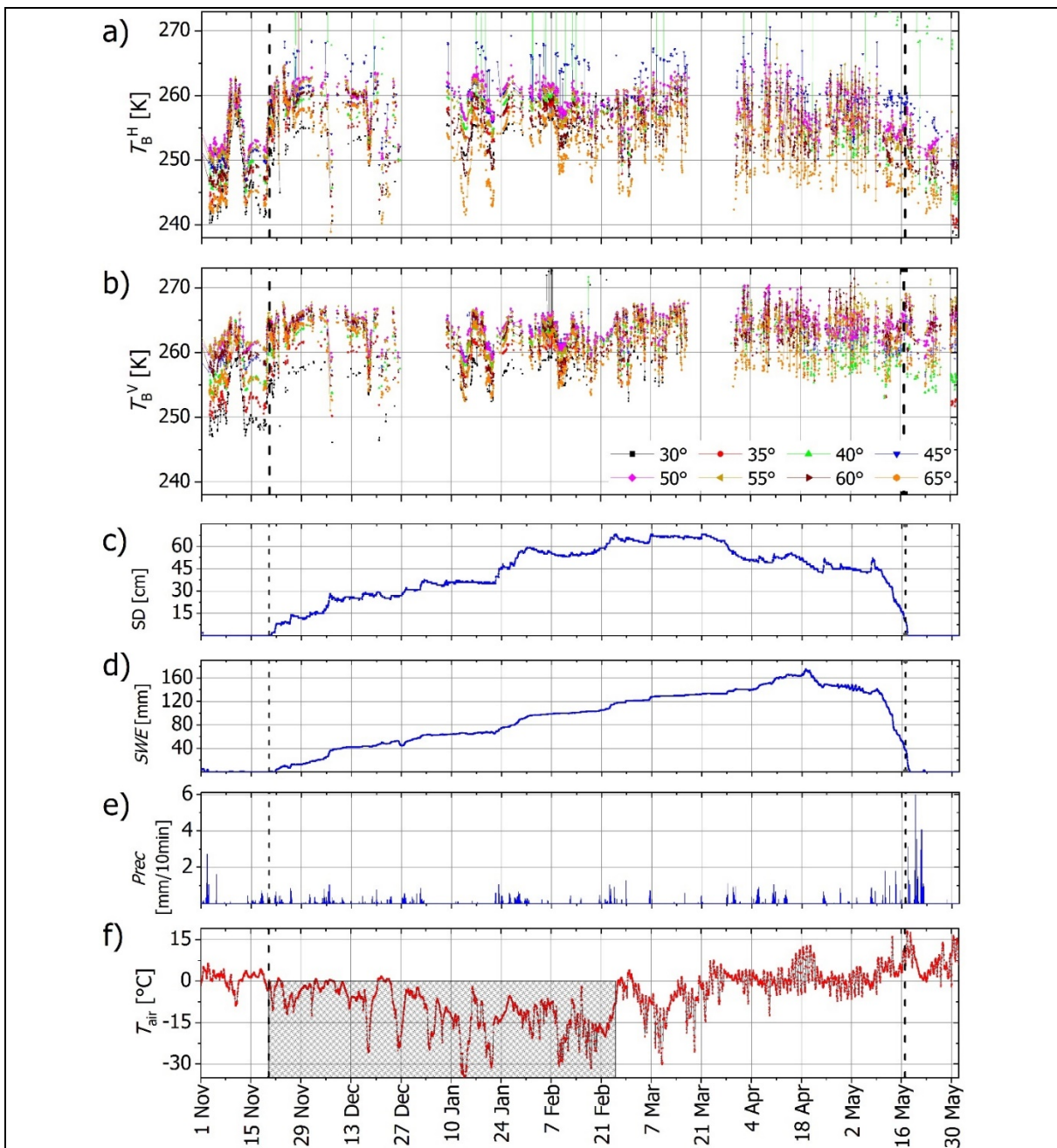


**Figure 2:** Time series of: a), b) L-band brightness temperatures  $T_B^{p,\theta}$ , c) snow depth  $SD$ , d)  $SWE$ , e) precipitation intensity  $Prec.$ , and f) air temperature  $T_{air}$  measured during the winter campaign 2020/2021 at FMI-ARC in Sodankylä (Finland).

The length of winter time with air temperatures below freezing is noticeably different between Sodankylä and Davos-Laret. As shown in **Figure 2 f)**, with a few exceptions  $T_{\text{air}}$  stays below  $0^{\circ}\text{C}$  for about four months between mid-November 2020 to late-March 2021. This indicates dry snow conditions for a much longer period than in Davos-Laret where it was typically a month of consistent  $T_{\text{air}} < 0^{\circ}\text{C}$  and dry snow conditions [8].

In **Figure 2** the onset of snow cover on 20 November 2020 and its complete melt on 17 May 2021 are marked with vertical dashed lines in all panels. It is evident in **Figure 2 a)** that the onset of snow cover has a distinct increasing effect on the  $T_{\text{B}}^{\text{H},\theta}$  which itself is dependent on the observation nadir angle  $\theta$ . Similarly, the complete melt of snow cover has an effect on  $T_{\text{B}}^{\text{H},\theta}$  such that  $T_{\text{B}}^{\text{H},\theta}$  falls by as much as 10 K as a response to the absence of snow. The L-band brightness temperature  $T_{\text{B}}^{\text{V},\theta}$  at vertical polarization  $p = \text{V}$  (**Figure 2 b)**) also responds to the snow cover changes but less distinctly compared to  $T_{\text{B}}^{\text{H},\theta}$ . The closer the observation nadir angle  $\theta$  to the Brewster angle, the less distinct the response of  $T_{\text{B}}^{\text{V},\theta}$  to snow cover variations.

It should be noted that the observation nadir angle scanning mechanism of ELBARA implies observing physically different areas of the canopy at different  $\theta$ . Therefore, the effect of spatial heterogeneities on  $T_{\text{B}}^{\text{p},\theta}$  should not be ignored. Furthermore, because ELBARA does not use an azimuth scanning system, it does not have overlapping measurements with WBSCAT over the treeless ground area.

## 6. WIDE-BAND SCATTEROMETRY

**Figure 3 a,b)** shows the time series of co-polarized radar cross sections  $\sigma_{\text{VV,C}}(f)$  and  $\sigma_{\text{VV,G}}(f)$  measured approximately over the Canopy and treeless ground areas, respectively (see **Table 1** and **Figure 1 d)**). In **Figure 3 a,b)**  $\sigma_{\text{VV}}(f)$  is shown for the frequencies  $f = \{2,6,10,16,20,32\}$  GHz covering a wide range of wavelengths from  $\lambda \approx 15$  cm to  $\lambda \approx 1$  cm. It is noteworthy that the approach for the computation of normalized radar cross section  $\sigma_{\text{pp}}^0(f)$  ( $\equiv$  backscattering coefficients) from WBSCAT measurements, given in [6], assumes that the instrument is sufficiently far from the observed target area. This ensures that the distance from the antennas' phase center to the footprint point along the antenna boresight is nearly the same as the distance from the antennas' phase center to any other point within the 3 dB projected footprint area. This allows for the computation of the effective area by which the radar cross section  $\sigma_{\text{pp}}(f)$  is divided to achieve  $\sigma_{\text{pp}}^0(f)$ . This assumption is true for example for airborne and satellite measurements. However, WBSCAT was installed at 19-m height above ground and looked into the canopy whose height is as much as 16 m. As a result, the conventional method for the computation of  $\sigma_{\text{pp}}^0(f)$  is not applicable. Therefore, in this report we demonstrate  $\sigma_{\text{VV}}(f)$  in dBsm (dB square meters). Nevertheless, it is possible to extract qualitative information by inspecting the temporal evolution of  $\sigma_{\text{VV}}(f)$  in response to ground and snow conditions and by comparing  $\sigma_{\text{VV,C}}(f)$  and  $\sigma_{\text{VV,G}}(f)$  to infer the differences between scattering from bare ground

and the ground underneath canopy. The former could be the case for the vast Tundra regions in high northern latitudes and the latter is representative of the ever-green northern forests.

Because the employed Quad-Ridged horn antennas [9] are electrically small, the polarization mixing effect cannot be ignored. Nevertheless, the data set includes radar cross sections for all available polarization combinations  $\sigma_{VV}(f)$ ,  $\sigma_{HH}(f)$ , and  $\sigma_{VH}(f)$ .

**Figure 3 c) - e)** show the time series of snow depth, precipitation intensity, and air temperature, respectively. This data is identical to the set shown in **Figure 2**, only repeated here for better readability next to the time series of  $\sigma_{VV,C}(f)$  and  $\sigma_{VV,G}(f)$ . Two vertical dashed lines are included in each panel in **Figure 3** to indicate the onset and melt of the snowpack.

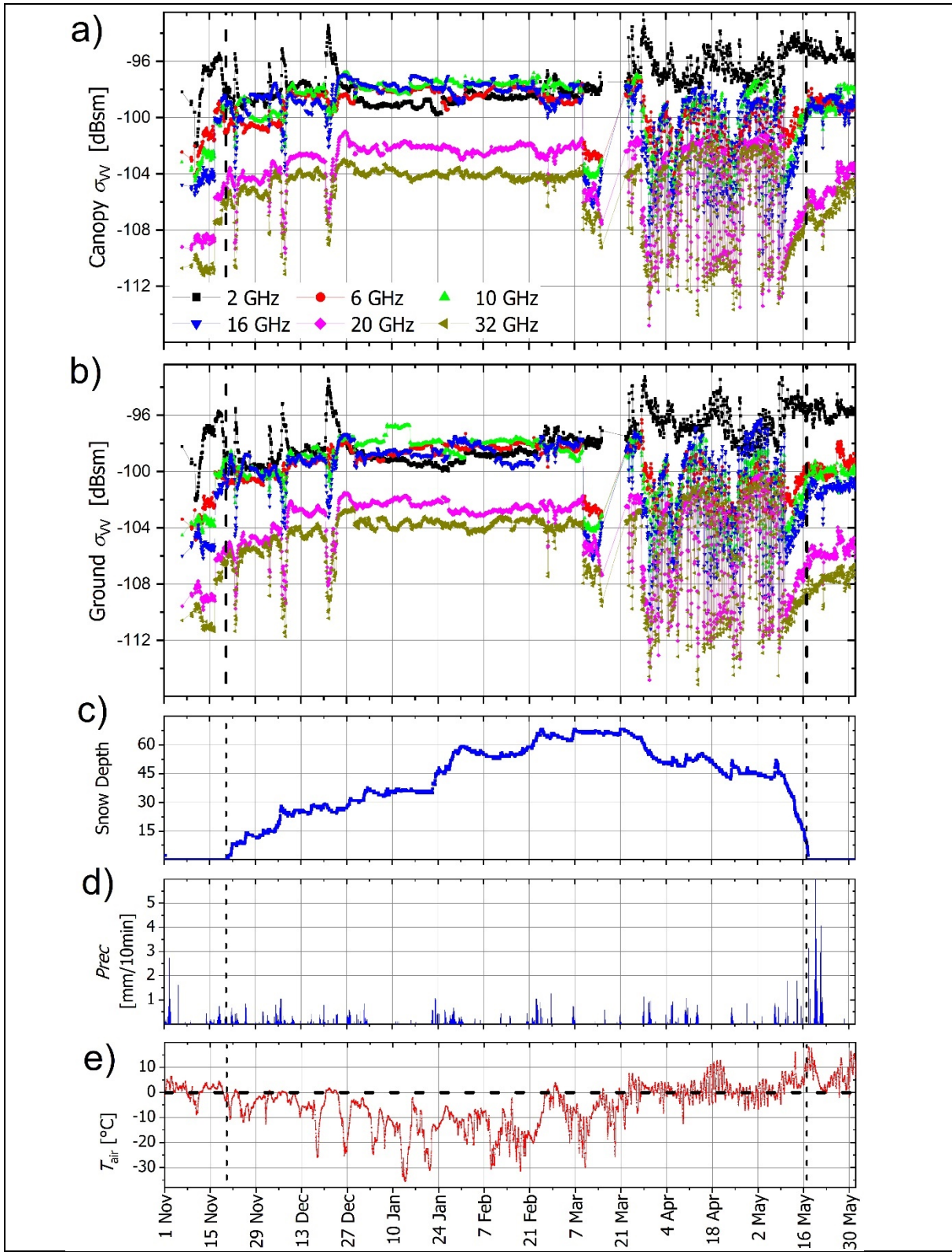


**Figure 3:** a, b) time series of co-polarized radar cross sections  $\sigma_{VV,C}(f)$  and  $\sigma_{VV,G}(f)$  measured over the Canopy and treeless Ground areas, respectively (see Table 1 and Figure 1 d)). Time series of: c) snow depth, d) precipitation intensity, and e) air temperature.

The response of  $\sigma_{VV,C}(f)$  and  $\sigma_{VV,G}(f)$ , especially at  $f > 2$  GHz, to the onset of snow cover is evident in **Figure 3 a,b**).  $\sigma_{VV}(f)$  increases by as much as 4 dB as a result of snow depth increasing from 0 cm to 15 cm.

Between 27 December 2020 and 7 March 2021,  $\sigma_{VV,C}(f)$  and  $\sigma_{VV,G}(f)$  seem to be stable which itself is a sign of dry snow and cold winter conditions. As shown in [6], during cold winter period, backscattering still responds to precipitation, changes in the underlying ground and even SWE. However, such in depth analysis is outside the scope of this report.

Between 27 March 2021 and 9 May 2021,  $\sigma_{VV,C}(f)$  and  $\sigma_{VV,G}(f)$  show daily fluctuations, which as shown in [6] is a sign of snow melt. As expected, the amplitude of these fluctuations depends on the frequency of observation. In simplified terms, the higher the frequency, the stronger the fluctuations in response to snow wetness variations during the melting period.

Other inspections reveal increasing differences between  $\sigma_{VV,C}(f)$  and  $\sigma_{VV,G}(f)$  at a given frequency growing from snow cover times to snow-free times after winter. This is possibly a hint to the increased scattering effect and contribution of the canopy when it is unfrozen. Furthermore, this difference between frozen and unfrozen canopy conditions is generally larger at higher frequencies. This is because at longer wavelengths, propagation losses are smaller, and the scattering elements are simply fewer and contributing less. At higher frequencies, small branches and even needle leaves contribute to backscattering. Therefore, during unfrozen times when the canopy becomes an effective part of total backscattering, these elements add to the total backscatter from the canopy.

There exists only one major gap in  $\sigma_{VV}(f)$  time series between 15 March 2021 and 22 March 2021. This gap was due a temporary internal software problem.

## 7. LESSONS LEARNED

Lessons learned during the Sodankylä campaign that are considered as useful for the design and conduction of future campaigns using WBSCAT are listed with the following bullet-points:

- Installation height of WBSCAT should be significantly higher than the expected snow-height. This is important to ensure consistency with certain assumptions in data processing.
- Remote access to the entire system is important because: 1) for regularly checks of data sanity, and 2) to allow to intervene in the event of technical problems or at least to be able to narrow down the cause of the problem.
- Quasi-simultaneous observations of at least two different target areas (in our case forested and non-forested areas). This allows reliable relative statements about changes in backscatter over time, independent of existing deficiencies in the WBSCAT data processing.

## 8. MANUAL IN-SITU SNOW CHARACTERIZATION

During the Winter 2020/2021 campaign, a total of 21 manual snow characterization measurements were performed at the ICOS tower to accurately monitor the following snow parameters: Snow temperature, SWE, snow depth, snow density using a standard 5-cm thick density cutter, and snow grain size.

## 9. APPENDIX: DATA FORMATS

The data package corresponding to D8 and D8a comes in eight categories whose content and format are explained in the following.

### 01\_LBand\_TB

It contains two main folders with “elbara-2” and “elbara-3” measurements. In each of these folders, there are subfolders whose name corresponds to the date of the measurements. Inside each subfolder, calibrated L-band brightness temperature for each hourly scan is given.

Data Directory

For ELBARA-II measurements:

01\_LBand\_TB\elbara-2\YYYYmmDD\YYYYmmDDHHMMSS\_TB.txt

For ELBARA-III measurements

01\_LBand\_TB\elbara-3\YYYYmmDD\YYYYmmDDHHMMSS\_TB.txt

Inside the text files, the following information are provided:

- Temperature-dependent ACL noise temperature for each single measurement reported in the text file.
- Date and Time in 6 numeric columns: YYYY mm DD HH MM SS
- T\_rec: Temperature of the receiver (= radio frequency assembly)
- elev: observation elevation angle for a given measurement. This is in the range of 30° to 180°
- TBH\_ch1: Calculated  $T_B^{H,1}$  at horizontal polarization and frequency channel 1
- TBH\_ch2: Calculated  $T_B^{H,2}$  at horizontal polarization and frequency channel 2
- TBV\_ch1: Calculated  $T_B^{V,1}$  at vertical polarization and frequency channel 1
- TBV\_ch2: Calculated  $T_B^{V,2}$  at vertical polarization and frequency channel 2
- TBH\_mean: Average value of brightness temperatures at two channels  $T_B^{H,1}$  and  $T_B^{H,2}$
- TBV\_mean: Average value of brightness temperatures at two channels  $T_B^{V,1}$  and  $T_B^{V,2}$
- (TBH+TBV)/2
- T\_ext: air temperature measured by ELBARA’s external PT-100 sensor

### 02\_RCS

This folder contains two sets of 12 files which include the same data in “.csv” and “.mat” formats. For each of the six frequency bands, raw internally calibrated WBSCAT two-dimensional scan data are processed to compute the radar cross section  $\sigma_{pp}$  for  $pp = \{HH, VV, VH\}$ . The average  $\sigma_{pp,G}$  and  $\sigma_{pp,C}$  for treeless ground patch and canopy areas, respectively, are calculated using the azimuth ranges given in **Table 1**. The  $\sigma_{pp}$  is given in dBsm or in other words dB square meters.

**03\_ManualSnowPit**

It contains the EXCEL file “Snowpit\_2021\_ICOS.xlsx” with all the *in-situ* snow measurements performed at the ICOS tower during the 2020/2021 campaign.

**04\_RadiationData**

An EXCEL file containing the measured long and short wave radiation at the FMI-ARC. This data set begins on 1 August 2020 and ends on 1 January 2022.

**05\_MeteoData**

Measurements recorded by the AWS at the ICOS tower are given in a text file “MeteoData.txt” which contains a time series starting on 1 August 2020 and ends on 31 December 2021. The following parameters are saved in comma-separated format:

- 1) T Air temperature 2m
- 2) TD Dew point temperature
- 3) RH Air relative humidity
- 4) TG Ground temperature
- 5) P\_SEA Air pressure at sea level
- 6) P\_ST Air pressure at station level
- 7) SD Snow depth
- 8) VIS Visibility
- 9) RI\_OPT Precipitation intensity 10min average from optical sensor
- 10) RI Precipitation intensity 10min average
- 11) PW Present weather WMO code 4680
- 12) WS Wind speed 10min average 22m
- 13) WD Wind direction 10min average 22m
- 14) WG Wind gust 10min maximum 22m
- 15) CH1 Height of the lowest cloud base or vertical visibility
- 16) CH2 Height of the 2nd lowest cloud base
- 17) CH3 Height of the 3rd lowest cloud base
- 18) CH4 Height of the 4th lowest cloud base
- 19) N Total cloudiness 1/8 (N, value 9 = can't be defined)

## 10. REFERENCES

- [1] M. Schwank *et al.*, "ELBARA II, An L-Band Radiometer System for Soil Moisture Research," *Sensors MDPI*, vol. 10, pp. 584-612, 2010.
- [2] J. Jorge Ruiz *et al.*, "Sodsar: A tower-based 1–10 ghz sar system for snow, soil and vegetation studies," *Sensors*, vol. 20, no. 22, p. 6702, 2020.
- [3] C. L. Werner *et al.*, "Processing and Calibration of Continuous Snowpack Measurements using the WBSCAT Polarimetric Microwave Scatterometer During Winter 2018-2019 at Davos Switzerland," in *AGU Fall Meeting Abstracts*, 2019, vol. 2019, pp. C33E-1639.
- [4] C. Werner, M. Suess, U. Wegmüller, O. Frey, and A. Wiesmann, "The ESA wideband microwave scatterometer (WBSCAT): Design and implementation," in *IGARSS 2019-2019 IEEE International Geoscience and Remote Sensing Symposium*, 2019, pp. 8339-8342: IEEE.
- [5] C. L. Werner, O. Frey, U. Wegmüller, A. Wiesmann, and M. Suess, "The WBSCAT polarimetric synthetic aperture scatterometer for retrieval of in-situ time-series of snow structure," in *AGU Fall Meeting Abstracts*, 2018, vol. 2018, pp. C13D-1172.
- [6] R. Naderpour, M. Schwank, D. Houtz, C. Werner, and C. Mätzler, "Wideband Backscattering From Alpine Snow Cover: A Full-Season Study," *IEEE Transactions on Geoscience and Remote Sensing*, pp. 1-15, 2021.
- [7] R. Naderpour, M. Schwank, and C. Mätzler, "Davos-Laret Remote Sensing Field Laboratory: 2016/2017 Winter Season L-Band Measurements Data-Processing and Analysis," *Remote Sensing*, vol. 9, no. 11, p. 1185, 2017.
- [8] R. Naderpour, M. Schwank, D. Houtz, and C. Mätzler, "L-Band Radiometry of Alpine Seasonal Snow Cover: 4 Years at the Davos-Laret Remote Sensing Field Laboratory," *Journal of Selected Topics in Applied Earth Observations and Remote Sensing (JSTARS)*, submitted in February 2022.
- [9] R. Dehdasht-Heydari, H. R. Hassani, and A. R. R. Mallahzadeh, "Quad ridged horn antenna for UWB applications," *Progress In Electromagnetics Research*, vol. 79, pp. 23-38, 2008.